Fault Diagnosis and Prediction in Reciprocating Air Compressors by Quantifying Operating Parameters

by

Ming-Fa Feng

Dissertation submitted to the Faculty of the

Virginia Polytechnic Institute and State University

in partial fulfillment of the requirements for the degree of

Doctor of Philosophy

in

Mechanical Engineering

APPROVED:

Reginald G. Mitchiner, Chairman

Charles E. Knight

Robert G. Leonard

Mahendra P. Singh

Alfred L. Wicks

March 5, 1992

Blacksburg, Virginia

Fault Diagnosis and Prediction in Reciprocating Air Compressors by Quantifying Operating Parameters

by

Ming-Fa Feng

Reginald G. Mitchiner, Chairman

Mechanical Engineering

(ABSTRACT)

This research introduces a new method of diagnosing the internal condition of a reciprocating air compressor. Using only measured load torques and shaft dynamics, pressures, temperatures, flow rates, leakages, and heat transfer conditions are quantified to within 5 %.

The load torque acting on the rotor of the machine is shown to be a function of the dynamics (instantaneous position, velocity, and acceleration) of the driving shaft, the kinematic construction, and the internal condition of the machine. If the load torque, the kinematic construction of the machine, and the dynamics of the rotor are known, then the condition of the machine can be assessed.

A theoretical model is developed to describe the physical behavior of the slider-crank mechanism and the shaft system. Solution techniques, which are based on the machine construction, crankshaft dynamics, and load torque measurements, are presented to determine the machine parameters. A personal computer based system used to measure the quantities necessary to solve for the machine parameters and the quantities used to compare with calculations is also documented.

The solution algorithm for multi-stage compressors is verified by decoupling the load torque contributed by each cylinder. Pressure data for a four-stage two-cylinder high pressure air compressor (HPAC) is used. Also, the mathematical model is proven feasible by using measured angular velocity of the crankshaft and direct measurements of the load torque of a single stage, single cylinder air compressor to solve for the machine parameters.

With this unintrusive and nondestructive method of quantifying the operating parameters, the cylinder pressures, operating temperatures, heat transfer conditions, leakage, and power consumption of a reciprocating air compressor can be evaluated.

Acknowledgements

First of all I would like to express my sincere gratitude to Dr. R.G. Mitchiner, my major professor, for his patience, guidance, and encouragement during the development and completion of this research. Also, I would like to take this opportunity to thank Dr. A.L. Wicks, Dr. R.G. Leonard, Dr. M.P. Singh, and Dr. C.E. Knight for serving as the committee members in this work. Their guidance and support have been invaluable. Special thanks go to Dr. Frederick Brockhurst, Professor of Electrical Engineering Rose-Hulman Polytechnic Institute, Indiana, for his advice on this research.

My thanks also go to the instrument shop personnel and machinists in the mechanical engineering department of VPI&SU. Without the professional help of Mr. Frank Caldwell, Mr. Billy Shepherd, and Mr. Ben Poe, this work could not have been completed.

Finally, I am indebted to my mother, brothers and sisters for their unfailing love and support. I value their faith in my ability to achieve anything I can imagine.

Table of Contents

List of Illustrations

List of Tables

1.0 Introduction

Machinery operation experiences have shown that failures are preceded by certain signs, conditions, indications, or processes that portions of the machine are degrading. Most research in this area has attempted to diagnose machine faults by the monitoring of vibration levels of the machine. Certain machine failures, such as the impending spalling of a ball bearing, are characterized by an increase in the vibration amplitude at certain frequencies. By monitoring the frequency content of a displacement vibration signature over time, impending catastrophic failure of various machine components may be foreseen.

In this study, another method of diagnosing the internal condition of a reciprocating compressor will be introduced. The load torque acting on the rotor of the machine is a function of the dynamics (instantaneous position, velocity, and acceleration) of the driving shaft, the kinematic construction, and the internal condition of the machine. If the load torque, the kinematic construction of the machine and the dynamics of the rotor are known, then the condition of the machine can be assessed.

The purpose of this research is the identification of the machine condition by quantifying the intake and discharge pressure levels and fluctuations, expansion constants, friction force between the piston ring and the cylinder wall, and other operating parameters. This is accomplished by measurement, in real-time, of the dynamics of the rotor and measurement of the power, voltages, and currents input to the driving motor. Then, with full knowledge of the motor's influence on the rotor dynamics, the set of compressor parameters necessary to give the measured velocities and accelerations can be determined. These compressor parameters are solved for, using the dynamics and kinematics equations for the compressor as presented herein.

Figure 1-1 shows the rotor of the driving motor (three phase induction motor) rigidly coupled to the shaft of the compressor and the energy diagrams for the motor, coupling, and compressor. According to conservation of energy principle, for the motor system:

$$P_{mo}(t) = P_{mi}(t) - P_{lm}(t) \qquad (1-1)$$

where

P_{mo} Power output from the motor, the same with the power input to the coupling system.

P_{mi} Electric power input to the motor, can be calculated by using measurements of the instantaneous currents, I, and voltages, V, of the three phase electric supply to the motor.

P_{lm} Power losses of the motor.

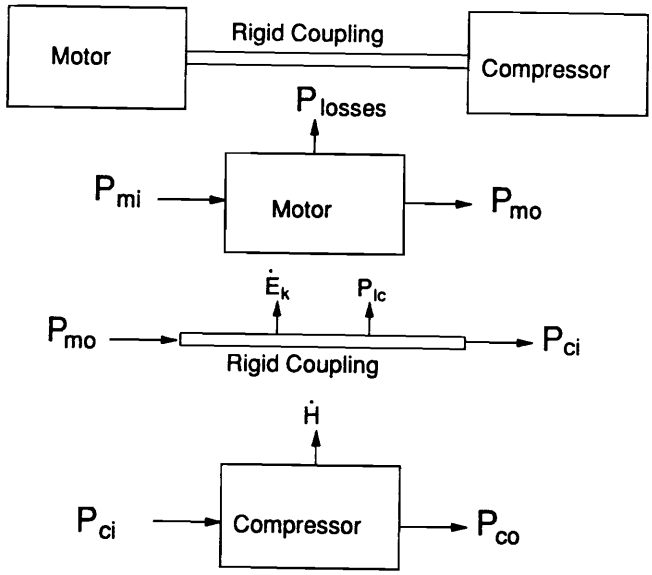

Figure 1-1. Motor-Coupling-Compressor System

For the coupling system, the energy equation can be expressed as:

$$P_{mo}(t) = P_{ci}(t) + \dot{E}_k(t) + P_{lc}(t) \qquad (1-2)$$

where

P_{ci} Power input to the compressor, the same with the power output from the coupling system.

$\dot{E}_k$ Kinetic energy change rate of the coupled shaft system.

P_{lc} Power losses of the coupling system.

The power input to the compressor, P_{ci}, can be expressed as:

$$P_{ci}(t) = T_L(t)\dot{\theta}(t) \qquad (1-3)$$

where

T_L Load torque needed to drive the compressor.

$\dot{\theta}$ Angular velocity of the shaft.

The rate of change of kinetic energy, $\dot{E}_k$, can be expressed as:

$$\dot{E}_k(t) = J_S\ddot{\theta}(t)\dot{\theta}(t) \qquad (1-4)$$

where

J_S Mass moment of inertia of the shaft system.

$\ddot{\theta}$ Angular acceleration of the shaft, can be evaluated by differentiating the velocity with respect to time.

The viscous power loss of the coupling system, P_{lc}, can be expressed as:

$$P_{lc}(t) = C_S\dot{\theta}(t)\dot{\theta}(t) \qquad (1-5)$$

where

C_S Damping coefficient of the shaft system, assumed constant.

Then, equation 1-2 can be rearranged as:

$$T_L = \frac{\sum_{i=1}^{3}(I_i(t)V_i(t) - P_{lmi}(t))}{\dot{\theta}(t)} - J_S\ddot{\theta}(t) - C_S\dot{\theta}(t) \qquad (1-6)$$

Further, T_L can be analytically expressed as a function of the kinematic construction of the compressor, the position, velocity, and acceleration of the shaft, and the compressor parameters. Then, by solving Equation 1-6, the equation set, the compressor parameters can be assessed.

For the compressor system in Figure 1-1, the energy equation is:

$$P_{ci}(t) = \dot{H}(t) + P_{co}(t) \qquad (1-7)$$

where

$\dot{H}$ Heat transferred from the compressor.

P_{co} Power output from the compressor, as form of pressure work and internal energy increase of air.

After the compressor parameters are solved, the power input to the compressor, P_{ci}, can be evaluated and the power output from the compressor, P_{co}, can be evaluated by calculating the energy change between the intake and exhaust air of the compressor. Then, by solving Equation 1-7, the heat transfer condition can be identified.

In the first phase of this research, a mathematical model was developed to express the load torque, in terms of the kinematic construction of the machine and the machine condition indicators, the intake and discharge pressure levels and fluctuations, expansion and compression constants, and internal friction. This set of analytical expressions, in terms of the machine condition indicators and the dynamics of the rotor, can be equated to the right-hand side of Equation 1-6, which is based on constants, dynamics observations, and current and voltage measurements of the electric supply. The resulting mathematical model is an equation set. By solving this equation set, the machine condition indicators can be assessed. In this phase of the investigation, the experimental data of a Worthington 50 Hp high pressure four-stage air compressor from DTRC (David Taylor Research Center) is used to verify the solution techniques.

In the second phase of the research, an experiment was devised. The acquisition of θ, $\dot{\theta}$, and $\ddot{\theta}$ is accomplished from a purpose built research machine using methods outlined by Kanth [1987], and Williams [1989]. First, the load torque was measured mechanically by a load cell. Using the solution techniques developed in the first phase, the machine condition indicators are to be assessed. After the mathematical model used to describe the physical behavior of the compressor was proven accurate, the output torque of the motor was calculated by using the measurements of the motor phase currents and voltages to verify the feasibility of Equation (1-6). The compressor used in this phase is a single cylinder, single stage reciprocating air compressor.

1.1 References

1. Kanth, R.M., 1987, *A Personal Computer Based Instrumentation System for Determining Real-Time Dynamic Torque in Rotating Machinery* Masters Thesis, Virginia Polytechnic Institute and State University, Blacksburg, VA.

2. Williams, J, 1989, *Parameter Identification in a Slider-Crank Mechanism Through Direct Measurement of Shaft Velocity* Masters Thesis, Virginia Polytechnic Institute and State University, Blacksburg, VA.

2.0 Literature Review

2.1 Machinery Diagnosis

The major thrust in the diagnosis of machinery conditions recently could be observed in measurement, feedforward and feedback control, alarm monitoring and protection, documentation, manual operation, and optimization. Progress has been made in the development of equipment for measurement and control. The improvements in process control are, on one hand, based on the development of components for sensors, transducers, control systems, and actuators, and on the other hand, on the understanding and modeling of process dynamics and on applied control theory. Furthermore, the components for process supervision, including alarm monitoring and protection, were developed. However, the implemented methods are still simple and exist mostly in the limit value checking of some easily available single signals. In contrast to the field of control, methods based on modern dynamic system theory are hardly applied.

The goal of machinery supervision is the detection of process changes and faults during normal operation and the taking of action to avoid damage to the process or other accident. For this task, a supervision loop is often implemented which contains the tasks:

1. Fault detection and diagnosis.

2. Fault evaluation.

3. Decision on operating state (stop or change parts).

4. Fault elimination.

2.1.1 Mathematical Model for Process Fault Diagnosis

Isermann, R.[1] proposed a mathematical model to represent a process influenced by a fault, schematically shown as Figure 2-1.

$$Y = f(U, N, \mathrm{X}, \Theta) \qquad (2-1)$$

where:

U(t),Y(t)	measurable input and output variables.
Θ	constant or slow time varying process parameters, unmeasurable.
X(t)	process state variables, unmeasurable.

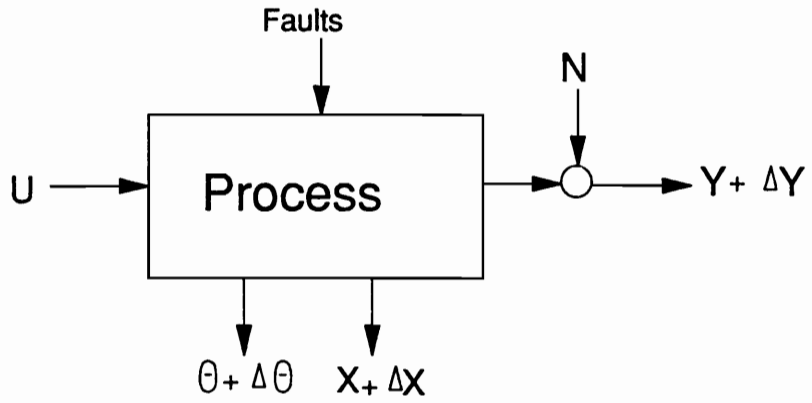

U,Y : measurable input and output variables

Θ : process parameters

X : process state varibles

N : disturbance variable (noise)

Figure 2-1. A Process Influenced by a Fault[1]

N(t) disturbance variables (noise).

If a process model is known, one is able to estimate the unmeasurable process variables, $X(t)$, or unmeasurable process parameters, $\Theta(t)$, based on the measurable inputs, U(t), and outputs, Y(t), by using state variable or process parameters estimation methods and to detect changes $\Delta X(t)$ or $\Delta\Theta(t)$.

2.1.2 Fault Diagnosis Based on Process Parameters

A schematic flow-chart from Isermann for technical fault diagnosis based on process parameters is shown in Figure 2-2. Three phases can be distinguished, namely:

1. Data processing

   The measured signal are processed by methods of filtering and estimation such that reduced information results which is suitable for fault detection and diagnosis. The reduced information, for example, exists in filtered signal components, correlation functions, or in parameter or state variable estimates, if process models are applied.

2. Fault detection

   Based on the reduced process information, features are extracted which allow the detection of faults in the process. Then, changes of these features are determined with reference to the normal process. These changes are then used to recognize the

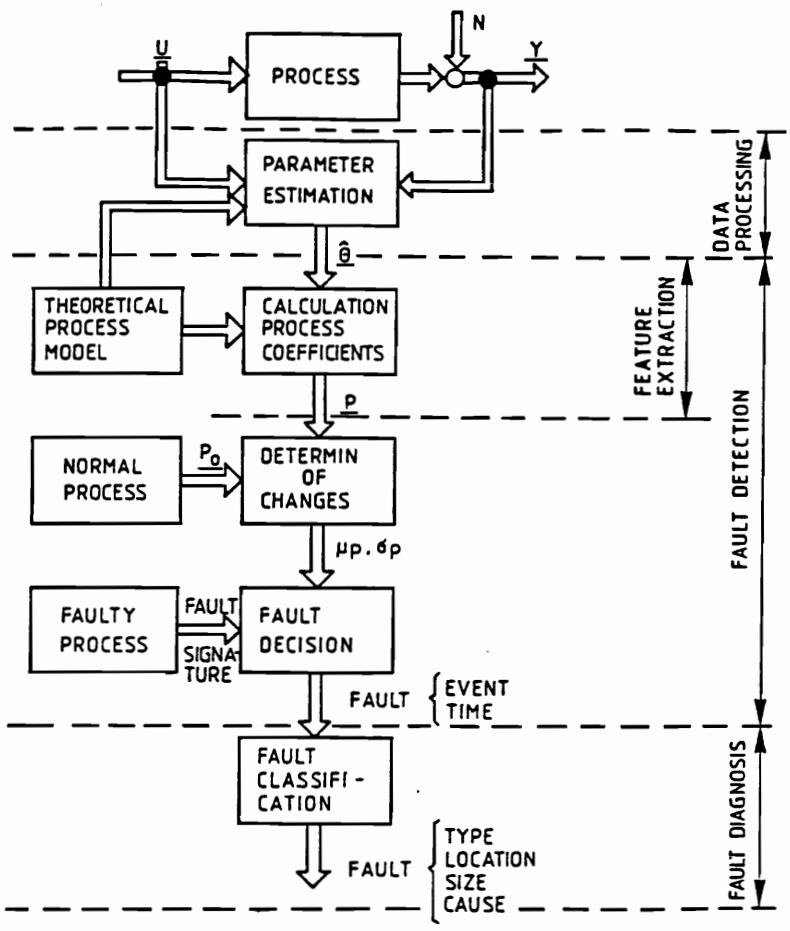

Figure 2-2. Fault Diagnosis Based on Process Parameters[1]

occurrence of a fault and the time of its event. For this task, statistical decision methods may be used.

3. Fault diagnosis

   After a fault event has been detected, the features and their changes are submitted to a classification procedure with the goal of determining the fault type, fault location, fault size, and the cause of the fault.

2.1.3 Examples of Fault Diagnosis Based on Parameter Estimation

Most contemporary research in machinery fault diagnosis has attempted to identify machine faults by checking some easily available signals instead of quantifying the process parameters. However, in 1987, D. T. Dalle Molle and D. M. Himmelblau[2] attempted to detect faults in an evaporator system by identifying the heat transfer coefficient and the composition of feedwater. In their research, the following procedures were implemented:

1. A state observer was combined with a least squares procedure in the time domain.

2. An extended Kalman filter was applied to the model when faults were introduced.

3. Noise was added to the model inputs and outputs to represent what might occur in the actual operation of equipment.

The Dalle Molle results demonstrated that the least squares estimation scheme is valid even when two faults occur simultaneously. However, for abrupt changes of the parameters, the estimate responds slowly and takes a long time to converge to new values.

In 1989, R.G. Mitchiner and J. William[3] demonstrated the procedures to identify parameters of a slider-crank mechanism by directly measuring the shaft velocity. In this research, a slider-crank mechanism attached with a spring and a damper, and coupled with a three phase induction a.c. motor was devised. In the parameter solving algorithm, two assumptions were made:

1. The machine is running in steady state, i.e. difference from revolution to revolution of the shaft is negligible.

2. In the Williams study, the attempt to mechanically measure the load torque were unsuccessful and the ac components of the output torque from the motor is proven insignificant in comparison with the ac components of the load torque. Therefore, the motor torque is assumed to be constant.

By curve-fitting in frequency domain, the reciprocating mass, spring rate and preload of the spring, and the damping coefficient of the damper were to be quantified. The results show that the calculated reciprocating mass and spring rate and preload of the spring are in good comparison with known value. However, the attempt to evaluate the damping failed.

2.2 *Reciprocating Air Compressors*

Reciprocating compressors compress gas by reducing a volume of gas that has been isolated in a cylinder (Figure 2-3.a). The theoretical evolution of a gas in the cylinder of a single-acting reciprocating compressor is as following:

1. Compression during the forward motion of the piston and discharge of the gas.

2. Expansion and suction during the return motion of the piston.

In an ideal cycle (Figure 2-3.b), the pressure-volume relationships for the compression and expansion are assumed to be polytropic.

$$PV^{\kappa} = constant \qquad (2-2)$$

where κ is the expansion constant and the pressure levels of discharge and suction are assumed to be constant.

As discussed by Pichot[4], there are pressure losses due to leakage around the discharge and suction valves, as well as losses due to valve pressure drops, gas heating, and internal leakage past the piston rings, so that the actual compression diagram has a modified shape, as shown in Figure 2-3.c.

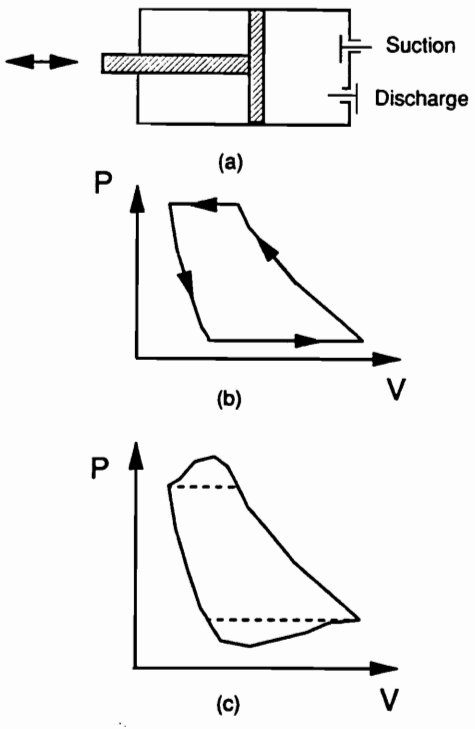

Figure 2-3. Operation Principle of Reciprocating Compressors

2.2.1 Expansion Constant

As shown in Figure 2-4, the ideal gas in the cylinder is to be compressed from pressure P_1 to P_2. In this polytropic process, the expansion constant, κ, depends only on the heat and work quantities during the process. According to the first law of thermodynamics for a closed system,

$$mC_V T_1 + W_{in} = Q_{out} + mC_V T_2 \qquad (2-3)$$

where:

C_V	Specific heat at constant volume of the gas
T_1, T_2	Temperature of the gas at states 1 and 2
m	Mass of the gas
W_{in}	Work done to the system
Q_{out}	Heat transfer from the system

For this closed system, the work done to the system can be evaluated by:

$$\begin{aligned} W_{in} &= -\int_{V_1}^{V_2} P dV \\ &= \frac{P_2 V_2 - P_1 V_1}{\kappa - 1} \end{aligned} \qquad (2-4)$$

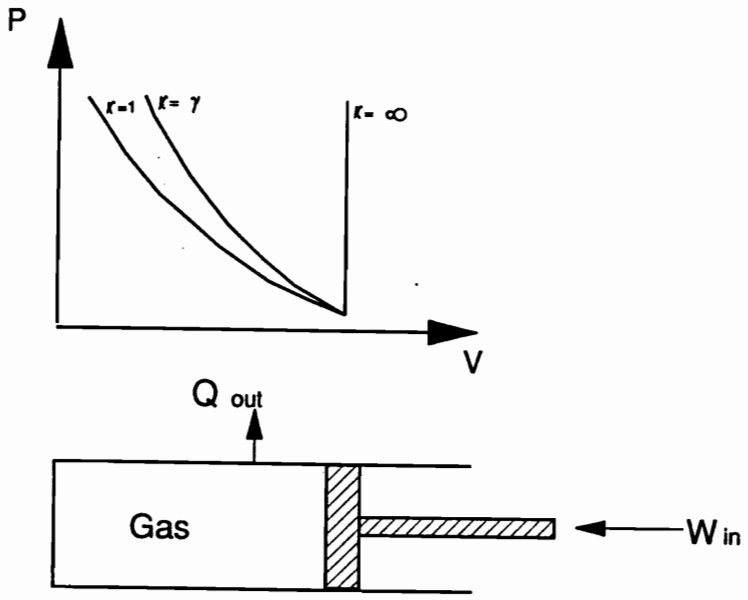

Figure 2-4. Polytropic Compression

Since the gas is assumed ideal, the temperature can be written as:

$$T = \frac{PV}{mR} \tag{2-5}$$

where R is the universal gas constant.

For ideal gases, the ratio of specific heats is defined as:

$$\begin{aligned} \gamma &= \frac{C_P}{C_V} \\ &= \frac{C_V + R}{C_V} \\ &= 1 + \frac{R}{C_V} \end{aligned} \tag{2-6}$$

In order to determine the sign of Q_{out}, the expansion constant κ can be rewritten as:

$$\kappa = 1 + \frac{\Delta}{C_V} \tag{2-7}$$

where, Δ is a parameter to determine the sign of Q_{out}.

Then, in equation 2-3, the heat transfer out of the system, Q_{out}, can be expressed as:

$$Q_{out} = (P_2V_2 - P_1V_1)\left(\frac{C_V}{\Delta} - \frac{C_V}{R}\right) \tag{2-8}$$

If during this compression process, the temperature rises, i.e. κ is larger than unity, then from the derivation above, the following can be concluded:

1. If $\Delta > R$, i.e. $\kappa > \gamma$, then $Q_{out} < 0$.

2. If $\Delta = R$, i.e. $\kappa = \gamma$, then $Q_{out} = 0$.

3. If $\Delta < R$, i.e. $\kappa < \gamma$, then $Q_{out} > 0$.

As discussed by Easttop and McConkey[5], in the thermodynamics of gas compression, there are some special processes:

1. When $\kappa = \infty$, $V = constant$, i.e. the process is a constant volume process.

2. When $\kappa = \gamma$, $Q_{out} = 0.$, i.e. the process is a reversible adiabatic, or thermally isolated process.

3. When $\kappa = 1.0$, $T = constant$, i.e. the process is isothermal.

Therefore, one may attribute a high expansion constant (greater than γ) to poor heat transfer conditions and heat gain caused by friction effects of the machine.

2.2.2 Leakage through piston ring pack

The purpose of the piston ring in a lubricated reciprocating compressors is two-fold. The ring prevents the leakage of the cylinder gas and prevents the ingress of excessive lubricating oil into the compression chamber. An ideal piston ring should be a perfect seal for the compressed gas and the ring itself should not allow any leakage past it. However, according to Nadeem[6], in practical applications, the cylinder gas may leak through the following three possible paths:

1. Through the ring edge.

2. Through the gap between the ring side face and the lower edge of groove.

3. Through the peripheral area between ring and cylinder bore.

Figure 2-5 shows these three possible leakage paths.

According to Ruddy, Dowson and Economou[7], if the piston ring is performing properly, the edge gap would be the primary leakage path. In practice, however, the axial movement of the ring in its groove can greatly increase the effective leakage area.

The ring edge gap increases progressively with wear of the ring surface. Figure 6 shows a worn ring inside a cylinder. The ring edge gap l_g is given as,

$$l_g = 2\pi\Delta_W \qquad (2-9)$$

where, Δ_W indicates the amount of wear. This increase in the gap results in the decrease of the piston ring friction force and the leakage of the cylinder gas. During the compression process, if the leakage is significant then the time to reach the output pressure level will be delayed, i.e. the expansion constant will diminish. That is, leakage could cause a low expansion constant during the compression process. However, during the expansion process, leakage accelerates the pressure drop from discharge to suction pressure level, i.e. a large expansion constant during the expansion process could be caused by leakage.

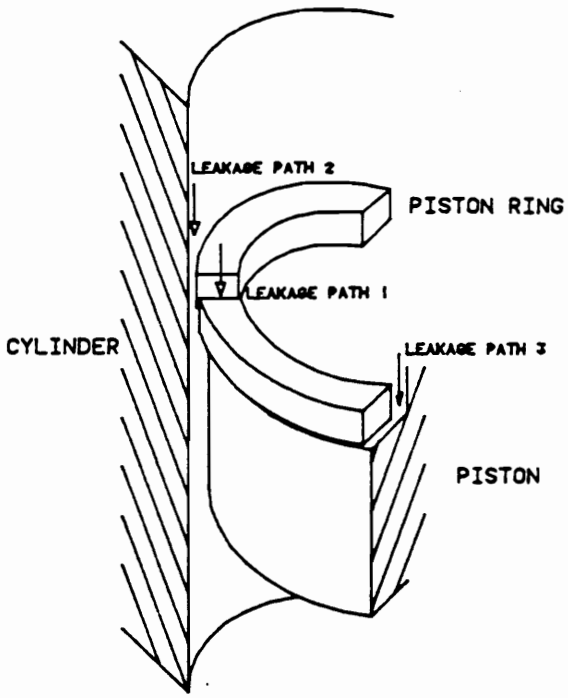

Figure 2-5. The Possible Leakage Paths Through the Piston Rings[6]

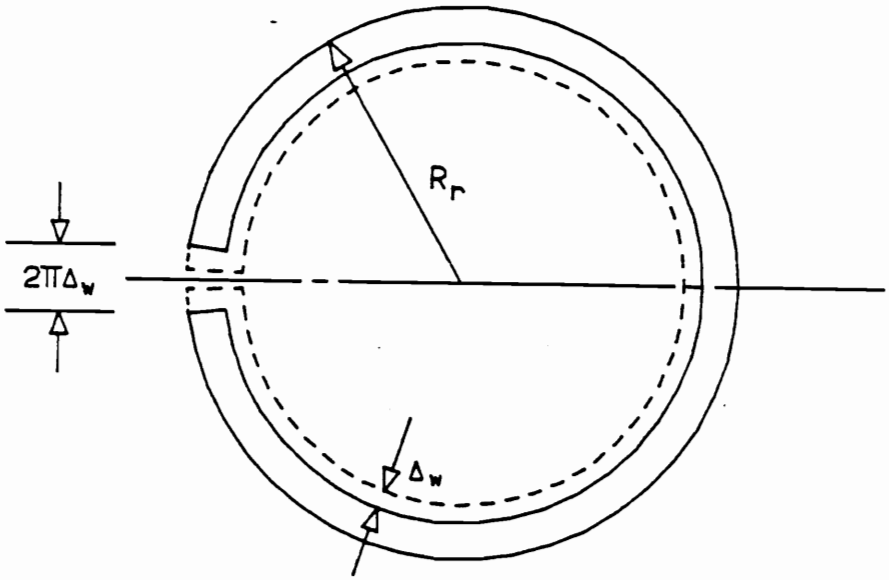

Figure 2-6. Change in Piston Ring Edge Gap After Wear[6]

2.2.3 Friction Force of Piston Rings Against Cylinder Wall

The research of S. Furuhama and M. Takiguchi[8] on the piston friction force in diesel engines concluded that

1. Friction forces of piston rings account for majority (more than 75%) of the total piston force.

2. The friction force of the piston rings against the cylinder wall without gas pressure is nearly the same to the friction force under firing operation.

3. The sliding surface temperature affects the oil viscosity and the friction force of the piston ring is then changed.

4. The friction force of the piston rings, F, is primarily determined by the ring force normal to the sliding surface, P_n.

$$F = fP_n \qquad (2-10)$$

where f is the friction coefficient which is independent to the back pressure of the piston.

In general application, the operating temperature is approximately within 100°F to 300°F. According to experimental data of S. Furuhama and M. Takiguchi[8], the friction coefficient between the piston rings and the cylinder wall can be treated as constant within this temperature range without significant error (less than 5%).

Since the friction is not conservative, in one complete compressor cycle, the work consumed by the friction force is evaluated as

$$W_F = \int F ds \qquad (2-11)$$

This work needed to overcome the friction force will be transferred into heat energy and raises the operating temperature.

2.2.4 Valves

In a reciprocating compressor, the inlet and outlet valves are used to to control the gas flow from the intake chamber to cylinder and that from the cylinder to the discharge chamber. The most commonly used valves for reciprocating compressor are finger type valve. As described by Spagnuolo[9], the operating principle is shown as Figure 2-7.

As shown in Figure 2-3, because of the inertia of the gas flow and the overpressure to open the valves, there exist pressure excursions during the intake and discharge processes on P-V diagram. The excursions depend on the pre-load of the valve and the inertia of the gas. Besides, the bounce of the valves will cause the pressure fluctuations during the intake and discharge. According to Soedel[10], theoretically, the valves can be modeled as a cantilever beam. As discussed by Spanuolo[9], the finger valve reed may be simplified as one-degree-of-freedom spring-mass-damper system.

$$M_{eq}\ddot{Y} + C_{eq}\dot{Y} + K_{eq}Y = F_V - PL \qquad (2-12)$$

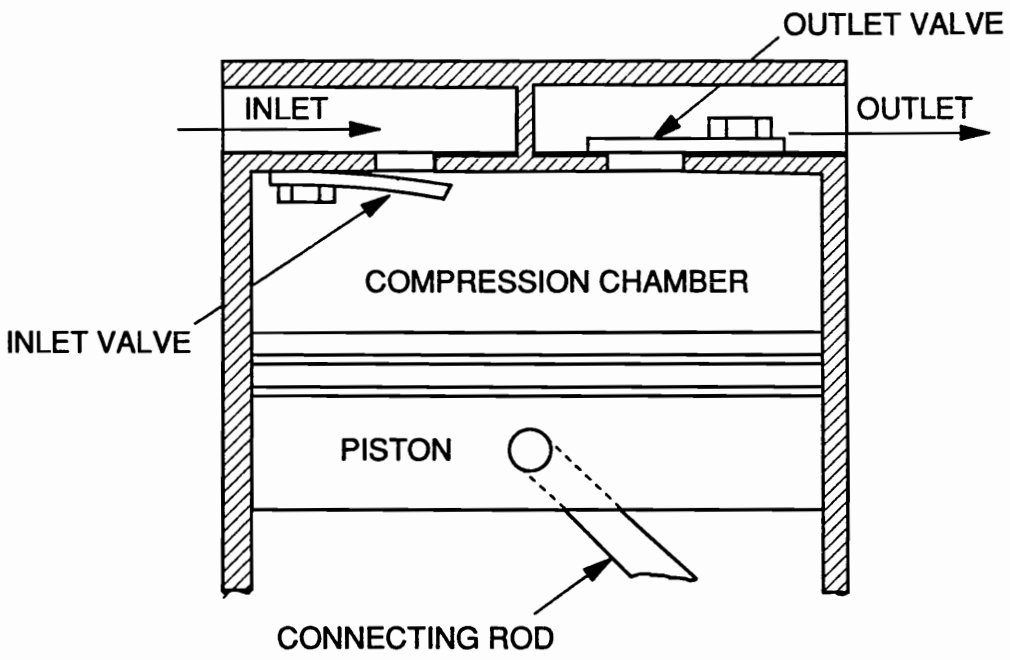

Figure 2-7. Operating Principle of Finger Type Valves

where PL is the preload on the valve and M_{eq} and K_{eq} are the equivalent mass and stiffness for the valve. For the first mode, Harris[11] gave the following expression for a cantilever beam with distributed mass,

$$M_{eq} = 0.234 M_V \tag{2-13}$$

$$K_{eq} = \frac{3 E_V I_V}{L_V^{\,3}} \tag{2-14}$$

where, M_V, E_V, I_V and, L_V indicate mass, modulus of elasticity, area moment of inertia, and length of the valve respectively. C_{eq} is the equivalent damping coefficient of the gas.

The force F_V acts on the face of the valve and it depends on the pressure difference across the valve ΔP and effective area of the valve, A_F.

$$F_V = A_F \Delta P \tag{2-15}$$

According to Equation 2-12, the fatigue of the valve will cause pre-load loss then, the valve's premature opening, i.e. the discharge pressure level diminishes and the intake level increases. High stiffness of the valve may cause the rebound, therefore high frequency fluctuations during intake and discharge may occur.

2.2.5 Energy Balance for a Multi-Stage Compressor With Intercooler

According to Easttop and McConkey[5], for a multi-stage reciprocating gas compressor, intercoolers are needed for:

1. Preventing the operating temperature of the machine from being too high.

2. Reducing the externally provided work needed by the machine, i.e., increasing the efficiency of the machine.

Figure 2-8.a shows an intercooler for a multi-stage compressor schematically, Figure 2-8.b indicates the ideal P-V diagram of this multi-stage compressor without intercooler and Figure 2-8.c indicates the ideal P-V diagram for the compressor and the saving in work obtained by intercooler by the shaded area.

By neglecting changes in kinetic energy, the general form of the first law of thermodynamics for steady flow can be expressed as:

$$\dot{m}h_1 + \dot{W}_{in} = \dot{m}h_2 + \dot{Q}_{out} \qquad (2-16)$$

where:

$\dot{m}$ mass flow of the steady system.

$\dot{W}_{in}$ power done on the system.

$\dot{Q}_{out}$ rate of heat transferred out from the system.

h_1, h_2 enthalpies per unit mass at input and output conditions, which can be can be expressed as:

$$h = C_P T \qquad (2-17)$$

where, C_P is the specific heat at constant pressure of the gas and T is the temperature.

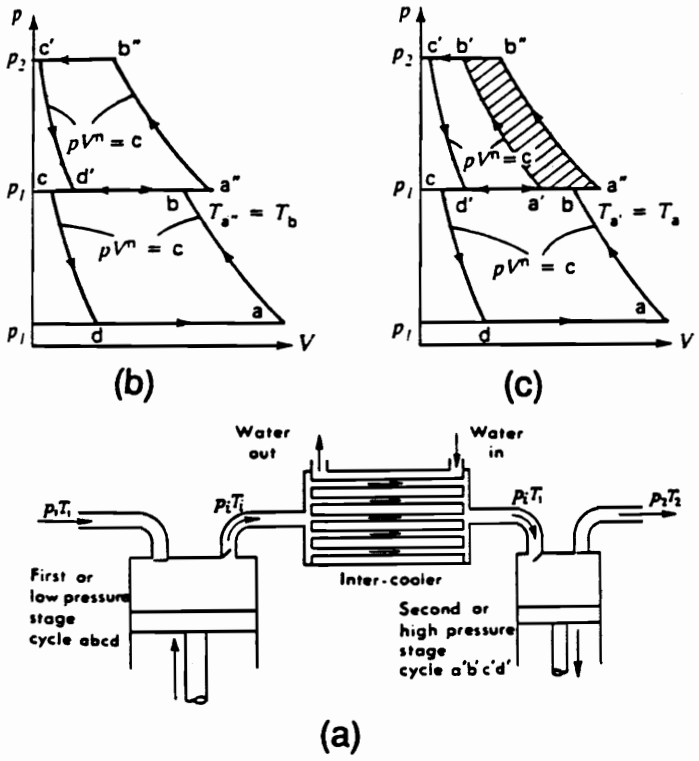

Figure 2-8. Operating Principle of an Intercooler

Referring to Figure 2-9, by applying the first law of thermodynamics for steady flow to the low-pressure stage, the intercooler, and the high-pressure stage in turn, the rates of heat transferred out from the low-pressure stage, the intercooler, and the high-pressure stage can be evaluated.

For the low-pressure stage, for mass flow $\dot{m}$,

$$\dot{Q}_L = \dot{W}_L - \dot{m}C_P(T_i - T_L) \qquad (2-18)$$

For the intercooler, for mass flow $\dot{m}$,

$$\dot{Q}_i = \dot{m}C_P(T_i - T_1) \qquad (2-19)$$

For the low-pressure stage, for mass flow $\dot{m}$,

$$\dot{Q}_H = \dot{W}_H - \dot{m}C_P(T_2 - T_1) \qquad (2-20)$$

The power $\dot{W}_L$ and $\dot{W}_H$ can be evaluated by calculating the area of the P-V cycle and T_i, T_1, and T_2 can be calculated by Equation 2-5.

2.3 *Polyphase Induction Motors*

According to Ampere's Law[12], if a magnetic field and a current-carrying conductor are placed in such a spatial relationship as to have components mutually perpendicular to each other, a useful force may be obtained in a direction perpendicular to the magnetic field and to the conductor. Further, if this force appears as a tangential force near the

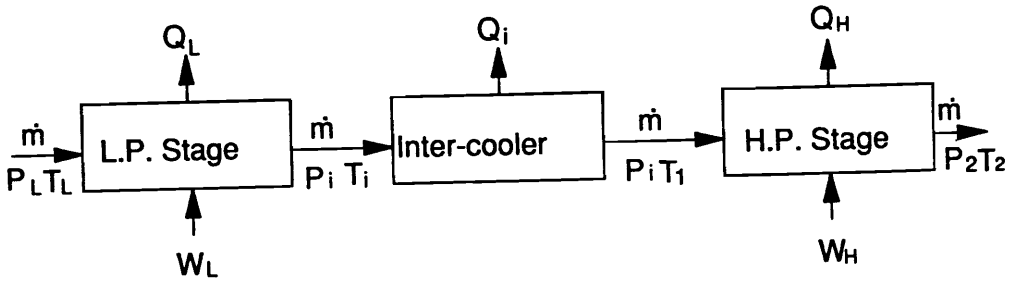

Figure 2-9. Energy Diagram of a Multi-Stage Compressor With Intercooler

periphery of a circumferential structure capable of rotating on a shaft through its center, such as a rotor, a useful torque will be produced. Such an action constitutes a conversion from electrical to mechanical energy and is known as motor action.

The requirements for producing motor action have been accomplished in three different configurations, dc motors, synchronous motors, and induction motors. A dc motor requires a source of dc power to excite the stationary field winding and to supply dc power to the rotating armature winding, through the brushes and commutator. Thus the original cost and the maintenance cost per horsepower are greater for this type of motor than for the other two types mentioned above. Although the dc motor has very good speed-control characteristics, its significantly greater total cost per horsepower has limited its industrial application to a small percentage of total drive-motor horse power.

A synchronous motor requires a source of dc power to excite the rotating field winding, through the brushes and collector rings. For many synchronous motors, for which fine control of the field winding is not required, the field is excited by a rotating alternator, the output of which is rectified by a rotating rectifier bank. However, in neither case, the original cost is greater and the maintenance cost per unit horsepower is generally greater than for an induction motor of the same horsepower rating. Although the synchronous motor can be designed, at an increased cost, to exhibit a leading power factor (i.e. to deliver positive volt-amperes to the ac bus), the application of synchronous motors is limited primarily to driven equipment that can not be permitted a change in speed upon a change in load.

A polyphase induction motor requires only a source of polyphase power. Polyphase voltage, impressed on the stator winding of such a motor, produces a synchronously rotating magnetomotive-force wave which, in turn, produces a synchronously rotating

flux wave. Since the flux wave is traveling at a greater angular velocity than is the rotor structure, the relative motion results in a voltage being induced in the rotor winding. This induced voltage will cause a corresponding rotor current to flow in each phase of the rotor winding, the direction of which is such as to oppose the original influencing agent, the stator bus. The currents in the rotor phases will combine to produce a rotor-current wave, which rotates at an angular velocity that is equal to the difference in velocity between the synchronous flux wave and the rotor structure. The sum of the angular velocity of this rotating rotor-current wave and of the angular velocity of the rotor structure is equal to the synchronous speed. Thus the rotating flux wave, produced by the stator winding, and the rotating rotor-current wave, developed in the rotor winding, are traveling at the same speed as seen from a point on the stator. The rotor current interacts with the stator flux to produce a torque on the rotor structure. Accordingly, the rotor will accelerate until the torque produced by the motor is just equal to the load torque. For the usual application, this will occur at a rotor speed that is slightly less than synchronous speed. The simplicity and inherently high reliability of the polyphase induction motor has generally made it the drive motor of choice throughout the industry.

2.3.1 Power Losses

For Equation (1-6) to be solvable, the power losses of the motor must be quantified.

$$T_L = \frac{\sum_{i=1}^{3} (I_i(t)V_i(t) - P_{lmi}(t))}{\dot{\theta}(t)} - J_S\ddot{\theta}(t) - C_S\dot{\theta}(t) \qquad (1-6)$$

According to Cochran[12], in an induction motor, there are five components of machine power losses:

1. Core loss which consists of following components.

    a. Fundamental core losses.

        1) Magnetic hysteresis loss.

        2) Eddy current loss which caused by eddy currents flowing through a conductor.

    b. Rotational core loss.

        1) High-frequency rotor-surface and stator surface losses.

        2) High-frequency rotor-tooth and stator-tooth pulsation losses.

2. Load loss: Assume that the core loss and friction and windage losses of a polyphase induction motor have been determined accurately from tests. Let rated voltage be applied to the stator winding and let the connected load be such that it is exactly equal to the rating of the machine. Under such rated-load conditions, let the power input to the stator be measured accurately. Also, let the temperature of the stator and rotor windings be determined accurately by some means. With this information available, determine the sum of core loss, friction and windage losses, stator I^2R, and rotor I^2R loss, with the two I^2R losses being adjusted to correspond to the full load operating temperatures of their respective windings. This sum of losses will then be found to be considerably smaller than the difference between the total power deliv-

ered to the stator and the total shaft power delivered to the connected load. This discrepancy on losses, which typically varies from 0.8 to 2.0% of the power rating of the machine, is called stray load loss or, more usually, load loss.

Lacking an analytical expression for the load loss in a induction motor, acceptable values of load loss are usually determined by use of empirical equations which are calibrated by test results. Furthermore, because of the insignificance comparing with other losses[13], the load loss is neglected in the calculation of the output power from the motor in this research.

3. Friction and windage, i.e. mechanical losses, caused by rotation of the rotor body, are sufficiently significant that their effect must be considered. Rotating of the rotor structure results in the production of friction and windage losses which generally equal 1% or more of the output rating of the machine. The friction power losses correspond to the time rate of energy losses that occur in the bearing assemblies and for wound-rotor machines, also at the contact surface between the collector rings, at the terminals of the rotor windings, and the mating brushes.

   Since the damping loss of the shaft system is incorporated in Equation (1-6), the mechanical losses will not be included in the power losses of the motor but attributed to the driven machine.

4. Stator I^2R loss.

5. Rotor I^2R loss.

2.3.2 The Equivalent Circuit of a Three-Phase Induction Motor

It is desirable to have an equivalent circuit of a three-phase induction motor in order to direct the analysis of operation and to facilitate the computation of performance. Del Toro[14] describes a three-phase induction motor as an equivalent circuit shown as Figure 2-10.

All the parameters of the equivalent circuit are expressed on a per-phase base. They are defined as:

V	Line voltage.
I, I_1, I_2, I_3	Currents.
R_1	Stator phase winding resistance.
L_1	Stator phase winding leakage inductance.
R_2'	Rotor resistance.
L_2'	Rotor leakage inductance.
R_c	Core loss resistance.
L_m	Magnetizing inductance.

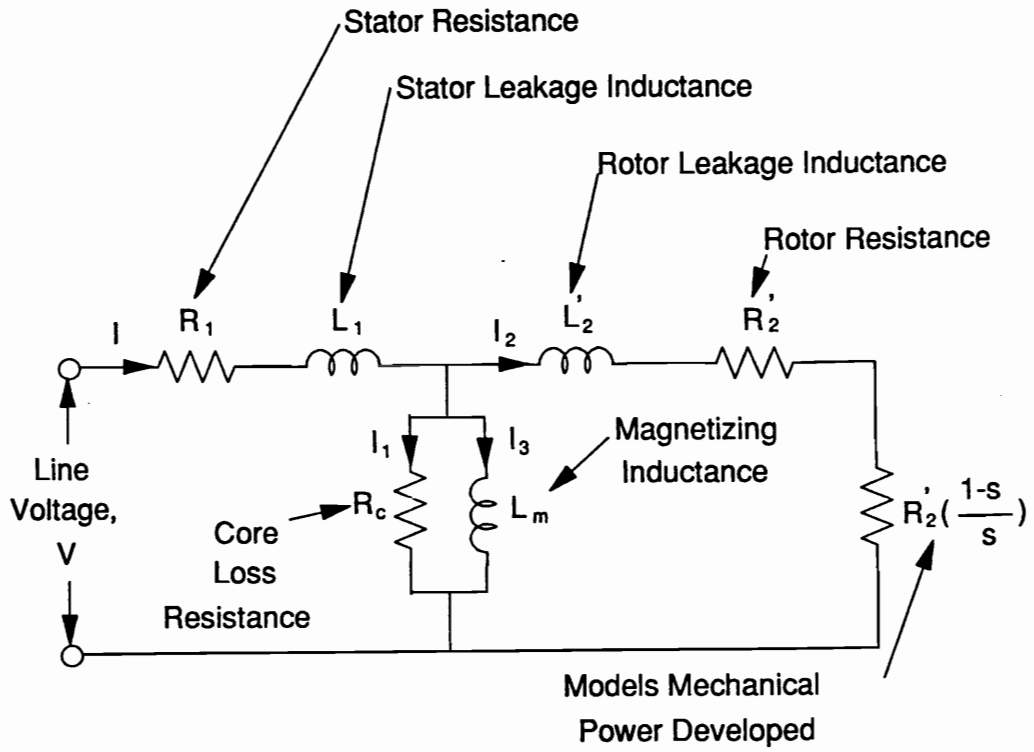

Figure 2-10. Equivalent Circuit of a Three-Phase Induction Motor

s Slip per unit, which is defined as:

$$s = \frac{f_s - f}{f_s} \qquad (2-21)$$

where,

f Rotation speed of the motor.

f_s Syncronous speed of the motor, which is defined as:

$$f_s = \frac{2\omega}{p} \qquad (2-22)$$

where, ω is frequency of the power supply, and p is the number of poles of the stator winding. For this research, the frequency of the power supply is 60 Hertz, and the number of the stator windings is 8. Therefore, the synchronous speed of the motor is 15 Hertz.

A Baldor three-phase AC induction motor, specification shown as Table 2-1, is used in this research. According to Dr. Brockhurst's[15] test, the stator resistance, R_1, and stator leakage inductance held constant as 5.368 Ohms and 0.016 Henry, and the rotor resistance, R_2', rotor leakage inductance, L_2', magnetizing inductance, L_m, and core loss resistance, R_c, change their values when the input power frequency varies. Figure 2-11, 2-12, 2-13, and 2-14 show the curves of R_2', L_2', L_m, and R_c vs. input power frequency.

Table 2-1. Baldor 1/2 Hp Motor Specification

Cat. No.	M3160				
Spec.	35B11-5351				
Frame	56	Ser.	F588		
H.P.	1/2		DP		
Volts	208-230/460				
Amps	3.4-3.2/1.6				
Rpm	850				
Hz	60	Ph.	3	Class	B
Ser. F.	1.15	Des	B	Code	M
Full Load Eff.	64%	P.F.	46%		
Rating	40C Amb-Cont				

2.3.3 Computation of Performance

The use of a power-flow diagram in conjunction with the equivalent circuit makes the computation of the performance of a three-phase induction motor a straightforward matter. Depicted in Figure 2-15.a is power-flow diagram in statement form. Note that the loss quantities are placed on the left side of a flow point. Appearing in Figure 2-15.b is the same power-flow diagram but now expressed in terms of the appropriate relationships needed to compute the performance.

In the steady state of the motor, the slip per unit, s, assumed to be constant through one revolution (the average value to be used), the equivalent circuit can be expressed as shown in Figure 2-16, since the input power is a 60 Hertz AC voltage.

By solving this circuit, I, I_1, I_2 can be expressed as:

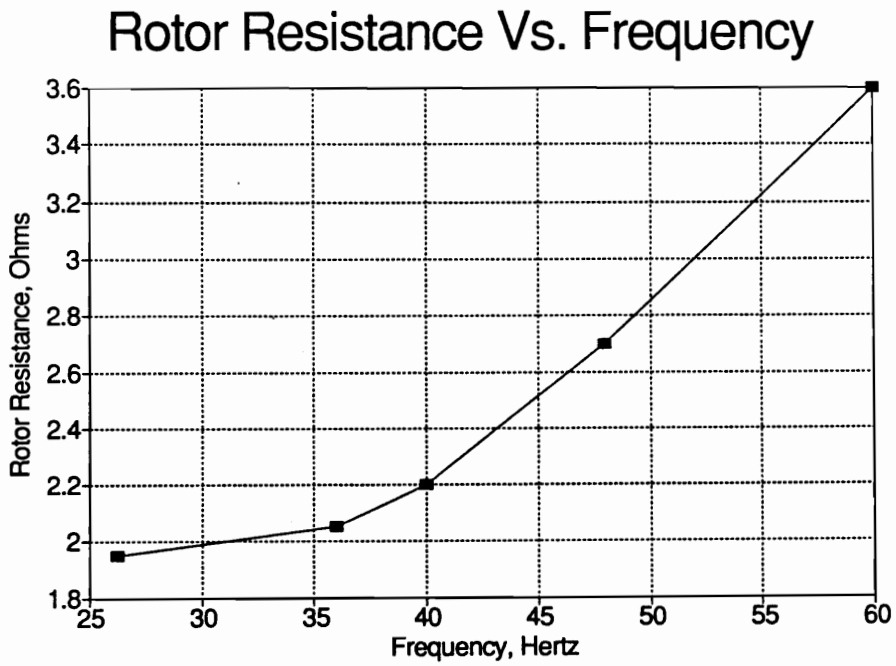

Figure 2-11. Rotor Resistance vs. Frequency

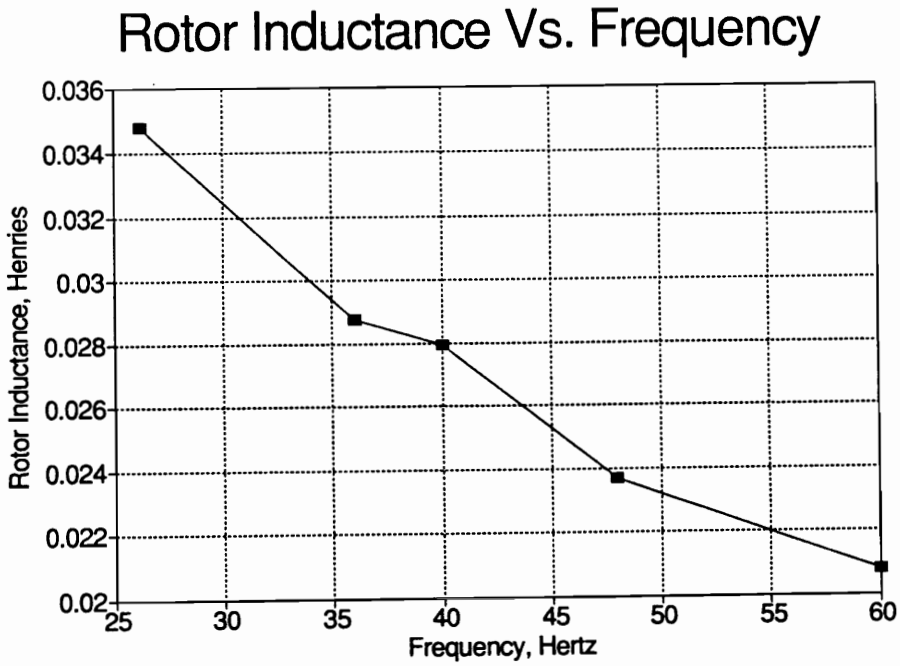

Figure 2-12. Rotor Inductance vs. Frequency

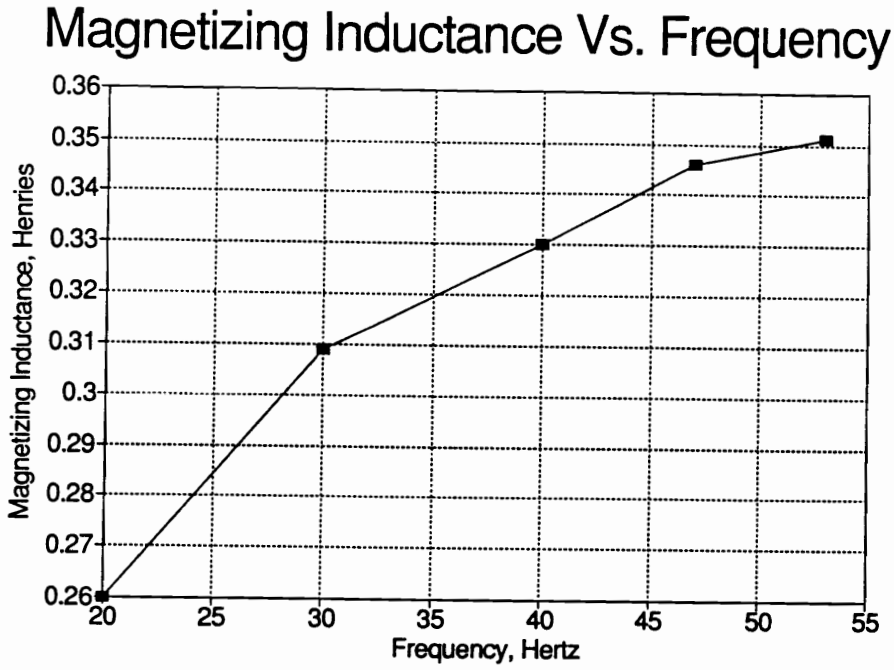

Figure 2-13. Magnetizing Inductance vs. Frequency

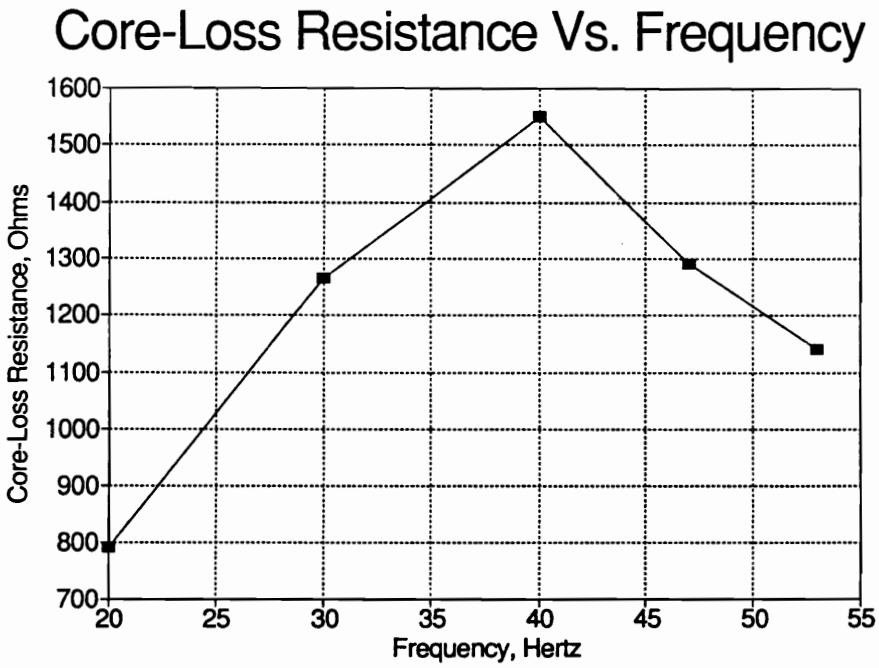

Figure 2-14. Core-Loss Resistance vs. Frequency

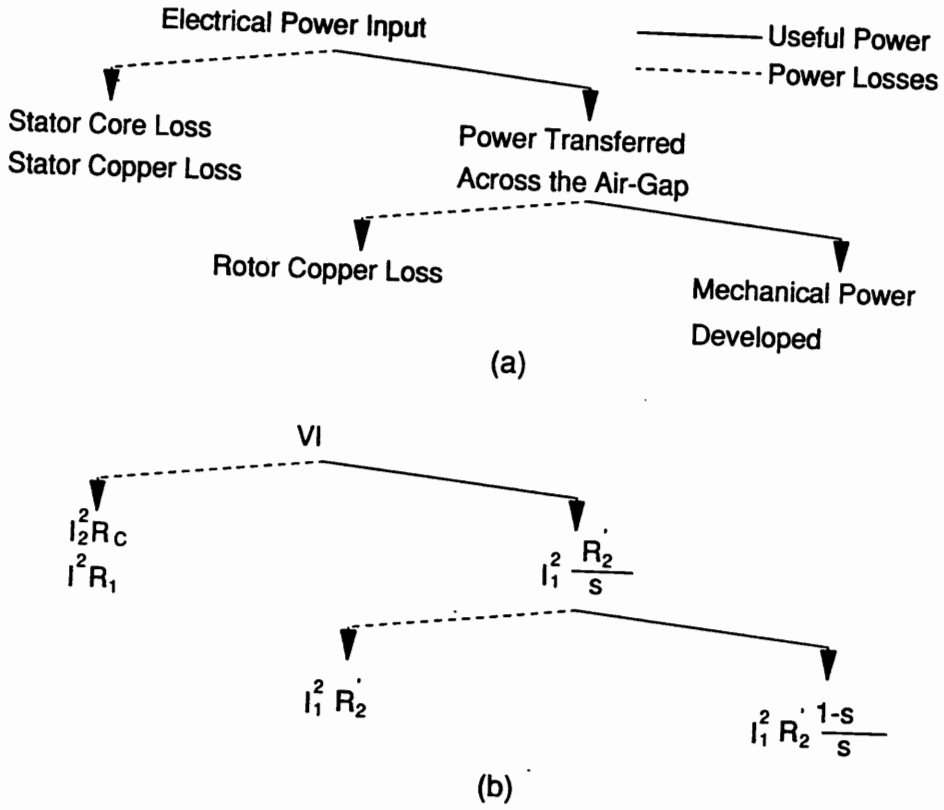

Figure 2-15. Power-Flow Diagram: (a) Statement Form; (b) Equation Form[14]

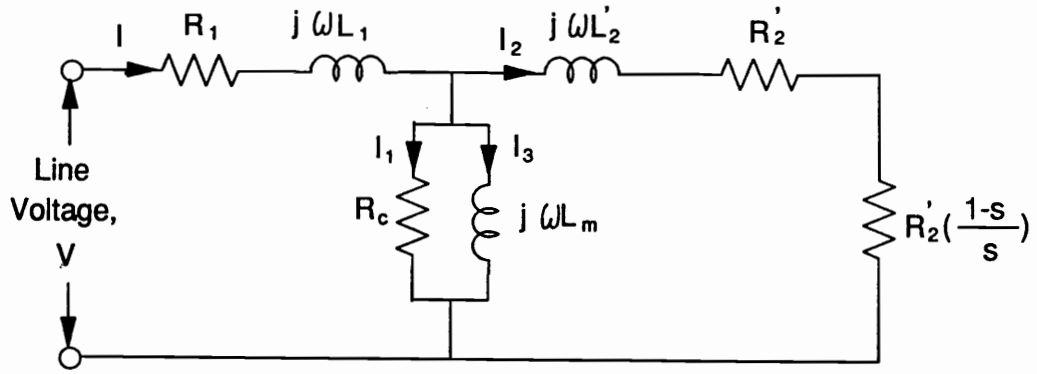

Figure 2-16. Equivalent Circuit of Steady State

$$I = V\left(\frac{Z_R}{Z_R^{\,2} + Z_I^{\,2}} - j\frac{Z_I}{Z_R^{\,2} + Z_I^{\,2}}\right) \qquad (2-23)$$

$$I_1 = \frac{V}{R_c}(b_R - jb_I) \qquad (2-24)$$

$$I_2 = V(c_R - jc_I) \qquad (2-25)$$

where,

$$Z_R = R_1 + \frac{a_R}{a_R^{\,2} + a_I^{\,2}} \qquad (2-26)$$

$$Z_I = \omega L_1 - \frac{a_I}{a_R^{\,2} + a_I^{\,2}} \qquad (2-27)$$

$$a_R = \frac{1}{R_c} + \frac{\frac{R_2'}{s}}{\left(\frac{R_2'}{s}\right)^2 + (\omega L_2')^2} \qquad (2-28)$$

$$a_I = \frac{1}{\omega L_m} + \frac{\omega L_2'}{\left(\frac{R_2'}{s}\right)^2 + (\omega L_2')^2} \qquad (2-29)$$

$$b_R = 1 - \frac{R_1 Z_R + Z_I \omega L_1}{Z_R^{\,2} + Z_I^{\,2}} \qquad (2-30)$$

$$b_I = \frac{Z_R \omega L_1 - Z_I R_1}{Z_R^{\,2} + Z_I^{\,2}} \qquad (2-31)$$

$$c_R = \frac{\frac{R_2'}{s} b_R - \omega L_2' b_I}{(\frac{R_2'}{s})^2 + (\omega L_2')^2} \qquad (2-32)$$

$$c_I = \frac{b_R \omega L_2' + b_I \frac{R_2'}{s}}{(\frac{R_2'}{s})^2 + (\omega L_2')^2} \qquad (2-33)$$

From Equation (2-23), (2-24), and (2-25), the amplitudes and phase differences with the input voltage can be expressed as:

$$AMP(I) = \frac{AMP(V)}{\sqrt{Z_R^2 + Z_I^2}} \qquad (2-34)$$

$$\phi_I = \tan^{-1} \frac{-Z_I}{Z_R} \qquad (2-35)$$

$$AMP(I_1) = \frac{AMP(V)}{R_c} \sqrt{b_R^2 + b_I^2} \qquad (2-36)$$

$$\phi_{I_1} = \tan^{-1} \frac{-b_I}{b_R} \qquad (2-37)$$

$$AMP(I_2) = AMP(V) \sqrt{c_R^2 + c_I^2} \qquad (2-38)$$

$$\phi_{I_2} = \tan^{-1} \frac{-c_I}{c_R} \qquad (2-39)$$

Therefore, the output power of the there phase motor is then determined.

$$P_m = \sum_{i=1}^{3} (I_i V_i - I_i^2 R_{1i} - I_{1i}^2 R_{Ci} - I_{2i}^2 R_{2i}') \qquad (2-40)$$

2.4 References

1. Isermann, Rolf, 1986, *Experiences with Process Fault Detection Methods via Parameter Estimation*, Proceedings of the First European Workshop on Fault Diagnosis, Reliability and Related Knowledge-Based Approaches, Island of Rhodes, Greece.

2. D.T. Dalle Molle and D.M. Himmelblau, 1987, *Fault Detection in an Evaporator via Parameter Estimation in Real Time*, Proceedings of the Second European Workshop on Fault Diagnosis, Reliability and Related Knowledge-Based Approaches, UMIST, Manchester, UK.

3. Williams, J, 1989, *Parameter Identification in a Slider-Crank Mechanism Through Direct Measurement of Shaft Velocity*, Masters Thesis, Virginia Polytechnic Institute and State University, Blacksburg, VA.

4. Pichot, Pierre, 1986, *Compressor Application Engineering, Volume 1, Compression Equipment*, Gulf Publishing Company, Houston, Texas.

5. Easttop, T.D. and McConkey, A., 1986, *Applied Thermodynamics for Engineering Technologists, SI Units, Fourth Edition*, Longman Inc., New York.

6. Nadeem, Tariq, 1988, *Computer Simulation of the Steady-State Thermodynamic Processes and Piston Ring Wear for a Multi-Stage Intercooled Reciprocating Air Compressor*, Masters Thesis, Virginia Polytechnic Institute and State University, Blacksburg, VA,

7. Ruddy, B.L., Dowson, D. and Economou, P.N., 1981, *The Prediction Gas Pressures Within the Ring Packs of Large Bore Diesel Engines*, Journal of Mechanical Engineering Science, 1981, Vol. 23, No. 6.

8. S. Furuhama, M. Takiguchi, K. Kenji, 1981, *Diesel Engine Oil Consumption, pp 63-pp 75*, Society of Automotive Engineers, Inc., Warrendale, PA.

9. Spagnuolo, Antonio, Jr., 1985, *A Study of Reciprocating Compressor Finger Valve Dynamics*, Masters Thesis, Virginia Polytechnic Institute and State University, Blacksburg, VA,

10. Soedel, W., 1972, *Introduction to Computer Simulation of Positive Displacement Compressor: A Short Course Text*, Ray W. Herrick Laboratories, Purdue University.

11. Harris, C.M., 1988, *Shock and Vibration Handbook*, McGraw-Hill Book Company.

12. Cochran, Paul L., 1989, *Polyphase Induction Motor, Analysis, Design, and Application*, Marcel Dekker, Inc., New York.

13. Bourne, R., *No Load Method of Estimating Stray Load Loss in Small Cage Induction Motors*, IEEE Proceedings, Vol. 136, No. 2, March, 1989.

14. Del Toro, Vincent, 1990, *Basic Electric Machines*, Prentice-Hall, Inc., New Jersey.

15. Brockhurst, Frederick, 1991, Professor of Electric Engineering, Rose-Hulman Polytechnic Institute, Terre-Haute, Indiana.

3.0 Theoretical Basis

In the first section of this chapter, the position, velocity, and acceleration of the slider-crank mechanism of an air compressor are derived by using complex analysis. Also, with the kinematic construction of the slider-crank and the dynamics of the crankshaft known, by analyzing the free body diagrams with force and torque equilibriums, the theoretical load torque is expressed as a function of the inertia of the slider-crank mechanism, and the internal pressure of the cylinder of the air compressor, and the effect of the friction force between the piston rings and the cylinder wall. The solution techniques of a linear equation system of the system parameters and a non-linear equation system of the pressure-volume characteristic parameters the air compressor system are discussed in the final section.

3.1 *Kinematic Analysis by Complex Numbers*

On a plane, link L rotates about a fixed axis O as shown in Figure 3-1[1]. The position of particle P on link L may be expressed by the vector $\vec{r}_P$. It is desired to determine the velocity and acceleration vectors $\dot{\vec{r}}_P$ and $\ddot{\vec{r}}_P$ of particle P when the link L is in the phase given by θ and the known instantaneous angular velocity and angular acceleration are $\dot{\theta}$ and $\ddot{\theta}$.

According to Mabie[1], the position vector $\vec{r}_P$ may be expressed as a complex number:

$$\begin{aligned} \vec{r}_P &= Re^{i\theta} \\ &= R\cos\theta + iR\sin\theta \end{aligned} \qquad (3-1)$$

Differentiation of Equation (3-1) yields the velocity vector $\dot{\vec{r}}_P$,

$$\begin{aligned} \dot{\vec{r}}_P &= iR\dot{\theta}e^{i\theta} \\ &= R\dot{\theta}e^{i(\theta+\pi/2)} \\ &= -R\dot{\theta}\sin\theta + iR\dot{\theta}\cos\theta \end{aligned} \qquad (3-2)$$

As shown in Figure 3-1, the direction of the velocity vector $\dot{\vec{r}}_P$ is given by the angle $(\theta + \pi/2)$ and is shown at an angle 90° greater than the angle of vector $\vec{r}_P$ and the magnitude of the velocity vector is $R\dot{\theta}$.

Differentiation of the velocity Equation (3-2) gives the acceleration vector $\ddot{\vec{r}}_P$ as:

$$\begin{aligned} \ddot{\vec{r}}_P &= iR\ddot{\theta}e^{i\theta} - R\dot{\theta}^2e^{i\theta} \\ &= R\dot{\theta}e^{i(\theta+\pi/2)} + R\dot{\theta}^2e^{i(\theta+\pi)} \\ &= -R(\ddot{\theta}\sin\theta + \dot{\theta}^2\cos\theta) + iR(\ddot{\theta}\cos\theta - \dot{\theta}^2\sin\theta) \end{aligned} \qquad (3-3)$$

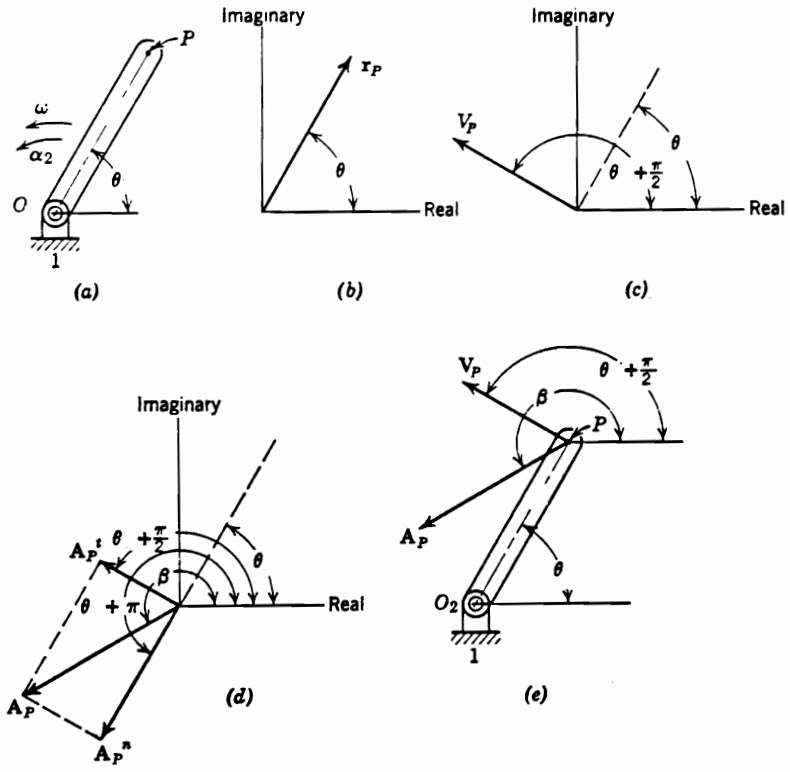

Figure 3-1. Position, Velocity, and Acceleration of a Link on Plane[1]

In Equation (3-3), the acceleration vector consists of the tangential component, $\vec{r}_P^t$, of magnitude $R\ddot{\theta}$ and direction 90° greater than θ, and normal component, $\vec{r}_P^n$, of magnitude $R\dot{\theta}^2$ and direction 180° greater than θ as shown in Figure 3-1. The acceleration vector $\vec{r}_P$ is the resultant of the sum of these two perpendicular vectors.

3.1.1 Kinematic Analysis of a Slider-Crank Mechanism

Figure 3-2 shows a slider-crank mechanism with crank radius of R, and connecting rod length, L, connected to a piston. The centers of gravity of the crank and the connecting rod are also indicated. The instantaneous angular position, angular velocity, and angular acceleration of the crankshaft are expressed as θ, $\dot{\theta}$, and $\ddot{\theta}$. The instantaneous position and acceleration of the piston and the instantaneous acceleration of the center of gravity of the connecting rod to the fixed point O_2 are to be determined.

As shown in Figure 3-2, the position of the piston, namely, particle B relative to fixed point O_2 given by vector $\vec{X}$ can be expressed as the resultant of the position vector of the crank-pin bearing, namely, particle A relative to the fixed point O_2, $\vec{R}$, and the position vector of particle B relative to particle A, $\vec{L}$.

$$\vec{X} = \vec{R} + \vec{L} \qquad (3-4)$$

If the vectors are to be represented by complex numbers, real and imaginary axes shown as Figure 3-2.b, Equation (3-4) can be written as:

$$X = Re^{i\theta} + Le^{i\beta} \qquad (3-5)$$

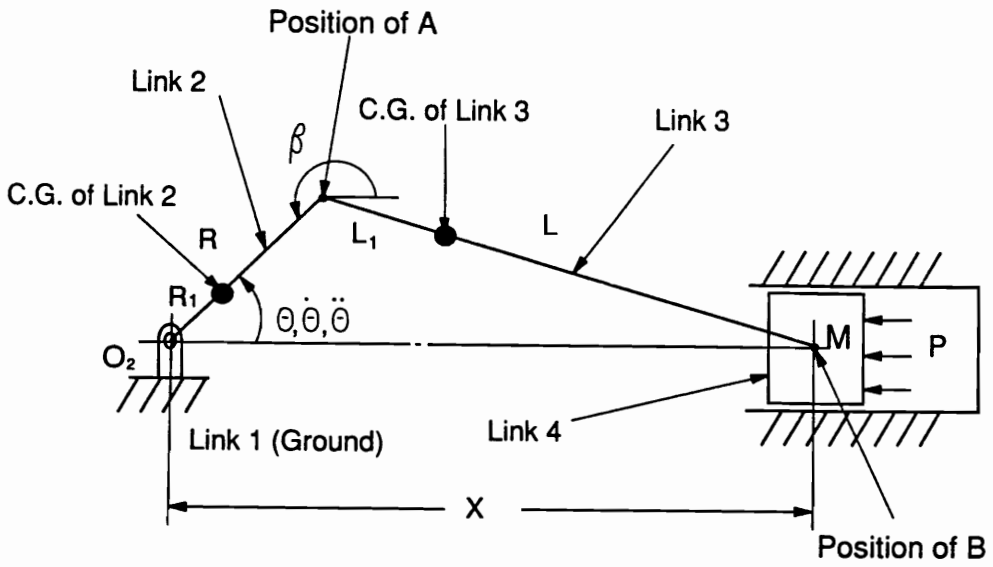

Figure 3-2. Slider-Crank Mechanism with Piston and Cylinder

where R and L are the fixed lengths of link 2 and 3 and X is a variable length giving the position of the slider.

Two successive differentiations of Equation (3-5) yield expressions giving the velocity $\dot{X}$ and acceleration $\ddot{X}$ as:

$$\dot{X} = iR\dot{\theta}e^{i\theta} + iL\dot{\beta}e^{i\beta} \qquad (3-6)$$

$$\ddot{X} = iR\ddot{\theta}e^{i\theta} - R\dot{\theta}^2e^{i\theta} + iL\ddot{\beta}e^{i\beta} - L\dot{\beta}^2e^{i\beta} \qquad (3-7)$$

Equation (3-5), (3-6), and (3-7) can be expanded to real and imaginary parts. Therefore, the instantaneous angular position, angular velocity, and angular acceleration of the connecting rod, β, $\dot{\beta}$, and $\ddot{\beta}$ and the instantaneous position, velocity, and acceleration of the reciprocating mass, X, $\dot{X}$, and $\ddot{X}$ can be solved.

$$\beta = \sin^{-1}\left(\frac{-R}{L}\sin\theta\right) \qquad (3-8)$$

$$X = R\cos\theta + L\cos\beta \qquad (3-9)$$

$$\dot{\beta} = -\dot{\theta}\left(\frac{R\cos\theta}{L\cos\beta}\right) \qquad (3-10)$$

$$\dot{X} = -R\dot{\theta}\sin\theta - L\dot{\beta}\sin\beta \qquad (3-11)$$

$$\ddot{\beta} = \frac{R(\dot{\theta}^2\sin\theta - \ddot{\theta}\cos\theta) + L\dot{\beta}^2\sin\beta}{L\cos\beta} \qquad (3-12)$$

$$\ddot{X} = -R(\dot{\theta}^2\cos\theta + \ddot{\theta}\sin\theta) - L(\dot{\beta}^2\cos\beta + \ddot{\beta}\sin\beta) \qquad (3-13)$$

Similarly, the position, velocity, and acceleration of the center of gravity of the connecting rod can be written as complex form:

$$\vec{R_3} = Re^{i\theta} + L_1 e^{i\beta} \tag{3-14}$$

$$\dot{\vec{R}}_3 = iR\dot{\theta}e^{i\theta} + iL_1\dot{\beta}e^{i\beta} \tag{3-15}$$

$$\ddot{\vec{R}}_3 = iR\ddot{\theta}e^{i\theta} - R\dot{\theta}^2 e^{i\theta} + iL_1\ddot{\beta}e^{i\beta} - L_1\dot{\beta}^2 e^{i\beta} \tag{3-16}$$

The imaginary and real components of acceleration of the center of gravity of the connecting rod, A_{R3X} and A_{R3Y}, can be obtained by expanding Equation (3-16).

$$A_{R3X} = -R(\dot{\theta}^2 \cos\theta + \ddot{\theta}\sin\theta) - L_1(\dot{\beta}^2\cos\beta + \ddot{\beta}\sin\beta) \tag{3-17}$$

$$A_{R3Y} = -R(\dot{\theta}^2 \sin\theta - \ddot{\theta}\cos\theta) - L_1(\dot{\beta}^2\sin\beta - \ddot{\beta}\cos\beta) \tag{3-18}$$

3.2 Force and Torque Analysis

3.2.1 Inertia of Slider-Crank Mechanism

According to Newton's Second Law of Motion[1], it is known that following equations apply for a rigid body in general motion.

$$\sum \vec{F} = M\vec{A_g} \tag{3-19}$$

$$\sum \vec{T} = J\vec{\alpha} \qquad (3-20)$$

in which $\sum \vec{F}$ is the vector sum of a system consisting of n forces acting on the body in the plane of motion; M is the mass of the body; $\vec{A}_g$ is the acceleration of the center of gravity of the body; $\sum \vec{T}$ is the sum of moments of the forces and torques about the axis of rotation; J is the moment of inertia of the body with respect to the axis of rotation; and $\vec{\alpha}$ is the angular acceleration of the body relative to the axis of rotation. Furthermore, by definition[2], the moment of a plane force, $\vec{F}$, acting on a rigid body about the axis of rotation is expressed:

$$\vec{T} = \vec{r} \times \vec{F} \qquad (3-21)$$

where $\vec{r}$ is the position vector of the point of action of the force relative to the rotation axis.

Figure 3-3[1] shows the free body diagrams of the crank of mass, M_2, and mass moment of inertia with respect to the center of gravity of the crank, J_2, connecting rod of mass, M_3, and mass moment of inertia with respect to the center of gravity of the connecting rod, J_3, and piston of mass, M. With all the kinematic construction (geometric dimension of the mechanism) and dynamics of the crankshaft (angular position, angular velocity, and angular acceleration) known and all the required dynamics of the slider mass (position and acceleration) and the connecting rod (angular acceleration and acceleration of the center of gravity) calculated in previous section, the required input torque,

---

[1] The first subscript of the force indicates the number of the link which originates the force, the second subscript denotes the number of the link which is acted upon by the force, and the third subscript is the direction of the force. For example, F_{32X} means the force that the connecting rod imposes on the crankshaft in X direction.

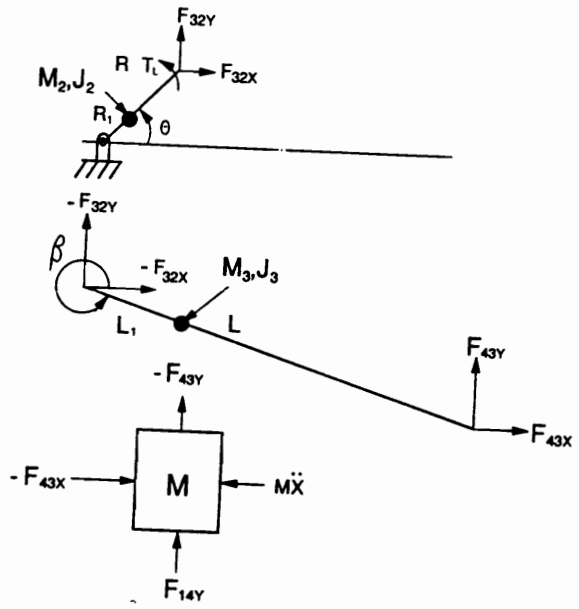

Figure 3-3. Free Body Diagrams of the Crankshaft, Connecting Rod and Piston

T_L, is to be expressed as a function of the machine condition parameters (masses of the slider and connecting rod, mass moments of inertia of the crank and the connecting rod, eccentricity of the crank, friction force of the piston ring against the cylinder wall, and the pressure difference across the piston).

By defining T_{LM} as the required input torque contributed by the masses of the crank, connecting rod, and piston and the mass moments of the crank and connecting rod, from the free body diagram, the force and torque equilibrium equations can be constructed as:

$$RF_{32Y}\cos\theta - RF_{32X}\sin\theta + R_1M_2g\sin\theta + T_{LM} = (J_2 + R_1{}^2M_2)\ddot{\theta} \qquad (3-22)$$

$$F_{43X} - F_{32X} - M_3g = M_3A_{R3X} \qquad (3-23)$$

$$F_{43Y} - F_{32Y} = M_3A_{R3Y} \qquad (3-24)$$

$$LF_{43Y}\cos\beta - LF_{43X}\sin\beta + L_1M_3g\sin\beta = (J_3 + L_1{}^2M_3)\ddot{\beta} \qquad (3-25)$$

$$F_{14Y} - F_{43Y} = 0 \qquad (3-26)$$

$$-F_{43X} - Mg = M\ddot{X} \qquad (3-27)$$

Solving Equations 3-22 through 3-27 simultaneously yields:

$$
\begin{aligned}
T_{LM} = {} & J_2'\ddot{\theta} - E_2 g \sin\theta \\
& + MR(\ddot{X} + g)(\tan\beta\cos\theta - \sin\theta) \\
& + M_3 R(A_{R3Y}\cos\theta - A_{R3X}\sin\theta - g\sin\theta + \frac{L_1}{L} g\tan\beta\cos\theta) \\
& - J_3' \frac{R\ddot{\beta}\cos\theta}{L\cos\beta}
\end{aligned}
\qquad (3-28)
$$

where J_2' is the mass moment of inertia of the crank with respect to the crankshaft,

$$J_2' = J_2 + R_1^2 M_2 \qquad (3-29)$$

J_3' is the mass moment of inertia of the connecting rod with respect to the crank-pin bearing,

$$J_3' = J_3 + L_1^2 M_3 \qquad (3-30)$$

and E_2 is the eccentricity of the crank with respect to the crankshaft and defined as:

$$E_2 = R_1 M_2 \qquad (3-31)$$

3.2.1.1 Simplified Model of the Slider-Crank Mechanism

From Equation (3-28), it is noticed that if the kinematic structure of the crankshaft mechanism and the dynamics of the rotation system are known, five parameters are needed to be quantified to describe the slider-crank mechanism, the mass of the crank, the mass moment of inertia of the crank with respect to the center of gravity of the crank, the mass of the connecting rod, the mass moment of inertia of the connecting rod

with respect to the center of gravity of itself, and the reciprocating mass. In order to reduce calculation effort, as in Mabie and Reinholtz[1], a simplified model is used to describe a slider-crank mechanism, using two masses lumped at wrist-pin bearing and crank-pin bearing to approximate the mass distribution of the connecting rod.

For a slider-crank mechanism, according to Mabie and Reinholtz[1], the mass of connecting rod, M_3, can be represented as two lumped masses, M_{31} and M_{32}, such that:

$$M_3 = M_{31} + M_{32} \tag{3-32}$$

$$M_{31}L_1 = M_{32}L_2 \tag{3-33}$$

$$J_3 = M_{31}L_1^2 + M_{32}L_2^2 \tag{3-34}$$

to make M_3 and M_{31} plus M_{32} kinematically equivalent, where J_3 is the inertia of moment of the connecting rod with respect to the center of gravity of the connecting rod; L_1 and L_2 represent the distances from the center of gravity of the connecting rod to the lumped mass M_{31} and lumped mass M_{32}.

Usually, one of the distance L_1 or L_2 is arbitrarily chosen and the other quantities are calculated using the above expressions. According to Mabie and Reinholtz, the usual practice is to place one of the equivalent masses on the wrist-pin bearing. The location of the other mass is then determined from the equations above. Because of the shape of the connecting rod, its center of gravity is very near the crank-pin bearing. Therefore, the second equivalent mass can be placed on the crank-pin bearing without great error. Then, the masses M_{31} and M_{32} can be approximately expressed as:

$$M_{31} = M_3 \frac{L_2}{L_1 + L_2} \tag{3-35}$$

$$M_{32} = M_3 \frac{L_1}{L_1 + L_2} \qquad (3-36)$$

Figure 3-4 shows the mass distribution of the connecting rod.

To balance the inertia effect of mass M_{31}, a counter weight is attached to the crank such that the mass center is at the axis of rotation. M_{32} is then incorporated into the reciprocating mass, M to make:

$$M = M_{32} + M_p \qquad (3-37)$$

where, M_p is the mass of the piston.

Therefore, in Equation (3-28), the load torque contributed by the crankshaft mechanism, T_{LM}, can be simplified as:

$$T_{LM} = J_2\ddot{\theta} + MR(\ddot{X} + g)(\tan\beta\cos\theta - \sin\theta) \qquad (3-38)$$

3.2.1.2 Comparison of the 'Exact' Model and the Simplified Model

The title 'exact model' means the model of continuously distributed mass of the connecting rod and is in comparison to the simplified model of lumped masses of the connecting rod described above. From Equation (3-28), for the 'exact' model, the required input torque contributed by the connecting rod can be expressed as:

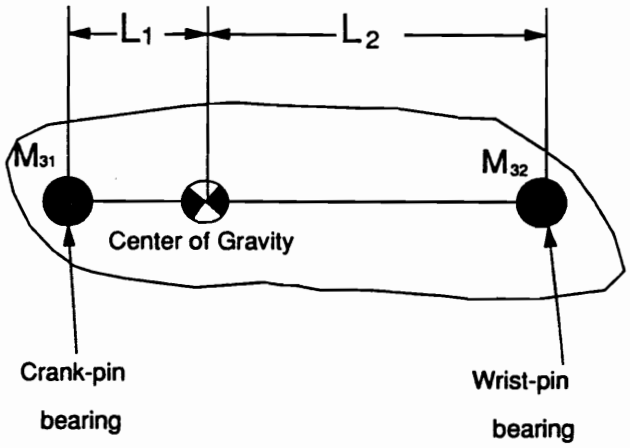

Figure 3-4. Mass Distribution of the Connecting Rod

$$T_{EX} = M_3 R(A_{R3Y}\cos\theta - A_{R3X}\sin\theta - g\sin\theta + \frac{L_1}{L} g\tan\beta\cos\theta) - \frac{R\ddot{\beta}\cos\theta}{L\cos\beta}(J_3 + M_3 L_1{}^2) \quad (3-39)$$

and for the simplified model:

$$T_{SI} = R^2 M_{31}\ddot{\theta} + M_{32}R(\ddot{X}+g)(\tan\beta\cos\theta - \sin\theta) \quad (3-40)$$

The slider-crank mechanism with kinematic construction specification shown as Table 3-1 was utilized to compare the difference between Equation (3-39) and (3-40). The angular velocity and angular acceleration histories of the crankshaft through one complete cycle shown as Figure 3-5 and 3-6 (the data were acquired with the single-stage air compressor with cylinder head off, driven by a 1/2 horsepower three-phase induction motor).

Figure 3-7 and 3-8 compare these two models in the time and frequency domain (the time reference is the angular position of the crankshaft and the period of one complete cycle of crankshaft is 0.0677 second). The dominant components in frequency domain for both signals are the first three harmonics. It is noticed that there are significant differences for both signals of the first and the third harmonics. Therefore, the continuously distributed mass model of the connecting rod is to be adopted to more accurately estimate the machine condition parameters in the solution algorithm.

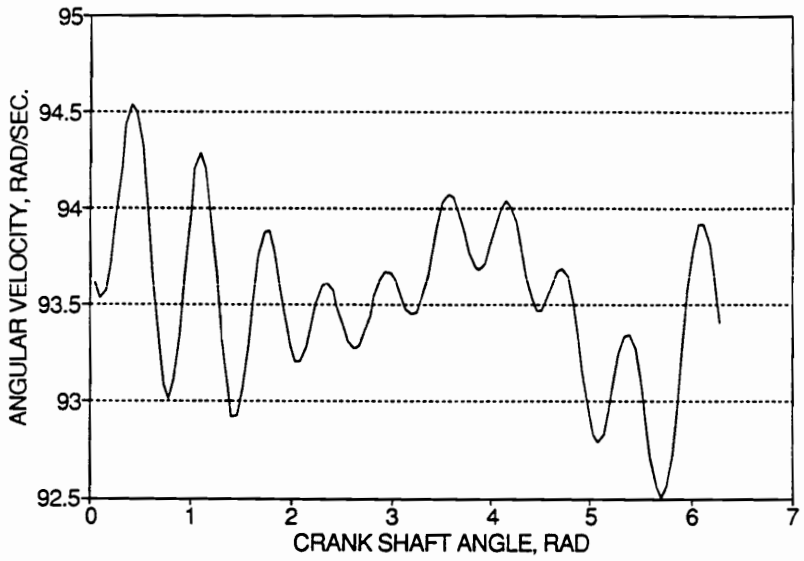

Figure 3-5. Angular Velocity History of the Crank Shaft through One Cycle

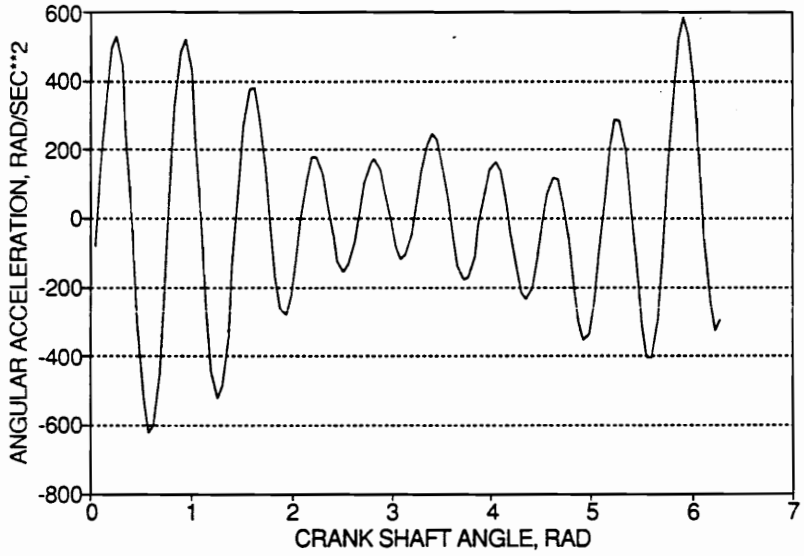

Figure 3-6. Angular Acceleration History of the Crank Shaft through One Cycle

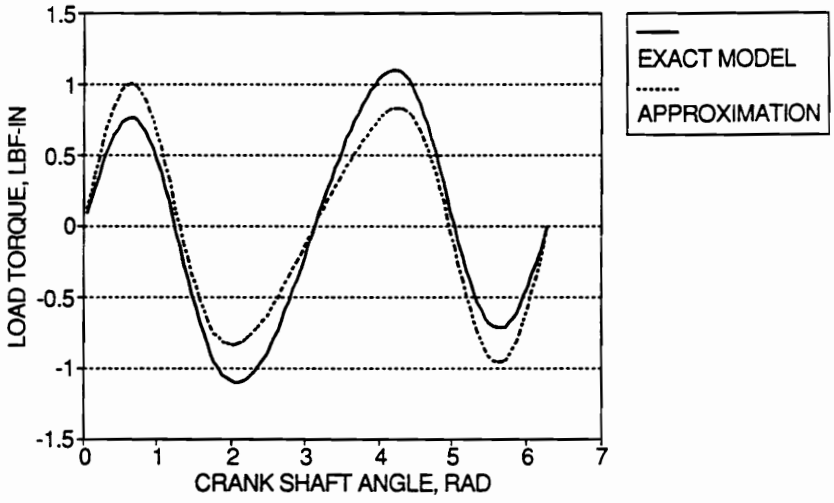

Figure 3-7. Load Torque Caused by Connecting Rod in Time Domain

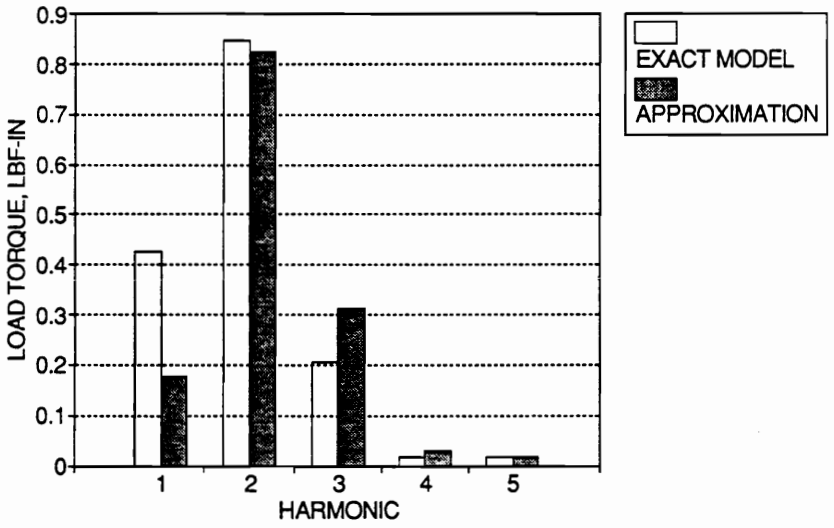

Figure 3-8. Load Torque Caused by Connecting Rod in Frequency Domain

Table 3-1. Specification of Slider-Crank Mechanism

Crank Radius, R	1.0 in
Connecting Rod Length, L	4.0 in
Position of C.G. of Connecting Rod, L_1	1.25 in
Connecting Rod Mass, M_3	0.228 lbm
Mass Moment of Inertia of Connecting Rod, J_3'	0.394 lbm-in^2
Lumped Mass at Crank-Pin bearing, M_{31}	0.157 lbm
Lumped Mass at Wrist-Pin bearing, M_{32}	0.0712 lbm

3.2.2 Internal Pressure of the Cylinder

In Figure 3-3, substituting the effect of the inertia of the slider-crank mechanism by the pressure difference across the piston, ΔP, the required input torque contributed by the pressure difference across the piston, T_{LP}, can be derived.

$$T_{LP} = R(\tan\beta\cos\theta - \sin\theta)A\Delta P \qquad (3-41)$$

where, A is the cross area of the piston.

In order to evaluate T_{LP} in Equation 3-41, the cylinder pressure can be expressed as a function of the angular position of the crankshaft, θ. For a reciprocating air compressor, the pressure-volume and pressure-angle diagrams for a complete cycle are shown in Figure 3-9, where:

θ_1 Beginning of expansion = 0

θ_2 End of expansion and the beginning of suction

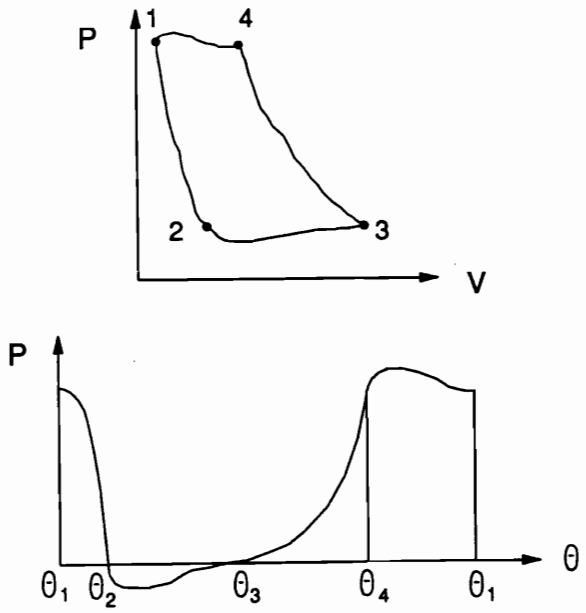

Figure 3-9. A Complete Cycle for a Reciprocating Compressor

θ_3 End of the suction and the beginning of compression = π

θ_4 End of compression and the beginning of discharge

θ_1 End of discharge = 2π

Zone 1-2 Expansion

Zone 2-3 Intake

Zone 3-4 Compression

Zone 4-1 Discharge

According to Easttop and McConkey[3], during expansion and compression of air, the pressure-volume relationship can be assumed as polytropic:

$$PV^{\kappa} = constant \qquad (3-42)$$

where κ is the expansion constant of air and V is the volume in the cylinder which can be evaluated as:

$$V = A\left(R + L + L_C - R\cos\theta - \sqrt{L^2 - R^2\sin^2\theta}\right) \qquad (3-43)$$

where,

A Cross section area of the piston.

R Crank radius.

L Connecting rod length.

L_C Clearance length.

θ Crankshaft angle with the reference of the position of top dead center.

For an ideal compression cycle, the pressures of the intake and discharge processes are assumed as constant. However, as discussed by Pichot[4], due to the inertia of the air flow and the effect of the valves, pressure fluctuations occur during the intake and discharge procedures. Therefore, the pressures during the discharge and intake can be expressed as the sum of the average and harmonic terms.

$$P_{discharge} = P_{out} + a_1 \sin(\theta^*) + a_2 \sin(2\theta^*) + \cdots \qquad (3-44)$$

$$P_{intake} = P_{in} - b_1 \sin(\theta^{**}) - b_2 \sin(2\theta^{**}) - \cdots \qquad (3-45)$$

where,

P_{out} Pressure at which the discharge valve opens.

P_{in} Pressure at which the intake valve opens.

a_1, a_2, b_1, b_2 Harmonic amplitudes of pressure fluctuations during discharge and intake.

θ^*, θ^{**} Scaled angles to express the durations of discharge and intake as a half harmonic period, π. Mathematically,

$$\theta^* = \pi\left(\frac{\theta - \theta_4}{2\pi - \theta_4}\right) \tag{3-46}$$

$$\theta^{**} = \pi\left(\frac{\theta - \theta_2}{\pi - \theta_2}\right) \tag{3-47}$$

The other alternative expression of the pressure fluctuations is polynomial forms; the pressures during the discharge and intake can be expressed as:

$$P_{discharge} = P_{out} + a_1(\theta - \theta_4) + a_2(\theta - \theta_4)^2 + \cdots \tag{3-48}$$

$$P_{intake} = P_{in} - b_1(\theta - \theta_2) - b_2(\theta - \theta_2)^2 - \cdots \tag{3-49}$$

Since the initial approximations and bounds are needed for the machine condition parameters (these will be discussed in next section) and there is not enough information to set the initial approximations and bounds for the polynomial coefficients, pressures of intermediate points between θ_4 and 2π in Figure 3-9 are needed to evaluate the coefficients, $a_1, a_2, \ldots$ by using a linear equation set solver:

$$\begin{bmatrix} a_1 \\ a_2 \\ \dots \\ a_n \\ a_{n+1} \end{bmatrix} = \begin{bmatrix} (\theta_{o1}-\theta_4) & (\theta_{o1}-\theta_4)^2 & \dots & (\theta_{o1}-\theta_4)^{n+1} \\ (\theta_{o2}-\theta_4) & (\theta_{o2}-\theta_4)^2 & \dots & (\theta_{o2}-\theta_4)^{n+1} \\ \dots & \dots & \dots & \dots \\ (\theta_{on}-\theta_4) & (\theta_{on}-\theta_4)^2 & \dots & (\theta_{on}-\theta_4)^{n+1} \\ (2\pi-\theta_4) & (2\pi-\theta_4)^2 & \dots & (2\pi-\theta_4)^{n+1} \end{bmatrix}^{-1} \begin{bmatrix} (P_{o1}-P_{out}) \\ (P_{o2}-P_{out}) \\ \dots \\ (P_{on}-P_{out}) \\ 0 \end{bmatrix} \qquad (3-50)$$

where, $\theta_{o1}, \theta_{o1}, \dots, \theta_{on}$ are the n intermediate points between θ_4 and 2π and $P_{o1}, P_{o2}, \dots, P_{on}$ are the corresponding pressures.

With same procedure described above, the polynomial coefficients $b_1, b_2, \dots$ can be expressed as:

$$\begin{bmatrix} b_1 \\ b_2 \\ \dots \\ b_n \\ b_{n+1} \end{bmatrix} = \begin{bmatrix} -(\theta_{i1}-\theta_2) & -(\theta_{i1}-\theta_2)^2 & \dots & -(\theta_{i1}-\theta_2)^{n+1} \\ -(\theta_{i2}-\theta_2) & -(\theta_{i2}-\theta_2)^2 & \dots & -(\theta_{i2}-\theta_2)^{n+1} \\ \dots & \dots & \dots & \dots \\ -(\theta_{in}-\theta_2) & -(\theta_{in}-\theta_2)^2 & \dots & -(\theta_{in}-\theta_2)^{n+1} \\ -(\pi-\theta_2) & -(\pi-\theta_2)^2 & \dots & -(\pi-\theta_2)^{n+1} \end{bmatrix}^{-1} \begin{bmatrix} (P_{i1}-P_{in}) \\ (P_{i2}-P_{in}) \\ \dots \\ (P_{in}-P_{in}) \\ 0 \end{bmatrix} \qquad (3-51)$$

where, $\theta_{i1}, \theta_{i1}, \dots, \theta_{in}$ are the n intermediate points between θ_2 and π and $P_{i1}, P_{i2}, \dots, P_{in}$ are the corresponding pressures.

According to the derivation above, it is concluded that it would be more efficient to express the pressure fluctuations with scaled harmonic terms than with a polynomial, because:

1. Experiments proved that it takes more calculation effort to determine polynomial coefficients than harmonic amplitudes.

2. The harmonic amplitudes correspond more closely to the physical phenomena under consideration than the polynomial coefficients.

3.2.3 Friction Force

During the operation of the air compressor, there are two friction forces which affect the required load torque:

1. The friction force caused by the piston ring against the cylinder wall.

2. The friction force caused by the piston side thrust force against the cylinder wall.

As discussed in Chapter 2, the friction force of the piston ring against the cylinder wall may be assumed to be a force with a constant magnitude, F_r, and a direction opposite to the velocity of the slider mass, $\dot{X}$. Then, the load torque contributed by the friction force of the piston rings against the cylinder wall, T_{LF}, can be derived with the procedure described in previous section.

$$T_{LF} = R(\tan\beta\cos\theta - \sin\theta)F_r\frac{abs(\dot{X})}{\dot{X}} \qquad (3-52)$$

Assuming the kinetic friction coefficient of the piston upon the cylinder wall is a constant, f, the friction force caused by the piston side thrust force against the cylinder wall is proportional to the absolute value of the piston side thrust force and with a direction opposite to that of the slider.

Considering the inertia of the slider-crank mechanism only, the free body diagram shown in Figure 3-3 can be reconstructed as in Figure 3-10 and the equilibrium equations are to be rewritten as:

$$RF_{32Y}\cos\theta - RF_{32X}\sin\theta + E_2 g\sin\theta + T_{LM}^{f} = J_2'\ddot{\theta} \qquad (3-53)$$

$$F_{43X} - F_{32X} - M_3 g = M_3 A_{R3X} \qquad (3-54)$$

$$F_{43Y} - F_{32Y} = M_3 A_{R3Y} \qquad (3-55)$$

$$LF_{43Y}\cos\beta - LF_{43X}\sin\beta + L_1 M_3 g\sin\beta = J_3'\ddot{\beta} \qquad (3-56)$$

$$F_{14Y} - F_{43Y} = 0 \qquad (3-57)$$

$$-F_{43X} - Mg - f\,abs(F_{14Y})\frac{abs(\dot{X})}{\dot{X}} = M\ddot{X} \qquad (3-58)$$

From Equations 3-53 through 3-58, the load torque contributed by the inertia of the slider-crank mechanism, T_{LM}^{f}, can be solved.

$$\begin{aligned} &\text{if } F_{14Y} \geq 0 \text{ and } \dot{X} \geq 0 \\ &\text{or } F_{14Y} < 0 \text{ and } \dot{X} < 0 \end{aligned} \qquad (3-59)$$

$$\begin{aligned} T_{LM}^{f} = {} & J_2'\ddot{\theta} - E_2 g\sin\theta \\ & + MR(\ddot{X}+g)\left(\frac{\cos\theta\sin\beta + f\sin\theta\sin\beta}{L\cos\beta + fL\sin\beta} - \sin\theta\right) \\ & + M_3 R\left(A_{R3Y}\cos\theta - A_{R3X}\sin\theta - g\sin\theta + \frac{L_1 g\cos\theta\sin\beta + fL_1 g\sin\theta\sin\beta}{L\cos\beta + fL\sin\beta}\right) \\ & - J_3' R\ddot{\beta}\frac{\cos\theta + f\sin\theta}{L\cos\beta + fL\sin\beta} \end{aligned}$$

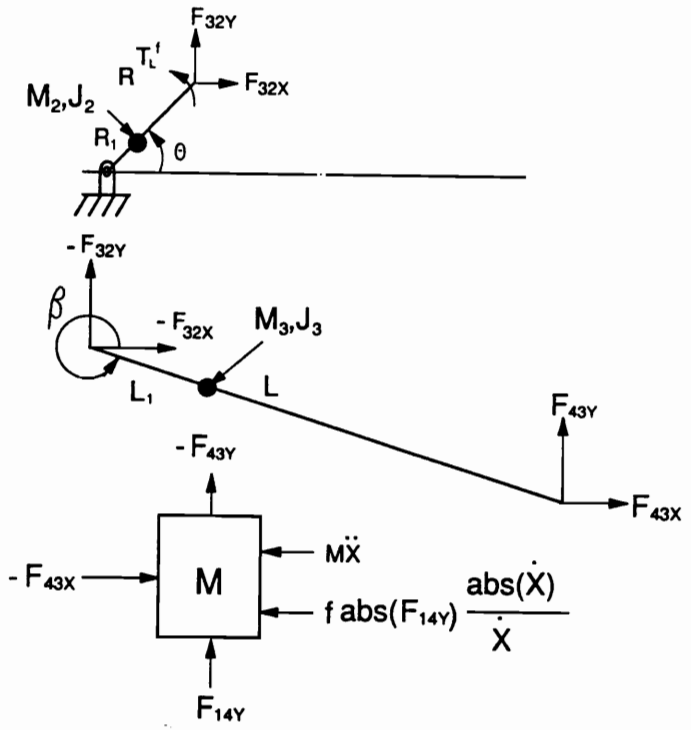

Figure 3-10. Free Body Diagram with Effect of Friction

if $F_{14Y} \geq 0$ and $\dot{X} < 0$

or $F_{14Y} < 0$ and $\dot{X} \geq 0$

$$
\begin{aligned}
T_{LM}^{f} = {} & J_2'\ddot{\theta} - E_2 g \sin\theta \\
& + MR(\ddot{X} + g)\left(\frac{\cos\theta \sin\beta - f\sin\theta \sin\beta}{L\cos\beta - fL\sin\beta} - \sin\theta\right) \\
& + M_3 R\left(A_{R3Y}\cos\theta - A_{R3X}\sin\theta - g\sin\theta + \frac{L_1 g\cos\theta \sin\beta - fL_1 g\sin\theta \sin\beta}{L\cos\beta - fL\sin\beta}\right) \\
& - J_3' R\ddot{\beta}\,\frac{\cos\theta - f\sin\theta}{L\cos\beta - fL\sin\beta}
\end{aligned}
$$

The sign of $\dot{X}$ can be determined from Equation 3-11.

$$\dot{X} = -R\dot{\theta}\sin\theta - L\dot{\beta}\sin\beta \qquad (3-11)$$

The sign of the piston side thrust force, F_{14Y}, can be determined by solving the equilibrium equation by setting the kinetic friction coefficient zero since the effect of the kinetic friction on the piston side thrust force is just on magnitude but not on direction.

$$F_{14Y}^{M} = \frac{J_3'\ddot{\beta} - L_1 M_3 g\sin\beta - L\sin\beta M\ddot{X} - L\sin\beta Mg}{L\cos\beta} \qquad (3-60-1)$$

which F_{14Y}^{M} represents the side thrust force caused by inertia of the slider-crank mechanism without the effect of kinetic friction between the piston and the cylinder wall.

The load torque contributed by the pressure difference across the piston with the effect of kinetic friction between the piston and the cylinder wall, T_{LF}, can be derived with same procedure as above:

$$\text{if } F_{14Y} \geq 0 \text{ and } \dot{X} \geq 0$$
$$\text{or } F_{14Y} < 0 \text{ and } \dot{X} < 0 \qquad (3-61)$$

$$T_{LP}{}^{f} = AR\Delta P\left(\frac{\cos\theta\tan\beta + f\sin\theta\tan\beta}{1 + f\tan\beta} - \sin\theta\right)$$

$$\text{if } F_{14Y} \geq 0 \text{ and } \dot{X} < 0$$
$$\text{or } F_{14Y} < 0 \text{ and } \dot{X} \geq 0$$

$$T_{LP}{}^{f} = AR\Delta P\left(\frac{\cos\theta\tan\beta - f\sin\theta\tan\beta}{1 - f\tan\beta} - \sin\theta\right)$$

The sign of $\dot{X}$ is determined from Equation 3-11 and the sign of F_{14Y} is determined by:

$$F_{14Y}{}^{P} = -A\Delta P\tan\beta \qquad (3-60-2)$$

which $F_{14Y}{}^{P}$ represents the side thrust force caused by pressure difference across the piston without the effect of kinetic friction between the piston and the cylinder wall.

Comparing Equations 3-59 and 3-61 with Equations 3-28 and 3-41, it is noticeable that Equation 3-28 and 3-41 are the special cases of Equations 3-59 and 3-61 with knietic friction coefficient zero.

3.2.3.1 Significance of Kinetic Friction on the Load Torque

From Equation 3-28 and 3-59, it is noticed that the kinetic friction will not affect the quantities of the load torques contributed by the mass inertia of the crank with respect to the crankshaft, J_2, and the eccentricity of the crank with respect to the crankshaft,

E_2. To verify the significance of the kinetic friction effect on load torques of inertias of the reciprocating mass and connecting rod, two quantities, T_{LM1} and $T_{LM1}{}^f$, are defined as:

$$T_{LM1} = MR(\ddot{X}+g)(\tan\beta\cos\theta - \sin\theta)$$
$$+ M_3R(A_{R3Y}\cos\theta - A_{R3X}\sin\theta - g\sin\theta + \frac{L_1}{L}g\tan\beta\cos\theta) \quad (3-62)$$
$$- J_3{}'\frac{R\ddot{\beta}\cos\theta}{L\cos\beta}$$

$$\text{if } F_{14Y} \geq 0 \text{ and } \dot{X} \geq 0$$
$$\text{or } F_{14Y} < 0 \text{ and } \dot{X} < 0 \quad (3-63)$$

$$T_{LM1}{}^f = MR(\ddot{X}+g)(\frac{\cos\theta\sin\beta + f\sin\theta\sin\beta}{L\cos\beta + fL\sin\beta} - \sin\theta)$$
$$+ M_3R(A_{R3Y}\cos\theta - A_{R3X}\sin\theta - g\sin\theta + \frac{L_1g\cos\theta\sin\beta + fL_1g\sin\theta\sin\beta}{L\cos\beta + fL\sin\beta})$$
$$- J_3{}'R\ddot{\beta}\frac{\cos\theta + f\sin\theta}{L\cos\beta + fL\sin\beta}$$

$$\text{if } F_{14Y} \geq 0 \text{ and } \dot{X} < 0$$
$$\text{or } F_{14Y} < 0 \text{ and } \dot{X} \geq 0$$

$$T_{LM1}{}^f = MR(\ddot{X}+g)(\frac{\cos\theta\sin\beta - f\sin\theta\sin\beta}{L\cos\beta - fL\sin\beta} - \sin\theta)$$
$$+ M_3R(A_{R3Y}\cos\theta - A_{R3X}\sin\theta - g\sin\theta + \frac{L_1g\cos\theta\sin\beta - fL_1g\sin\theta\sin\beta}{L\cos\beta - fL\sin\beta})$$
$$- J_3{}'R\ddot{\beta}\frac{\cos\theta - f\sin\theta}{L\cos\beta - fL\sin\beta}$$

Table 3-2. Specification of Slider-Crank Mechanism

Crank Radius, R	1.0 in
Connecting Rod Length, L	4.0 in
Position of C.G. of Connecting Rod, L_1	1.25 in
Connecting Rod Mass, M_3	0.228 lbm
Mass Moment of Inertia of Connecting Rod, J_3'	0.394 lbm-in^2
Reciprocating Mass, M	0.448 lbm
Piston Area, A	4.382in^2

The slider-crank mechanism with kinematic construction specification shown as Table 3-2 was utilized to verify the significance of the kinetic friction on the load torque of inertia of connecting rod and reciprocating mass. The angular velocity and angular acceleration histories of the crankshaft through one complete cycle shown as Figure 3-5 and 3-6 (the data were acquired with the single-stage air compressor with cylinder head off, driven by a 1/2 horsepower three-phase induction motor).

According to Bowden and Tabor[13], the kinetic friction coefficient between lubricated steel surfaces is approximately 0.07 or less. To simulate the good and ill lubricating conditions, the kinetic friction coefficient is set to be 0.05 and 0.1 respectively.

Figure 3-11 and 3-12 show the contribution of the kinetic friction on the load torque caused by the inertias of connecting rod and reciprocating mass in time and frequency domains. The results indicate that even at ill lubricating condition, the kinetic friction makes negligible difference in load torque of inertias of connecting rod and reciprocating mass (less than 5% for the first five harmonic components).

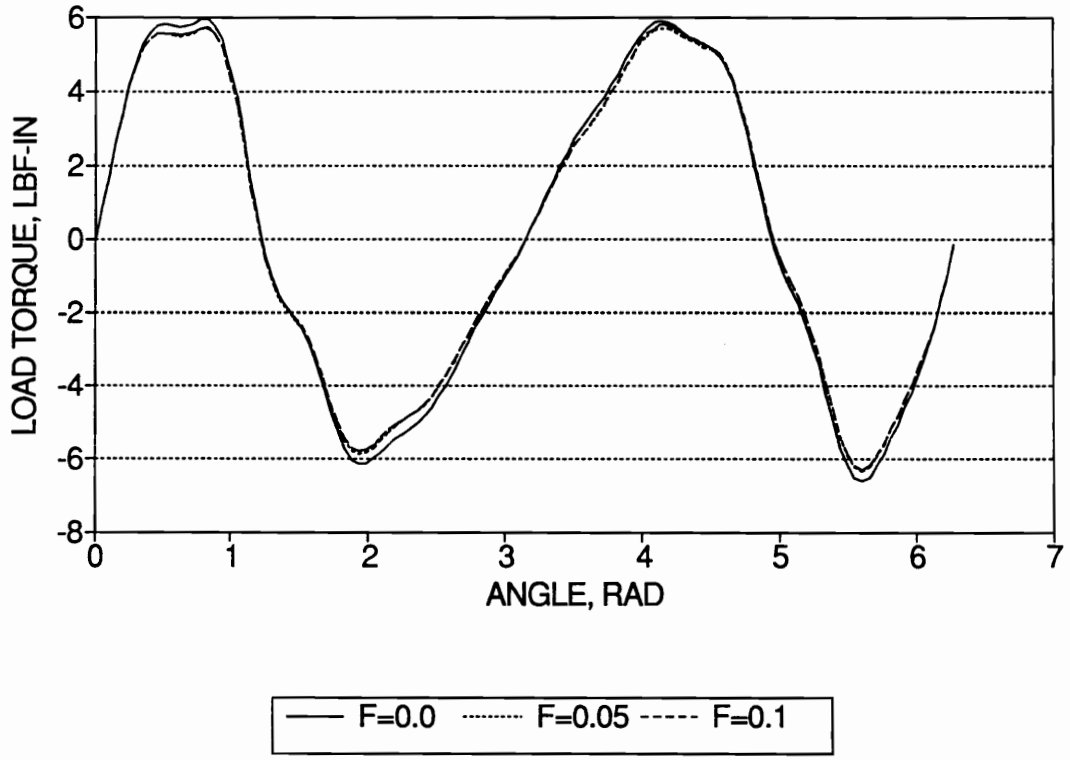

Figure 3-11. Load Torque Caused by Inertias of Connecting Rod and Piston in Time Domain

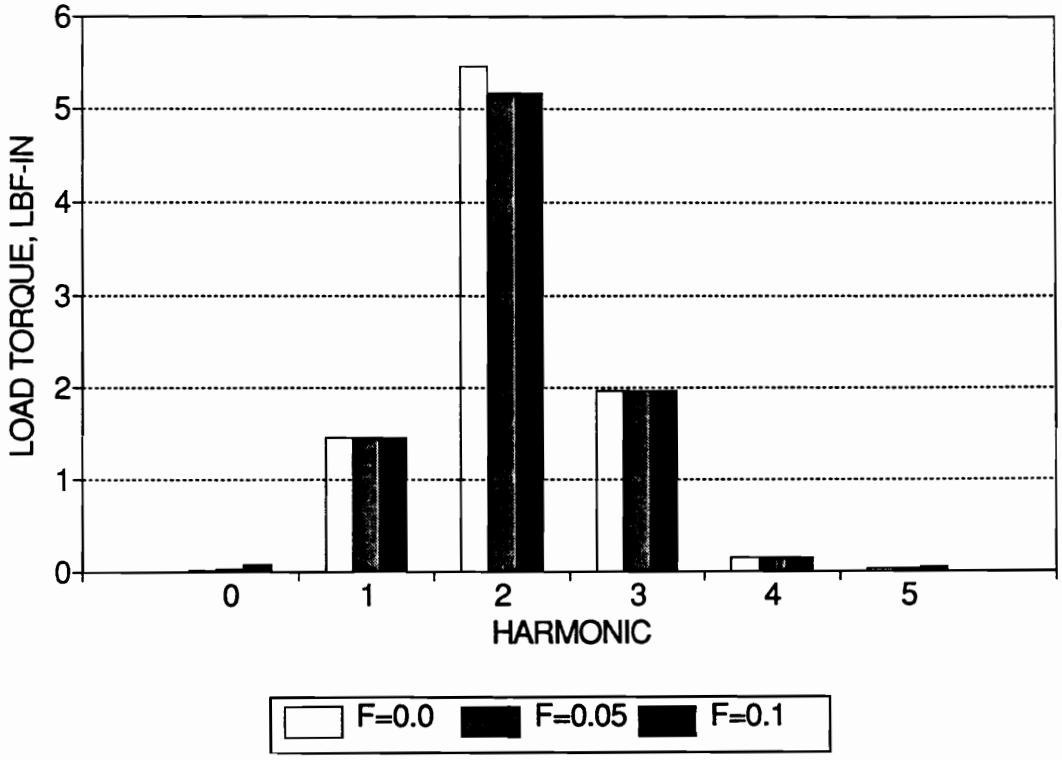

Figure 3-12. Load Torque Caused by Inertias of Connecting Rod and Piston in Frequency Domain

With the cylinder head installed, the single-stage air compressor with the slider-crank mechanism described above was also utilized to verify the significance of the kinetic friction on the load torque of the pressure difference across the piston. The pressure history through one complete cycle is shown as Figure 3-13 and Figure 3-14 and 3-15 show the contribution of the kinetic friction on the load torque caused by the pressure difference across the piston. As the case of the inertia load torque, the contribution of kinetic friction on pressure load torque is negligible.

From the results shown above, the friction effect between piston and wall can be treated as a single effect which is independent from the piston side thrust force and the friction force can be treated as a constant which is caused by the expanding force of piston rings.

3.3 Solution Techniques

In this research, the quantification of the compressor parameters is classified into two categories:

1. System parameters: the mass moment of inertia of the shaft system, J_S, the reciprocating mass of the piston, M, the mass and mass moment of inertia of the connecting rod, M_3 and J_3', the mass moment of inertia and the eccentricity of the crank, J_2 and E_2, and the friction force caused by the piston ring against cylinder wall, F. For these parameters, the linearity applies, that is:

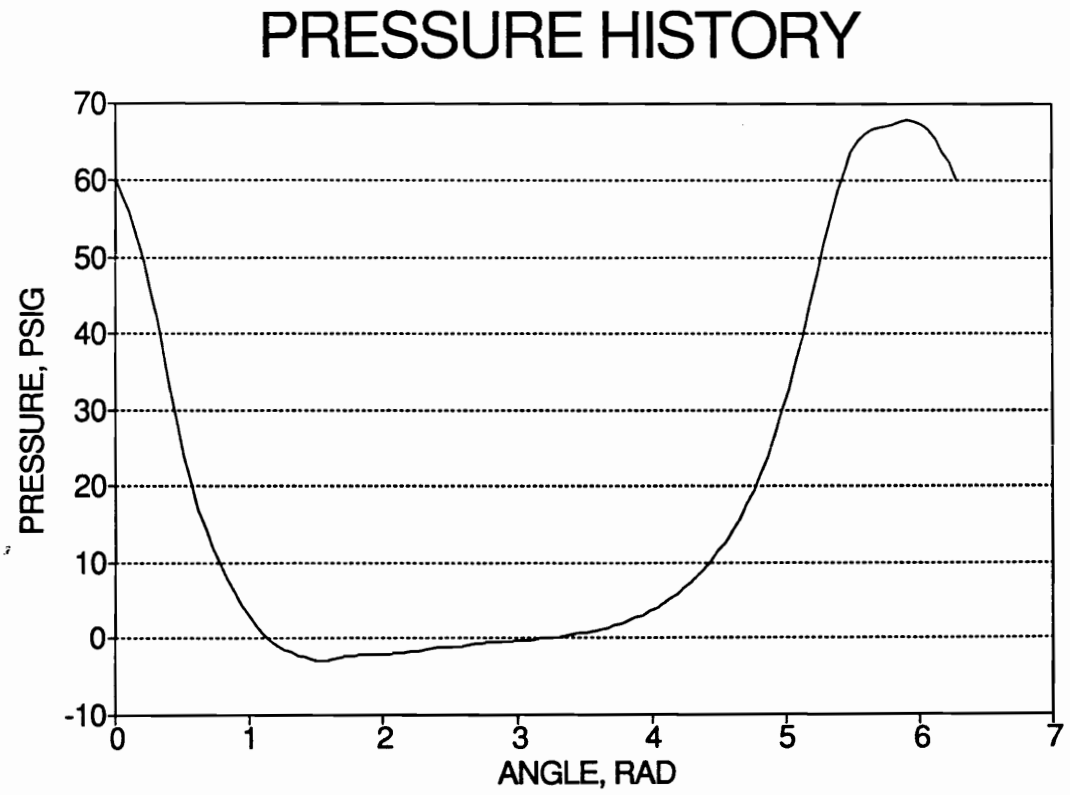

Figure 3-13. Pressure History Through One Complete Cycle of Crankshaft

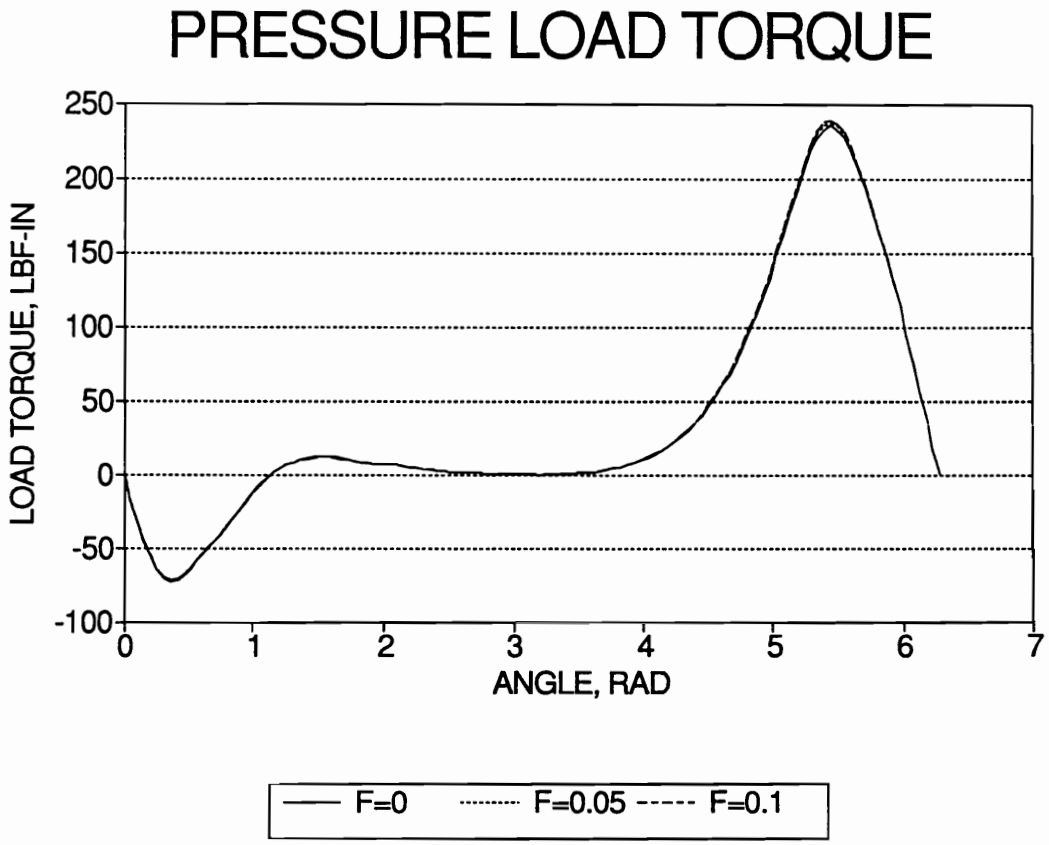

Figure 3-14. Load Torque Caused by Pressure in Time Domain

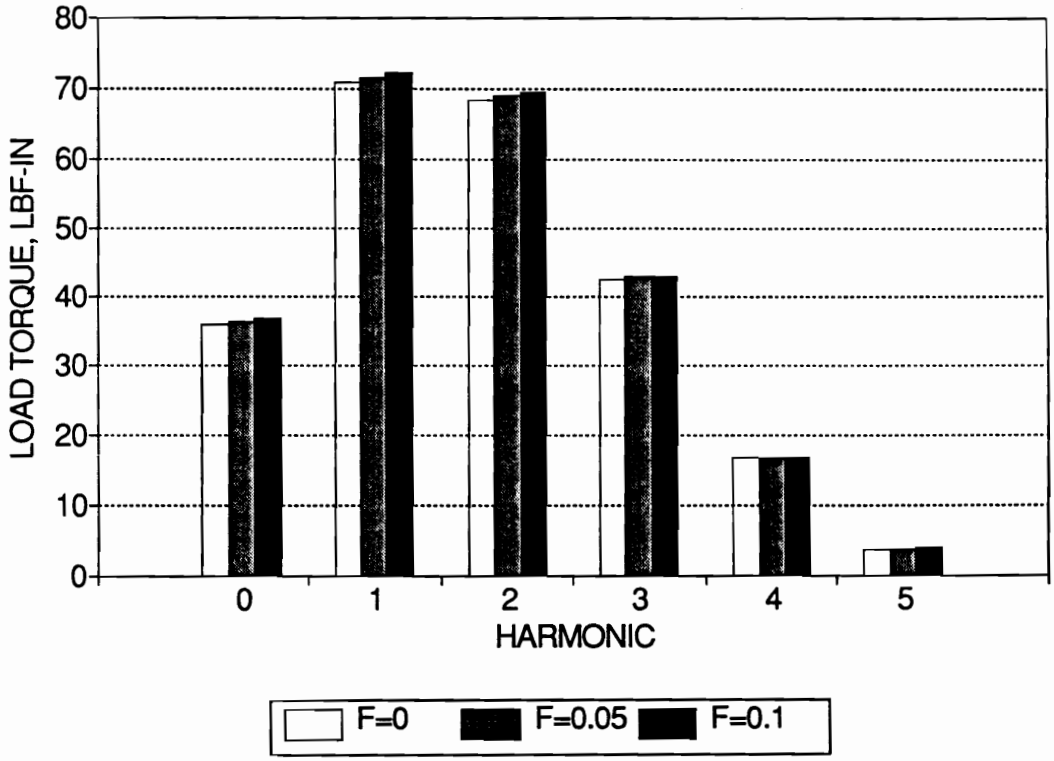

Figure 3-15. Load Torque Caused by Pressure in Frequency Domain

$$T_{LM} + T_{LE_2} + T_{LJ_2'} + T_{LM_3} + T_{LJ_3'} + T_{LF} + T_{LJ_S} =$$
$$MT_{LM}' + E_2T_{LE_2}' + J_2'T_{LJ_2'}' + M_3T_{LM_3}' + J_3'T_{LJ_3'}' \qquad (3-64)$$
$$+FT_{LF}' + J_ST_{LJ_S}'$$

where, T_{LM}, T_{LE_2}, $T_{LJ_2'}$ T_{LM_3}, $T_{LJ_3'}$ T_{LF}, and T_{LJ_S} represent the load torques contributed by reciprocating mass, eccentricity of the crank with respect to crankshaft, mass moment of inertia of the crank with respect to crankshaft, mass of the connecting rod, mass moment of inertia of the connecting rod with respect to the crank-pin bearing, friction force caused by the piston ring against cylinder wall, and mass moment of the shaft system; and T_{LM}', T_{LE_2}', $T_{LJ_2'}'$ T_{LM_3}', $T_{J_3'}'$ T_{LF}', and T_{LJ_S}' represent the load torques contributed by unit reciprocating mass, unit eccentricity of the crank with respect to crank shaft, unit mass moment of inertia of the crank with respect to crankshaft, unit mass of the connecting rod, unit mass moment of inertia of the connecting rod with respect to the crank-pin bearing, unit friction force caused by the piston ring against cylinder wall, and unit mass moment of the shaft system.

Equation (3-64) can be expressed in frequency domain,

$$f(T_{LM} + T_{LE_2} + T_{LJ_2'} + T_{LM_3} + T_{LJ_3'} + T_{LF} + T_{LJ_S}) =$$
$$Mf(T_{LM}') + E_2f(T_{LE_2}') + J_2'f(T_{LJ_2'}') + M_3f(T_{LM_3}') + J_3'f(T_{LJ_3'}') \qquad (3-65)$$
$$+Ff(T_{LF}') + J_Sf(T_{LJ_S}')$$

where, $f(\ldots)$ represents the Fourier transformation operation. Linearity still holds.

To quantify the system parameters, the experiment is designed to acquire the load torque without contribution of the back pressure on the piston, that is, with the

cylinder head off. Then, in order to estimate the system parameters, the measured torque is to be equated to the calculated torque.

$$f(T_{L\exp}) = Mf(T_{LM}') + E_2 f(T_{LE_2}') + J_2' f(T_{LJ_2}') + M_3 f(T_{LM_3}') + J_3' f(T_{LJ_3}') + Ff(T_{LF}') + J_S f(T_{LJ_S}') \quad (3-66)$$

where, $T_{L\exp}$ is the measured torque data.

Since, for a defined function, there exist unique Fourier components, by equating different components, a linear equation set can be constructed and the system parameters can be solved.

2. Pressure-Volume characteristic parameters: expansion constants, κ, intake and discharge pressure levels, P_{out}, and characteristic coefficients of intake and discharge pressure fluctuations, a_N and b_N. Unlike system parameters, the load torque contributed by pressure-volume characteristic parameters can not be linearly decoupled. In this case, the equation set constructed in frequency domain will be a nonlinear equation system. As discussed by Johnson and Riess[10], to solve a nonlinear equation system, the partial derivatives are needed to converge the solution efficiently, either with a closed form or by using finite-difference approximation. However, because the assumed pressure is a piecewise continuous function which makes the derivatives discontinuous, this solution algorithm will be less reliable because the discontinuity may diverge the solution.

Therefore, an optimization algorithm to deal with this piecewise continuous function by using statistical methods instead of using traditional gradient methods is intro-

duced to solve the pressure-volume characteristic parameters, time-domain solution technique. This algorithm is based on minimizing the difference between the experimental torque data and calculated torque data at n uniformly spaced points within one revolution of the crankshaft. The objective function is expressed as the summation of the absolute differences between calculated and experimental torques through one complete cycle.

After the system parameters have been estimated, the experiment is designed to acquire the load torque with contribution of the back pressure on the piston, that is, with the cylinder head on. Then, by subtracting the load torques contributed by the system parameters, the load torque contributed by the back pressure on the piston can be calculated.

$$T_{LPexp} = T_{Lexp} - T_{Lsys} \tag{3-67}$$

where,

T_{Lexp} Measured torque data.

T_{LPexp} Measured pressure torque data.

T_{Lsys} Torque contributed by the system parameters.

Then, the objective function can be constructed as:

$$f(X) = \sum_{i=1}^{n} (T_{LPcal}(X) - T_{LPexp})^2 \tag{3-68}$$

where,

X	Pressure-volume parameter vector of length N.
$f(X)$	The objective function of the N Pressure-Volume parameters.
$T_{LPcal}(X)$	Calculated torque.
T_{LPexp}	Measured torque.
n	The number of torque data under consideration through one complete cycle.

Mathematically, this solution can be expressed as:

$$\min f(X) \qquad (3-69)$$

$$\text{subject to } l_i \leq x_i \leq u_i, \text{ for } i = 1, 2, \ldots, n$$

Where l_i and u_i are the pre-defined lower and upper bounds.

3.3.1 Solution Algorithm for System Parameters

The linear equation system constructed from Equation 3-66 will be of the form:

$$AX = B \qquad (3-70)$$

where,

A	$(m \times n)$ coefficient matrix.
X	$(n \times 1)$ unknown vector.
B	$(m \times 1)$ known constant vector.

Equation 3-70 represents a linear equation system with n unknowns and m equations. To insure a nontrivial unique solution to Equation (3-70), the rank of matrix A, r, must be equal to the number of unknowns, n and the known constant vector, B, must be not a zero vector; that is, the number of independent equations must be equal to the number of unknowns and the equation system is not homogeneous.

However, the goal of the algorithm is curve-fitting of the output torque with the system parameters; that is, the algorithm is designed to find a 'best solution' instead of an 'exact solution'. Therefore, the number of equations, m, (assuming that all the equations are independent to each other) can be designed to be larger than the number of unknowns, n. Then, this problem becomes precisely the statistical problem of finding the best 'least-square solution' of $AX = B$. Mathematically, it can be expressed as the minimization of the Euclidean norm of vector AX and vector B.

$$\min \| |AX - B| \| \qquad (3-71)$$

Mathematically, it can be proven that there exists a vector X'(the best least-square solution of $AX = B$) such that

$$A^T A X^* = A^T B \qquad (3-72)$$

where, A^T is the transposition of matrix A. Then $||AX^* - B|| \leq ||AX - B||$ for all X.

Equation (3-72) is an (nxn) linear equation system known as 'normal equation system' with an 'exact' solution. According to Lawson and Hanson[11], by using QR decomposition, this normal equation system can be solved without forming $A^T A$. The QR decomposition of matrix A consists of finding an orthogonal matrix Q ($Q^{-1} = Q^T$) and an upper trapezoidal matrix with diagonal elements of nonincreasing magnitude, R, such that

$$A = Q^T R \qquad (3-73)$$

where,

A the ($m \times n$) coefficient matrix in Equation (3-70).

Q an ($m \times m$) orthogonal matrix.

R an ($m \times n$) trapezoidal matrix of the form:

$$R = \begin{bmatrix} R_{11} \\ 0 \end{bmatrix} \qquad (3-74)$$

R_{11} an ($n \times n$) upper triangular matrix.

Define the vector g of length m as:

$$g = QB = \begin{bmatrix} g_1 \\ g_2 \end{bmatrix} \qquad (3-75)$$

where,

B the $(m \times 1)$ constant vector in Equation (3-70).

g_1 an $(n \times 1)$ vector.

g_2 an $((m-n) \times 1)$ vector.

Then, the unique solution of Equation (3-72) can be expressed as:

$$R_{11}X^* = g_1 \qquad (3-76)$$

Since R_{11} is an $(n \times n)$ upper triangular matrix, X^* can be solved backward from X^*_n to X^*_1 and X^* gives rise to the residual vector, r, satisfying

$$r = B - AX^* = Q^T \begin{bmatrix} 0 \\ g_2 \end{bmatrix} \qquad (3-77)$$

3.3.1.1 Q-R Decomposition

Given a non-zero m-vector v, it can be proven there exists an orthogonal matrix Q such that

$$Qv = -\sigma \| v \| e_1 \qquad (3-78)$$

with

$$e_1 = \begin{bmatrix} 1 \\ 0 \\ . \\ . \\ 0 \end{bmatrix} \qquad (3-79)$$

and

$$\sigma = \begin{matrix} +1 \ if\ , v_1 \geq 0 \\ -1 \ if\ , v_1 < 0 \end{matrix} \qquad (3-80)$$

where v_1 is the first component of v.

Define

$$u = v + \sigma \| v \| e_1 \qquad (3-81)$$

and

$$Q = I_m \frac{2uu^T}{u^T u} \qquad (3-82)$$

where, I_m is an nxn unit matrix. By verifying directly it can be shown that matrix Q of in Equation (3-82) is symmetric and orthogonal and Equation (3-78) is satisfied.

This transformation defined in Equation (3-71) and (3-72) was used by A.S. Householder[12] in discussing a certain eigenvalue problem. For this reason, the matrix Q is called a Householder transformation matrix.

Let an $m \times m$ orthogonal matrix Q_1 be chosen as in Equation (3-82) such that the first column of Q_1A is zeroed in components 2 through m, where A is the mxn coefficient matrix in Equation (3-70). Next, choose an $(m-1) \times (m-1)$ orthogonal matrix P_2, which when applied to the (m-1) vector consisting of components 2 through m of the the second column of Q_1A results in zeros in components 3 through m. Then the transformation matrix

$$Q_2 = \begin{bmatrix} 1 & 0 \\ 0 & P_2 \end{bmatrix} \qquad (3-83)$$

is orthogonal and Q_1Q_2A has zeros below the diagonal in both the first two columns.

Continuing in this way, a product of n orthogonal transformations can be constructed that will transform A to upper triangular form.

In this research, the IMSL subroutine, LSQRR[9] , which adopts QR decomposition, is used to solve the normal equation system (3-72).

3.3.2 Solution Algorithm for Pressure-Volume Parameters

Almost all of the methods for handling constrained minimization make use of the first and sometimes the second partial derivatives of the objective function. The motivation behind the development of such methods is easily understood. The first and second derivatives of a function define its gradient and curvature and thereby determine the existence and location of the minimum which solves the problem being studied. Hence methods using this information are likely to lead to the solution most efficiently.

However, in Equation (3-69), two characteristics are noticed:

$$\min f(\mathrm{X}) \tag{3-69}$$

$$\text{subject to } l_i \leq x_i \leq u_i, \text{ for } i = 1, 2, \ldots, \mathrm{n}$$

1. The evaluation of the objective function, $f(\mathrm{X})$, involved a lengthy and complicated calculation.

2. Since the assumed pressure is a piecewise continuous function, the objective function, $f(\mathrm{X})$, is also a piecewise continuous function which makes the derivatives discontinuous.

As a consequence it is difficult or even impossible to derive explicit expressions for the required derivatives. In this circumstance, derivative values can only be obtained by means of finite difference approximations. However, this approach can introduce truncation and/or cancellation errors which nullify the theory underlying the algorithm and lead the search astray so that it converges to the solution very slowly, or possibly not at all.

As a result, the direct-search method which does not call for derivative values is introduced to solve Equation (3-69).

The direct-search strategies for generating a sequence of improving approximations to the solution are based simply on comparisons of the function values, and the method is more intuitive in nature by having a less rigorous mathematical basis. Furthermore, because of its lack of assumptions about the function, it can prove more reliable and stable than gradient methods.

However, it is important to appreciate that there are deficiencies in the direct-search approach. Whereas gradient methods are generally supported by optimality proofs, and the direct-search method discussed here is not, and consequently is aimed at producing a good solution rather than an optimal one, but in the hope that in practical terms 'good' will approximate 'optimal'. Associated with this difficulty is the problem of detecting convergence. For method with rigorous mathematical basis, sound convergence criteria can be derived, but this is not possible for intuitive direct-search methods. Consequently the direct-search methods base their termination criteria on the statistic characters of the test points. As discussed by Swan[5], because of the termination criteria, the direct searching algorithm are more liable to terminate prematurely or prolong the search unnecessarily.

3.3.2.1 The Algorithm for Function Minimization Based on Function Comparison

In 1962, Spendly, Hext and Himsworth[6] introduced an ingenious idea for tracking optimum operating conditions by evaluating the output from a system at a set of points forming a simplex in the factor-space, and continually forming new simplices by reflecting one point in the space of the remaining points. Then, by proposing that the simplex adapt itself to the local landscape, elongating down inclined planes, changing direction on encountering a valley at an angle, and contracting in the neighborhood of a minimum, and the criterion for stopping the process be chosen as a statistical character of the simplex, Nelder and Mead[7] modified the simplex method. As discussed by Murray and Wright[8], because of its programmability, this method became a popularly used algorithm to minimize non-smooth simple constrained functions.

The algorithm starts with a set of 2N points, $P_1, P_2, \ldots, P_{2N}$, in N-dimensional space called a *simplex*. f_i is defined as the function value at P_i, and

$$f_h = \max(f_i), \text{ h for highest}$$

$$f_l = \min(f_i), \text{ l for lowest}$$

Further, $\overline{P}$ is defined as the centroid of the points with $i \neq h$, and P_iP_j as the distance from P_i to P_j. At each iteration, a new point is generated to replace the worst point, P_h; three operations are involved - *reflection*, *contraction*, and *expansion*. These are defined as follows: the reflection of P_h is denoted as P^*, and its coordinates are defined by the relation

$$P^* = (1 + \alpha)\overline{P} - \alpha P_h \qquad (3-84)$$

where α is a positive constant, the *reflection coefficient*. Thus P^* is on the line joining P_h and $\overline{P}$, on the far side of $\overline{P}$ from P_h with $P^*\overline{P} = \alpha P_h\overline{P}$. If f^* lies between f_h and f_l, then P_h is replaced by P^* and another iteration stars with this new simplex.

If $f^* < f_l$, i.e. if reflection has produced a new minimum, then P^* is to be expanded to P^{**} by the relation

$$P^{**} = \gamma P^* + (1 - \gamma)\overline{P} \qquad (3-85)$$

The *expansion coefficient* γ, which is greater than unity, is the ratio of the distance $P^{**}\overline{P}$ to $P^*\overline{P}$. If $f^{**} < f_l$ then P_h is replaced by P^{**} and this process restart; but if $f^{**} > f_l$ then this expansion fails, and P_h is to be replaced by P^* before restarting.

If on reflecting P_h to P^*, $f^* > f_i$ for all $i \neq h$, i.e. that replacing P_h by P^* leaves f^* the maximum, then a new P_h is to be defined to be either the old P_h or P^*, whichever has the lower function value, and the new point is to be defined as

$$P^{**} = \beta P_h + (1 - \beta)\overline{P} \qquad (3 - 86)$$

The *contraction coefficient*, β, lies between 0 and 1 and is the ratio of the distance $P^{**}\overline{P}$ to $P_h\overline{P}$. Then P^{**} is to be accepted as P_h and another iteration starts unless $f^{**} > \min(f_h, f^*)$, i.e. the contracted point is worse than the better of P_h and P^*. For such a failed contraction the worst point P_h is to be replaced by $(P_h + P_l)/2$ and the process restart.

Whenever the new point generated is beyond the bound, it will be set to the bounds. This procedure is repeated until one of the following terminating criteria is satisfied.

Criteria 1:

$$f_{worst} - f_{best} \leq \varepsilon(1. + |f_{best}|) \qquad (3 - 87)$$

Criteria 2:

$$\sum_{i=1}^{2N} \left[f_i - \frac{\sum_{j=1}^{2N} f_j}{2N} \right]^2 \leq \varepsilon \qquad (3 - 88)$$

where ε is a given tolerance.

The coefficient α, β, and γ give the factor by which the volume of the simplex is changed by the operations of reflection, contraction or expansion respectively. Their values effect the convergence rate. The stopping criteria of the iteration are characteristics of the complex, i.e. the iteration continues until the points of the complex are compact enough. The complete method of this function minimization is shown as a flow diagram in Figure 3-16.

In this research, the IMSL subroutine, BCPOL[9] , which adopts the simplex method, is used to minimize the objective function, $f(X)$, in Equation 3-69.

3.4 References

1. Mabie, H. H., and Reinholtz C. F., 1987, *Mechanisms and Dynamics of Machinery, Fourth Edition,* John Wiley & Sons.

2. Herbert Goldstein, 1980, *Classical Mechanics, Second Edition,* Addison-Wesley Publishing Company, Inc.

3. Easttop, T.D. and McConkey, A., 1986, *Applied Thermodynamics for Engineering Technologists, SI Units, Fourth Edition,* Longman Inc., New York.

4. Pichot, Pierre, 1986, *Compressor Application Engineering, Volume 1, Compression Equipment,* Gulf Publishing Company, Houston, Texas.

5. Swan, W. H., 1974, *Constrained Optimization by Direct Search,* in *Numerical Methods for Constrained Optimization,* (P.E. Gill and W. Murray, eds), pp 191-217, Academic Press, London and New York.

6. Spendley, W., Hext, G. R. and Himsworth, F. R., 1962, *Sequential Application of Simplex Designs in Optimization and Evolutionary Operation,* Technometrics, Vol. 4, p441.

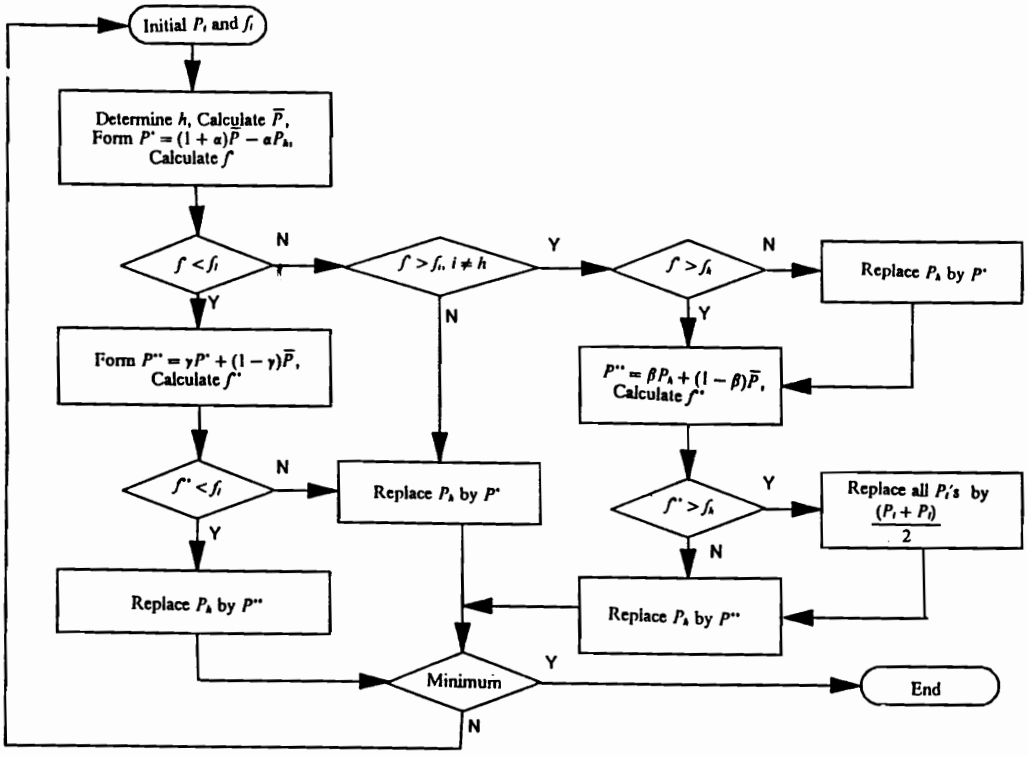

Figure 3-16. Flow diagram of function minimization by direct-search[6]

7. Nelder, J. A. and Mead, R., 1965, *A Simplex Method for Function Minimization,* Computer Journal 7, pp 308-313.

8. Gill, P. E., Murray, W., and Wright, M. H., 1981, *Practical Optimization,* Academic Press, New York.

9. ISML, Inc., 1987 *User's Manual, Volume 2*

10. Lee W. Johnson and R. Dean Riess, 1982, *Numerical Analysis, Second Edition,* Addison-Wesley Publishing Company.

11. C.L. Lawson and R.J. Hanson, 1974, *Solving Least Squares Problems,* Pretic-Hall, Inc., Englewood Cliffs, New Jersy.

12. A.S. Householder, 1958, *Unitary Triangularization of a Nonsymmetric Matrix,* Journal ACM, 5, pp 339-342.

13. F.P. Bowden, D. Tabor, 1950, *The Friction and Lubrication of Solids,* Oxford University Press, Amen House, London.

4.0 Mathematical Modeling for a Multi-Stage Compressor

In this chapter, the experimental data from DTRC (David Taylor Research Center) is used to verify the solution algorithm for the pressure-volume parameters of a multi-stage air compressor. The effects of the tolerance for the stopping criteria of the root-finding algorithm and pressure fluctuations during intake and discharge procedures on the precision of the parameters and the value of the objective function, i.e. the absolute difference between the calculated and experimental torque, are to be analyzed. Also, the uniqueness of solutions is discussed.

The data is for a 4-stage 4-cylinder 50 Hp Worthington high pressure air compressor. The specifications of each stage are shown as Table 4-1 and the pressure-angle relations shown as Figures 4-1, 4-2, 4-3, and 4-4. The pressure data was reported for 5° steps, from 0° to 360°, totally 72 data points. The load torques caused by the cylinder pressures are calculated using Equation 3-41.

Table 4-1. Specifications for the 4-stage Compressor

	Stage 1	Stage 2	Stage 3	Stage 4
Crank Radius, in	2.5	2.5	2.5	2.5
Connecting Rod Length, in	11.5	11.5	11.5	11.5
Piston Area, in^2	42.4	15.4	2.48	0.8
Cylinder Angle, Degree	0	180	0	180
Clearance Length, in	0.767	0.8275	2.585	2.9625

4.1 The Tolerance for the Stopping Criteria of the Algorithm

As described in the Equations (3-77) and (3-78) in the previous chapter, the tolerance, ε, is the criteria to halt the iterations of the algorithm. In order to guarantee the convergence of solution, the tolerance needs to be sufficiently small. On the other hand, if the tolerance is too small the number of iterations will be excessive, without improving the roots. The suggested strategy, developed experimentally, to deal with this dilemma is to start the tolerance with 0.1 and diminish it till the roots converge, or the minimum of the objective function converges.

Figure 4-5 portrays an example with the torque contributed by pressure of stage 1. According to the results, the solutions are reliable if the tolerance is smaller than 10^{-3}.

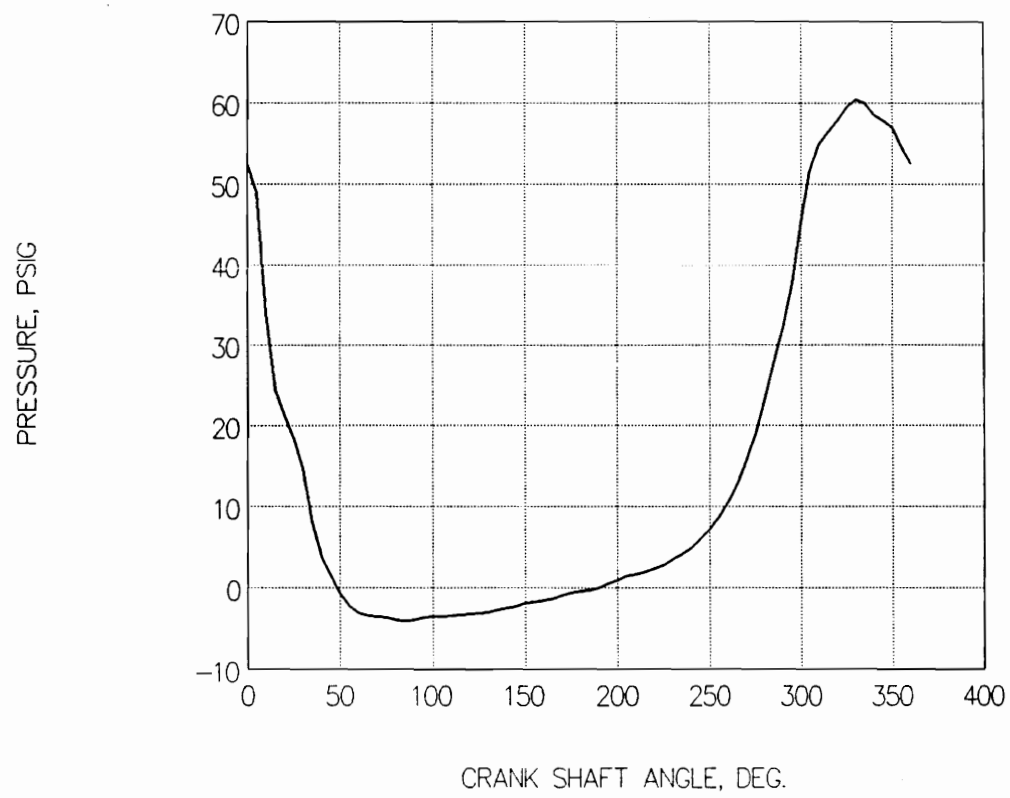

Figure 4-1. Pressure-Angle for Stage 1

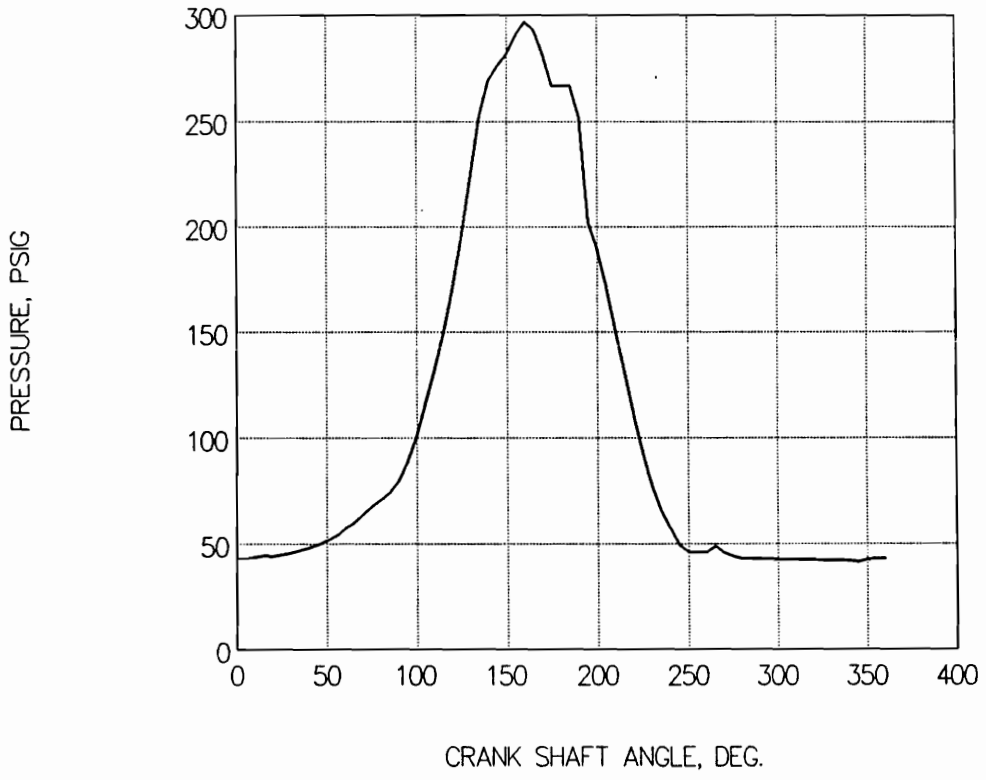

Figure 4-2. Pressure-Angle for Stage 2

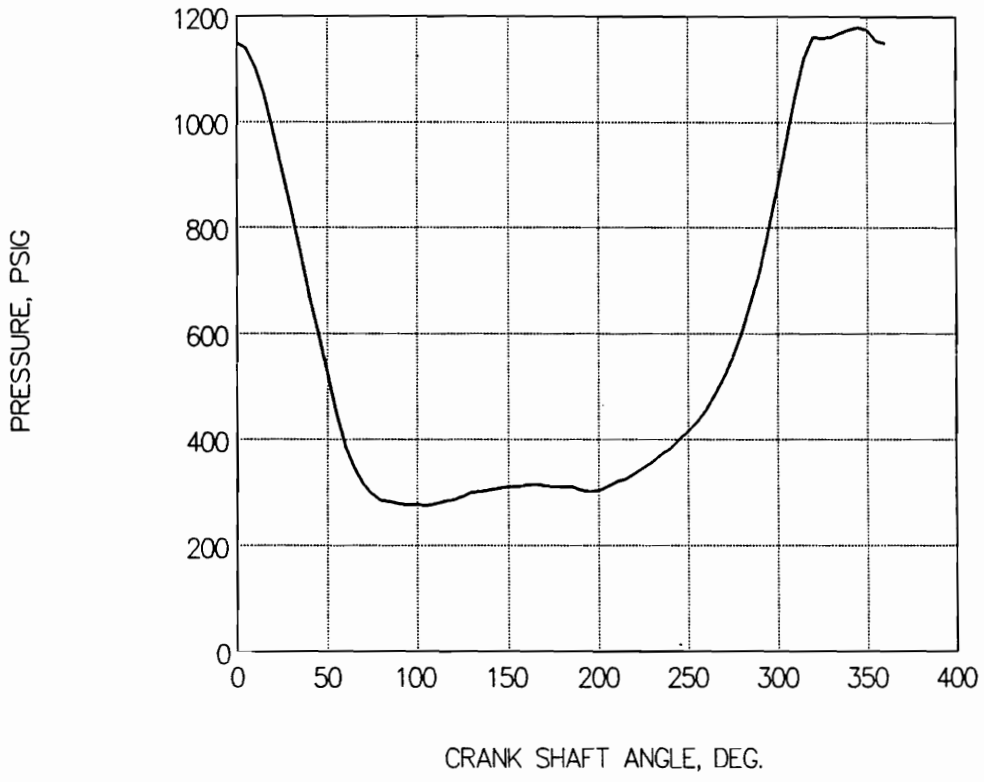

Figure 4-3. Pressure-Angle for Stage 3

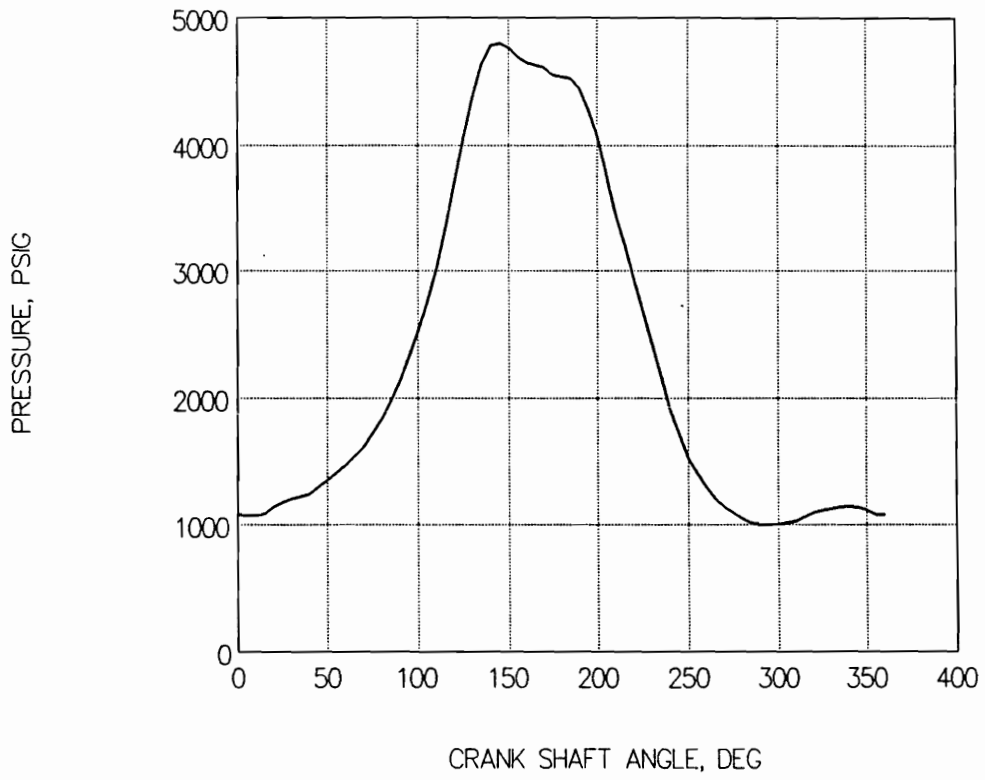

Figure 4-4. Pressure-Angle for Stage 4

	Bound	Initial	$\varepsilon = 10^{-1}$	$\varepsilon = 10^{-2}$	$\varepsilon = 10^{-3}$	$\varepsilon = 10^{-4}$	$\varepsilon = 10^{-5}$
P_{out}, *psia*	60. to 80.	70.	65.05663	64.75148	60.33119	60.25931	60.25095
a_1, psi	0. to 20.	0.	12.61148	12.29837	17.13841	17.20388	17.16145
a_2, psi	-20. to 20.	0.	-1.69878	-0.82131	-0.84387	-0.85693	-0.81753
P_{in}, *psia*	10. to 20.	15.	14.70906	14.63445	14.23203	14.23720	14.24365
b_1, psi	0. to 10.	0.	4.12938	3.95069	3.32067	3.25787	3.26475
b_2, psi	-10. to 10.	0.	0.71309	0.91828	1.03849	1.10987	1.11180
κ_1	1. to 3.	2.	1.99871	2.01168	1.81230	1.80080	1.80045
κ_2	1. to 3.	2.	1.45286	1.46674	1.51470	1.51314	1.51258
Function value			0.54501E6	0.51658E6	0.44494E6	0.44386E6	0.44379E6

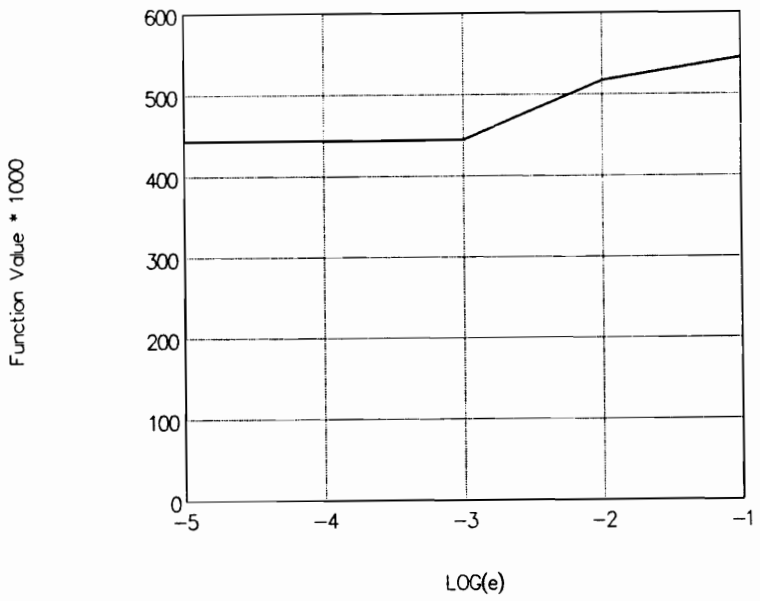

Figure 4-5. Effect of Tolerance to Solutions

4.2 *Characteristics of Intake and Discharge Pressure Fluctuations*

As discussed in Equation (3-46) and (3-47), a_1, a_2, ..., a_n, and b_1, b_2, ..., b_n are the harmonic amplitudes of the pressure fluctuations during discharge and intake. As the numbers of the terms in the equations increase, the precision of the discharge and intake pressures is enhanced. However, as more terms are involved in these two equations, more unknowns are to be solved for in the non-linear equation set, i.e. more iterations will be needed to converge to the minimum. The strategy in this solution algorithm is to start the iteration with no harmonic terms, then increase the the terms until the minimum of the objective function converges. Figure 4-6 represents the example with the torque contributed by pressure of stage 1 without the effects of damping and the reciprocating mass assumed known. The results show that employing more than 2 harmonic terms will not improve the solution.

4.3 *Uniqueness of Solution*

As mentioned in the previous chapter, the direct-search solution techniques are not supported by optimal proofs. The solutions vary significantly with unknown bounds. In this case, good engineering judgement and data analysis, sometimes even trial-and-error, is necessary to obtain 'reasonable' results. Table 4-2 represents the example how the

	Bound	Initial	0 term	1 term	2 terms	3 terms	4 terms
P_{out}, *psia*	60. to 80.	70.	72.75487	60.21405	60.25931	60.00006	60.00000
a_1, psi	0. to 20.	0.	**	16.77818	17.20388	18.33580	18.30926
a_2, psi	-20. to 20.	0.	**	**	-0.85693	-2.44955	-2.45230
a_3, psi	-20. to 20.	0.	**	**	**	2.46598	2.47885
a_4, psi	-20. to 20.	0.	**	**	**	**	0.00646
P_{in}, *psia*	10. to 20.	15.	12.92951	14.15082	14.23720	14.45069	14.45178
b_1, psi	0. to 10.	0.	**	3.65695	3.25787	3.73402	3.65938
b_2, psi	-10. to 10.	0.	**	**	1.10987	0.72820	0.91134
b_3, psi	-10. to 10.	0.	**	**	**	0.70599	0.47430
b_4, psi	-10. to 10.	0.	**	**	**	**	0.35684
κ_1	1. to 3.	2.	2.18299	1.80862	1.80080	1.78243	1.77870
κ_2	1. to 3.	2.	1.59215	1.51879	1.51314	1.48849	1.48883
Function value			0.22132E7	0.54242E6	0.44386E6	0.31859E6	0.31101E6

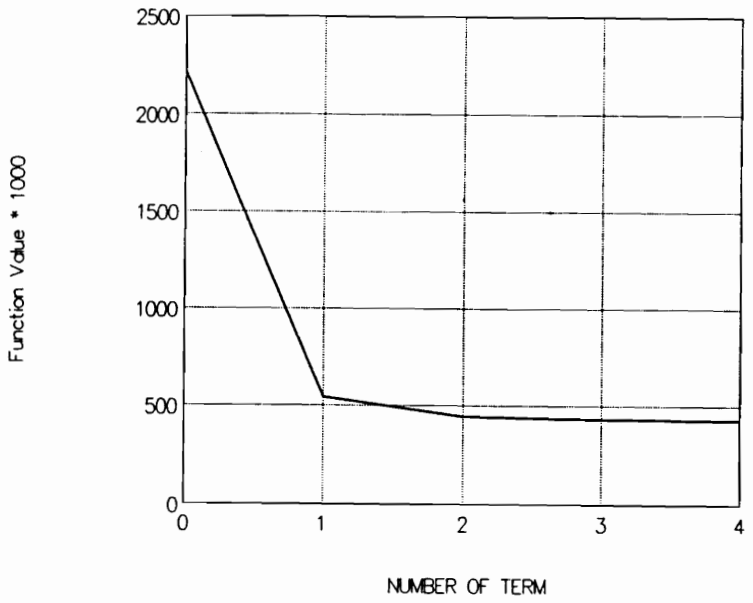

Figure 4-6. Effect of Pressure Fluctuation Terms

bounds of unknown vector affect the solution to the pressure-volume parameters of stage 1.

4.4 Solution to the Four-Stage Compressors

To solve the pressure-volume parameters of this 4-stage 4-cylinder compressor, the number of the harmonic terms of the pressure fluctuations during intake and discharge starts from 0; increasing until the value of objective function converges. The results are shown in Table 4-3 and the experimental and curve-fitted pressure-volume relations shown as Figures 4-7, 4-8, 4-9 and 4-10.

Figure 4-11 and 4-12 compare the load torque contributed by the measured cylinder pressures with curve fitted cylinder pressures in time and frequency domains. The results indicate that for the first five harmonics, the curve fitting is accurate within 5%.

Table 4-2. Effects of Unknown Bounds

	Initial	Bound	Solution	Bound	Solution	Bound	Solution
P_{out}	70.	60. to 80.	60.24202	55. to 85.	60.23841	50. to 90.	58.40305
a_1	0.	-20. to 20.	17.19243	-25. to 25.	17.14445	-30. to 30.	19.08550
a_2	0.	-20. to 20.	-0.80025	-25. to 25.	-0.78112	-30. to 30.	-0.78078
P_{in}	15.	10. to 20.	14.24117	5. to 25.	14.24165	0. to 30.	14.19605
b_1	0.	-10. to 10.	3.28352	-15. to 15.	3.26971	-20. to 20.	3.21311
b_2	0.	-10. to 10.	1.10750	-15. to 15.	1.10236	-20. to 20.	1.12046
κ_1	2.	1. to 3.	1.80005	1. to 3.5	1.79939	1. to 4.	1.73930
κ_2	2.	1. to 3.	1.51263	1. to 3.5	1.51246	1. to 4.	1.51881
Function value			0.44383E6		0.44381E6		0.43861E6

Table 4-3. Results of the 4-stage Compressor

	Initial	Bound	Solution
Stage 1			
P_{out}, psia	70.	50. to 80.	60.16091
a_1, psi	0.	-20. to 20.	13.00186
a_2, psi	0.	-20. to 20.	-1.77436
a_3, psi	0.	-20. to 20.	2.45775
P_{in}, psia	15.	10. to 20.	15.40961
b_1, psi	0.	-10. to 10.	2.67154
b_2, psi	0.	-10. to 10.	0.67821
b_3, psi	0.	-10. to 10.	0.05993
κ_1	2.	1. to 3.	1.67535
κ_2	2.	1. to 3.	1.45854
Stage 2			
P_{out}, psia	270.	240. to 320.	274.34742
a_1, psi	0.	-100. to 100.	43.43430
a_2, psi	0.	-100. to 100.	-8.16155
a_3, psi	0.	-100. to 100.	-2.86333
P_{in}, psia	60.	40. to 75.	53.82017
b_1, psi	0.	-50. to 50.	-0.09602
b_2, psi	0.	-50. to 50.	-2.88119
b_3, psi	0.	-50. to 50.	-5.74284
κ_1	2.	1. to 3.	1.38346
κ_2	2.	1. to 3.	1.34251
Stage 3			
P_{out}, psia	1100.	1000. to 1300.	1043.93445
a_1, psi	0.	-500. to 500.	135.18528
a_2, psi	0.	-500. to 500.	-8.57571
a_3, psi	0.	-500. to 500.	10.88448
P_{in}, psia	300.	200. to 400.	298.73060
b_1, psi	0.	-250. to 250.	10.54853
b_2, psi	0.	-250. to 250.	35.80524
b_3, psi	0.	-250. to 250.	-5.89672
κ_1	2.	1. to 3.	2.17580
κ_2	2.	1. to 3.	1.72775
Stage 4			
P_{out}, psia	4600.	4200. to 4900.	4577.87869
a_1, psi	0.	-500. to 500.	113.05125
a_2, psi	0.	-500. to 500.	10.75316
a_3, psi	0.	-500. to 500.	26.46469
P_{in}, psia	1000.	900. to 1250.	1033.05159
b_1, psi	0.	-250. to 250.	67.88923
b_2, psi	0.	-250. to 250.	12.95361
b_3, psi	0.	-250. to 250.	40.17928
κ_1	2.	1. to 3.	2.08261
κ_2	2.	1. to 3.	2.07182
Function value			0.27809E6

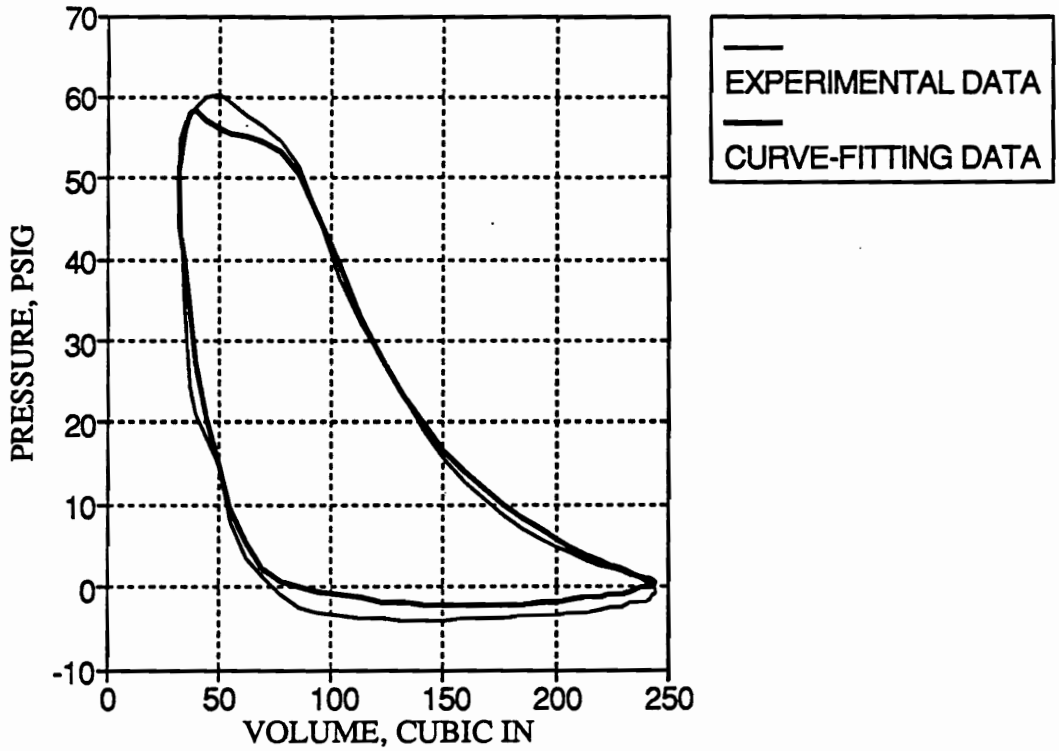

Figure 4-7. Pressure-Volume Diagram for Stage 1

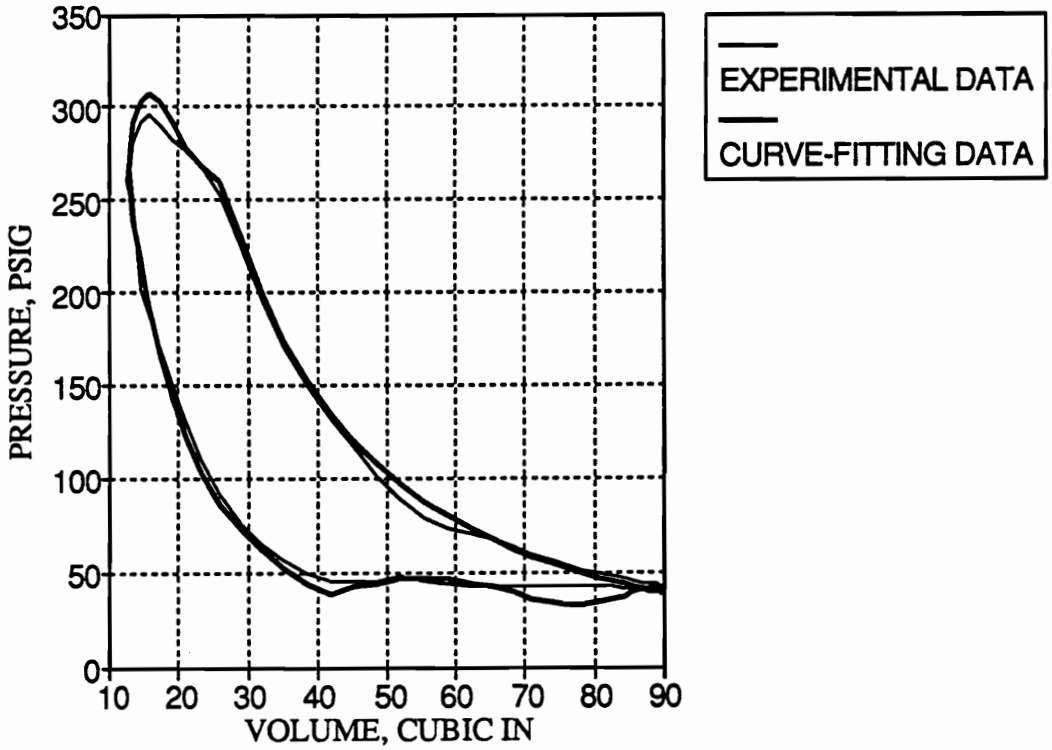

Figure 4-8. Pressure-Volume Diagram for Stage 2

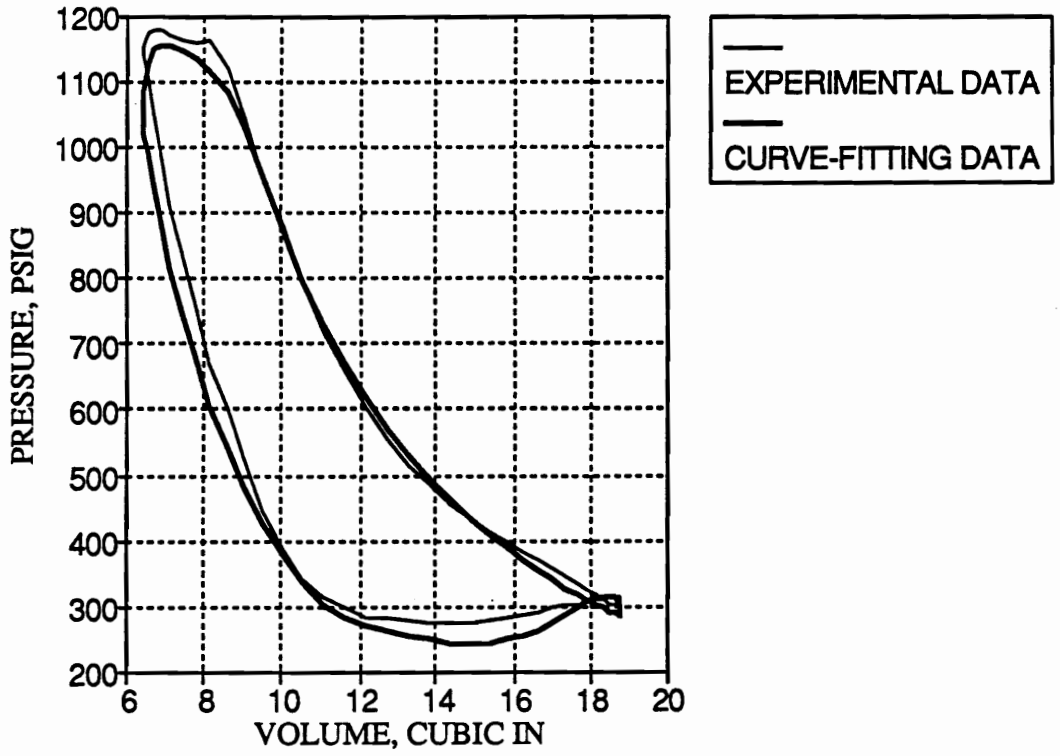

Figure 4-9. Pressure-Volume Diagram for Stage 3

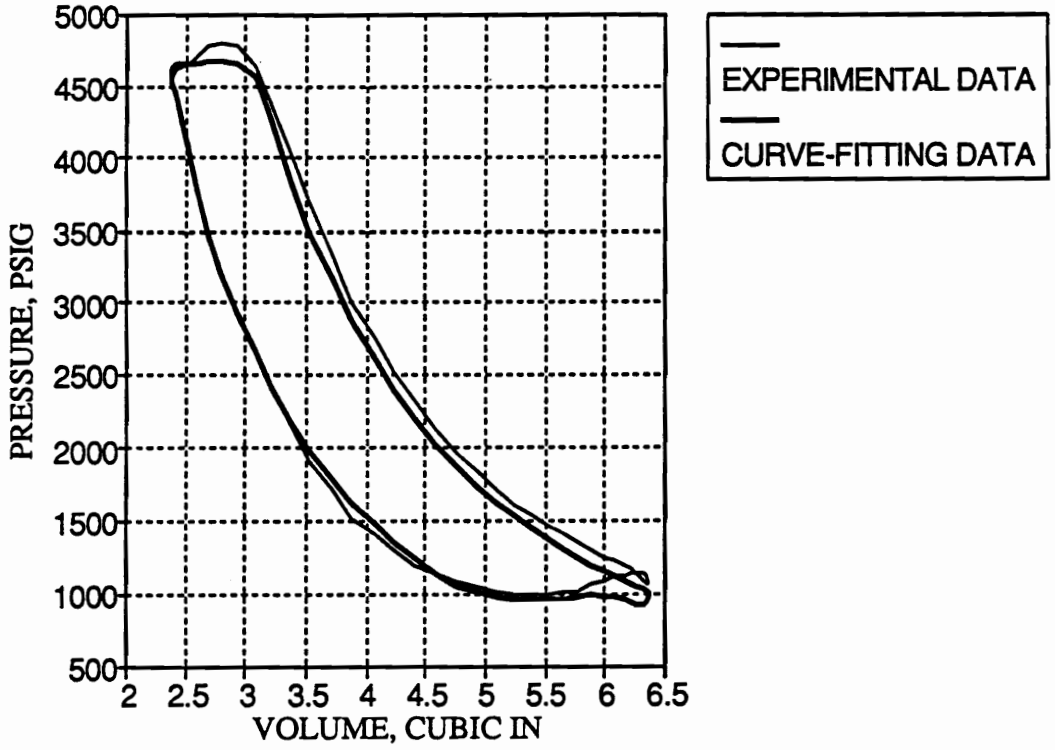

Figure 4-10. Pressure-Volume Diagram for Stage 4

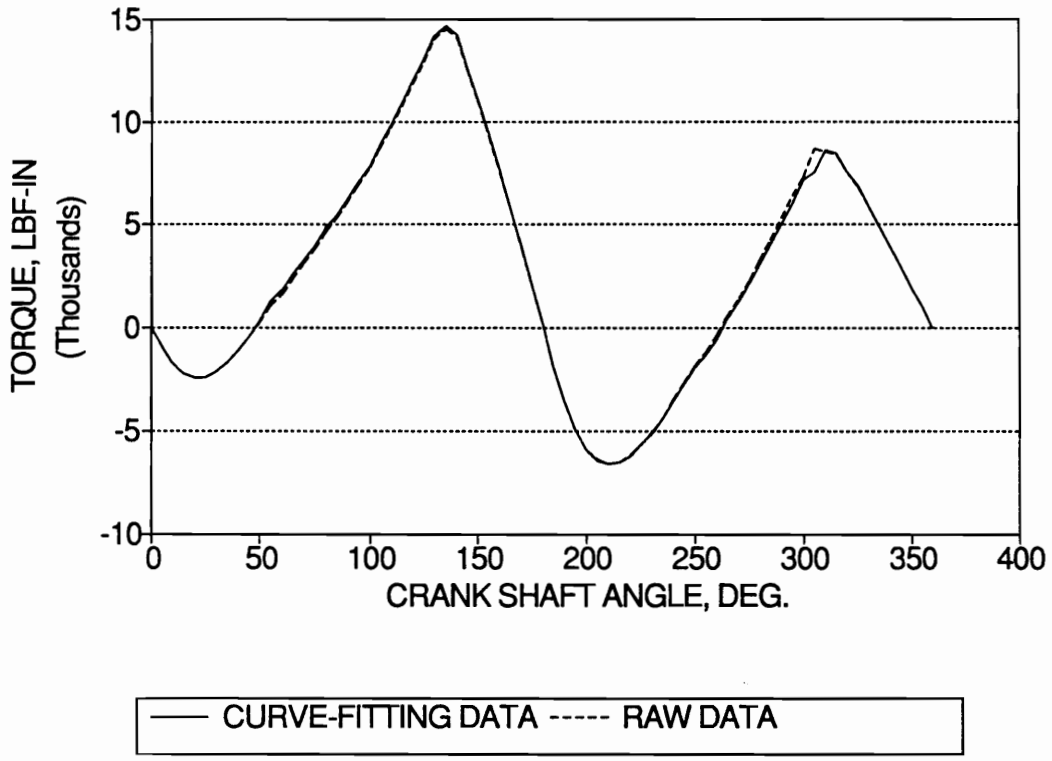

Figure 4-11. Pressure Load Torque in Time Domain

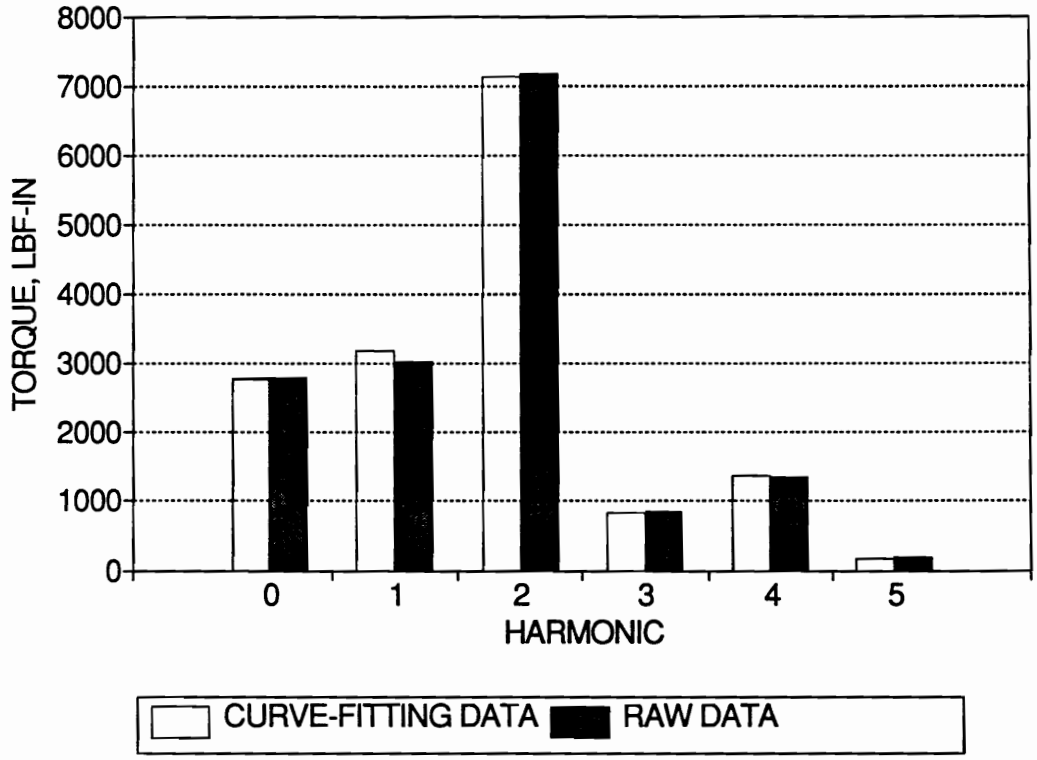

Figure 4-12. Pressure Load Torque in Frequency Domain

5.0 Results and Discussion

5.1 System Parameter Quantification by Direct Measurement of Load Torque

In order to quantify the system parameters, the mass moment of inertia of the crank with respect to the crankshaft, J_2', the reciprocating mass, M, the mass of the connecting rod, M_3, the mass moment of inertia of the connecting rod with respect to the crank-pin bearing, J_3', the eccentricity of the crank with respect to the crankshaft, E_2, and the friction force of the piston rings against the cylinder wall, F, by direct measurement of the load torque, the compressor-motor system is run with the cylinder head off (without the back pressure acting on the piston).

From the derivations in Chapters 3 and 5, the governing equation of torque equilibrium for the system can be written as

$$VD - T_{LP_C} = T_{LM} + T_{LE_2} + T_{LJ_2'} + T_{LM_3} + T_{LJ_3'} + T_{LF} + M_{EQ}\ddot{y}D \qquad (5-1)$$

In Equation (5-1), in addition to the five system parameters, the equivalent mass of the torque table lumped at the top of the load cell, M_{EQ}, are the unknown parameters to be determined.

In this solution algorithm, the known parameters are the kinematic construction of the slider-crank mechanism and the distance from the axis of the crankshaft to the load cell. These parameters are shown in Table 5-1.

The measurements required to quantify the unknown parameters are the force acting on the load cell, the vertical acceleration of the torque table, the angular velocity of the crankshaft, and the pressure of the crankcase. Figure 5-1, 5-2, 5-3, and 5-4 show these measurements through one complete cycle of crankshaft revolution. The period of one complete cycle of the crankshaft, T, is 0.0677 seconds.

Since the measurements are performed under the steady-state rotation of the system, the DC components (averages) of the vertical acceleration and crankcase pressure are assumed to be zero. Figures 5-1, 5-2, 5-3, and 5-4 represent the signal of the first ten harmonics (approximately up to 150 Hz). By differentiating the angular velocity with respect to time, the angular acceleration can calculated.

$$\dot{\theta}(t) = \sum_{N=0}^{10} \left(A_{\dot{\theta}N} \cos \frac{2\pi Nt}{T} + B_{\dot{\theta}N} \sin \frac{2\pi Nt}{T} \right)$$

$$\ddot{\theta}(t) = \sum_{N=1}^{10} \frac{2\pi N}{T} \left(- A_{\dot{\theta}N} \sin \frac{2\pi Nt}{T} + B_{\dot{\theta}N} \cos \frac{2\pi Nt}{T} \right) \qquad (5-2)$$

Figure 5-5 shows the angular acceleration of the crankshaft through one complete cycle.

Table 5-1. Kinematic Construction of Slider-Crank Mechanism

Crank Radius, R	1.0 in
Connecting Rod Length, L	4.0 in
Position of C.G. of Connecting Rod, L_1	1.25 in
Distance, D	10.0 in
Piston Area, A	4.382 in^2
Clearance Length, CL	0.1769 in

The angular position of the crankshaft is to be evaluated by

$$\theta(t) = \int_0^t \dot{\theta} dt \qquad (5-3)$$

Figure 5-1 indicates that the angular velocity is bounded within a range of ∓ 2 rad/sec which is approximately 2% of the average of the angular velocity, 93.5 rad/sec, and the first data point is located at top dead center of the slider-crank (the angular position is zero). Therefore, the angular position of Nth point can be calculated as

$$\theta_N = \frac{2\pi(N-1)}{120} \qquad (5-4)$$

since the data set consists 120 data points.

Using the kinematics of the slider-crank, the angular position, angular velocity and angular acceleration of the crankshaft, and the vertical acceleration of the lumped mass, the load torques contributed by unit quantities of the system parameters can be determined. As shown in Equation (5-1), the seven parameters to be quantified include the reciprocating mass, M, the eccentricity of the crank with respect to the crankshaft, E_2,

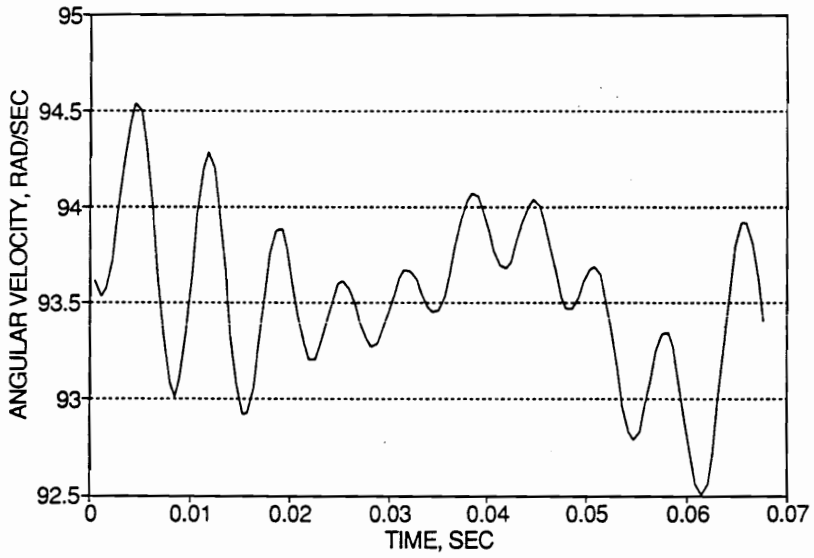

Figure 5-1. Angular Velocity of Crankshaft

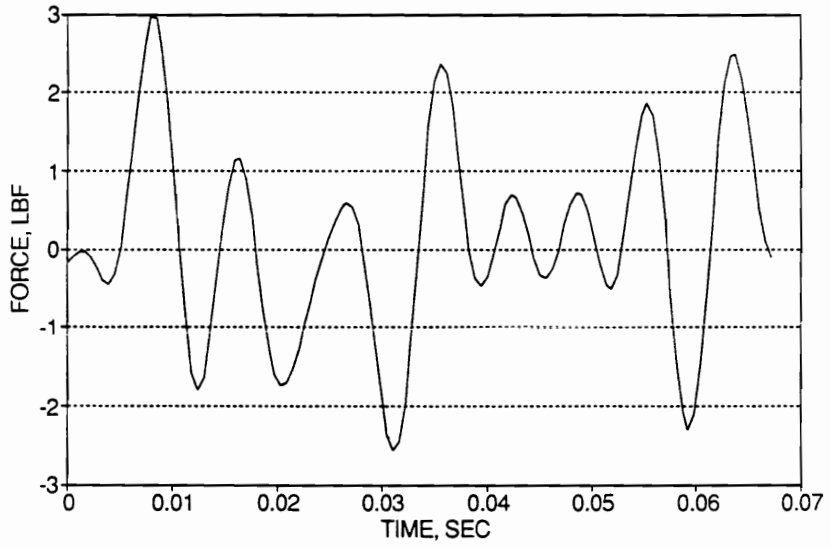

Figure 5-2. Force on Load Cell

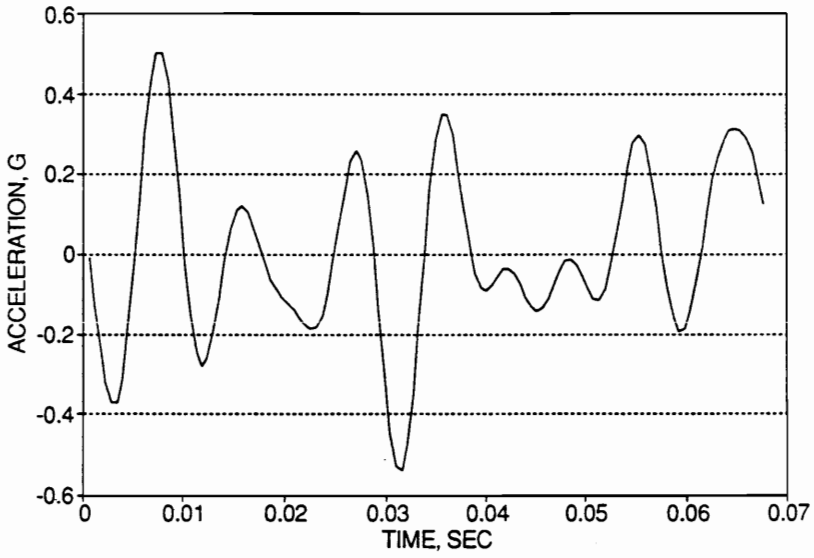

Figure 5-3. Vertical Acceleration of the Lumped Mass

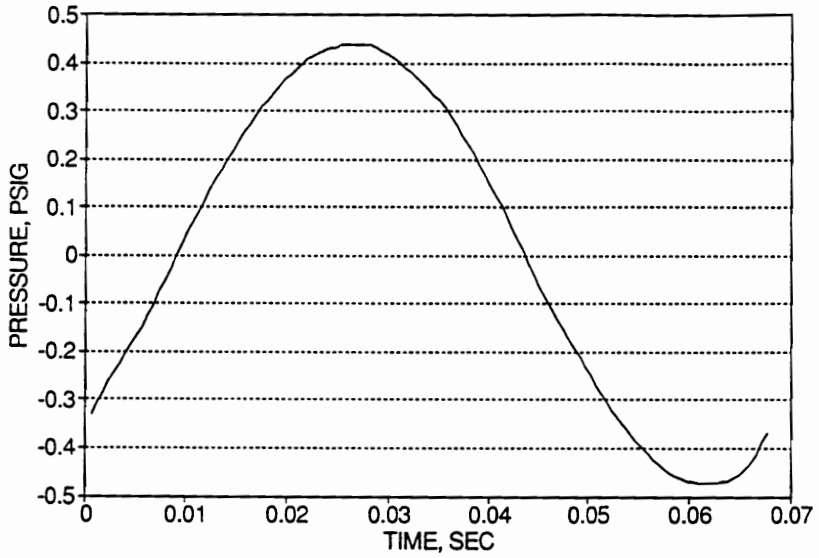

Figure 5-4. Crankcase Pressure

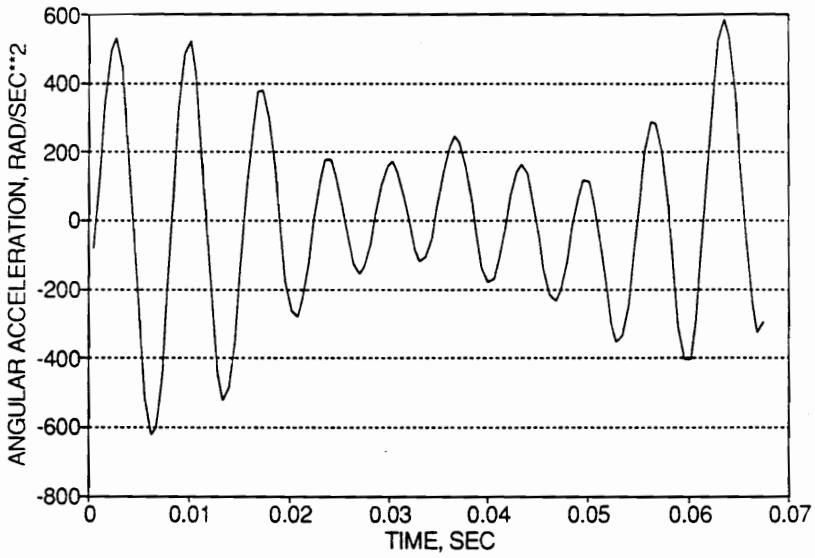

Figure 5-5. Angular Acceleration of Crankshaft

the mass moment of inertia of the crank with respect to crankshaft, J_2, the mass of the connecting rod, M_3, the mass moment of inertia of the connecting rod with respect to the crank-pin bearing, J_3, the friction force caused by the piston ring against cylinder wall, F, and the equivalent mass lumped at the top of the load cell, M_{EQ}.

The first five harmonics (10 components) of the load torques contributed by unit quantities of the seven system parameters, T_{LM}', T_{LE_2}', T_{LJ_2}' T_{LM_3}', T_{J_3}', T_{LF}', and $\ddot{y}D$ are used to construct the coefficient matrix, A; and the first five harmonics (10 components) of the force on the load cell and load torque contributed by the pressure of the crankcase, V, and T_{LPC}, are used to construct the known constant vector, B. Therefore, the linear equation system is of the form

$$A_{(10 \times 7)}X_{(7 \times 1)} = B_{(10 \times 1)} \qquad (5-5)$$

By least-square curve fitting Equation (5-5), the unknown parameters can be solved. Table 5-2 shows the solutions compared with measurements. The true values of the reciprocating mass and the mass of the connecting rod are measured by a triple beam balance and the true value of the mass moment of inertia of the connecting rod with respect to the crank-pin bearing, J_3', is calculated by Geomod, I-DEAS[1]. No measured values were determined for the eccentricity of the eccentricity of the crank with respect to crankshaft, the mass moment of inertia of the crank with respect to crankshaft, the friction force caused by the piston ring against cylinder wall, and the equivalent mass of the torque table lumped at the position of the load cell.

As discussed in Chapter 3, for this curve fitting, there exists a residual vector, r, satisfying

Table 5-2. Solutions to System Parameters

Parameter	Solution	True Value	Absolute Error
Reciprocating Mass, *lbm*	0.412	0.448	8.0%
Connecting Rod Mass, *lbm*	0.245	0.228	7.45%
Connecting Rod Mass Inertia, $lbm - in^2$	0.386	0.394	2.03%
Eccentricity of Crank, $lbm - in$	0.0	*NA*	*NA*
Crank Mass Inertia, $lbm - in^2$	9.274	*NA*	*NA*
Equivalent Lumped Mass, *lbm*	4.888	*NA*	*NA*
Friction Force, *lbf*	7.918	*NA*	*NA*

$$r = B - AX^* \qquad (3-77)$$

where X^* is the least-square solution for equation 5-5. The residual vector, r, physically describes the error of the fitting of the curve of the measured load torque, T_{L_M}, to the curve of the calculated load torque, T_{L_C}, in frequency domain.

$$T_{L_M} = VD - T_{LP_C}$$

$$T_{L_C} = T_{LM} + T_{LE_2} + T_{LJ_2'} + T_{LM_3} + T_{LJ_3'} + T_{LF} + M_{EQ}\ddot{y}D \qquad (5-6)$$

T_{L_M} can be evaluated from the kinematic construction and the measured signal, and since the system parameters have been quantified, T_{L_C} can be calculated.

Figures 5-6 and 5-7 compare T_{L_M} with T_{L_C} and shows the 'fittability' of the curve T_{L_C} to curve T_{L_M} for the first five harmonics in time and frequency domains (DC component is included in time domain). For first five harmonics, the curve fitting is accurate within 5 %.

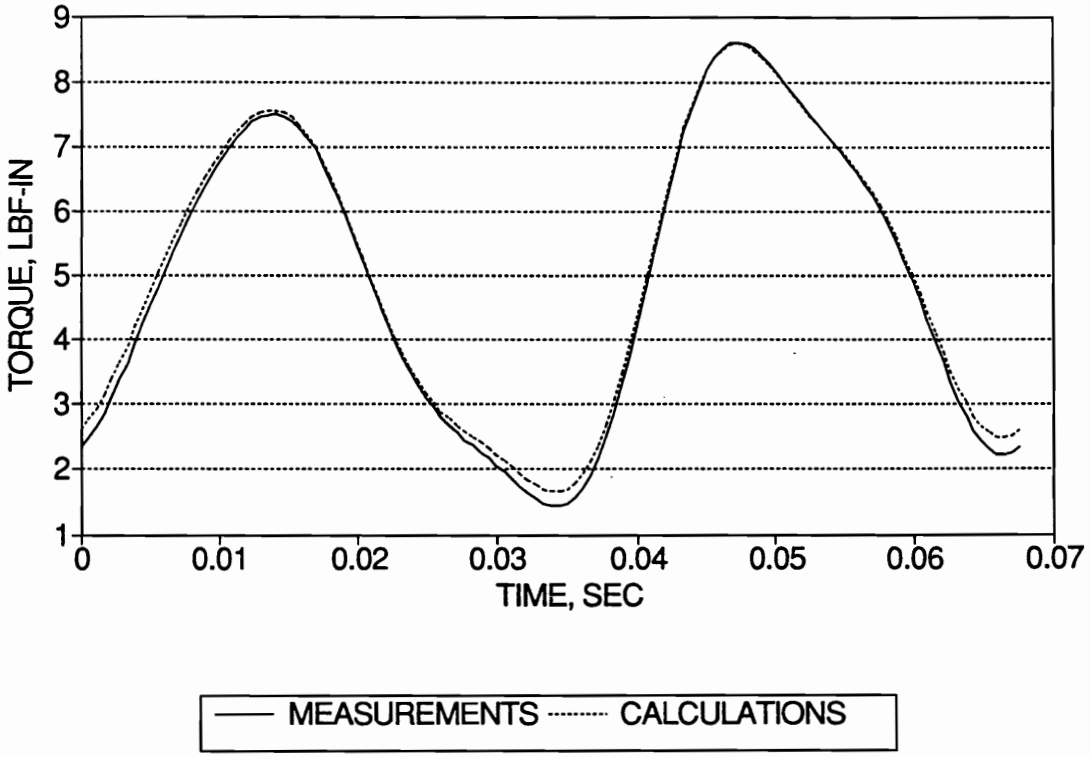

Figure 5-6. Load Torque Curve Fitting in Time Domain

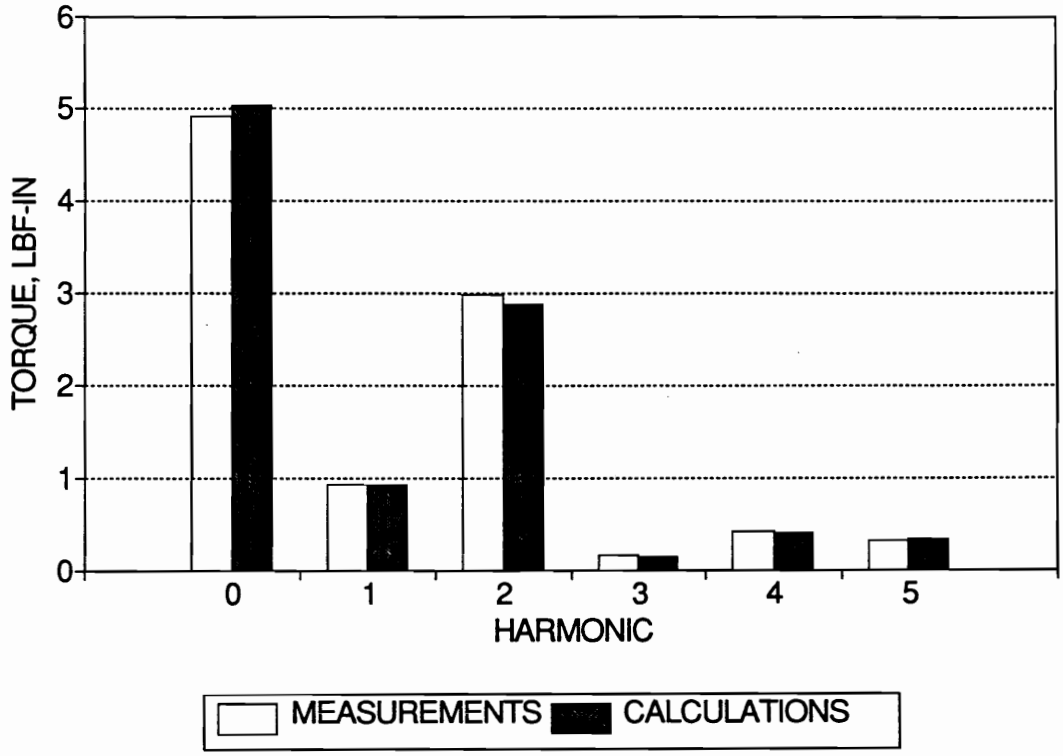

Figure 5-7. Load Torque Curve Fitting in Frequency Domain

5.1.1 Discussion

5.1.1.1 Friction Force

As discussed in Chapter two, the friction force of the piston ring is assumed constant through one complete cycle of the crankshaft; and in Chapter three, the kinetic friction force caused by the side thrust force is negligible. Figures 5-6 and 5-7 show the feasibility of this assumption, since for the first five harmonics, the curve fitted load torque is within 5% of the measurement. Since the friction force of the piston ring is independent from the back pressure of the piston, the force, F, as calculated above will be used to quantify the pressure-volume parameters.

5.1.1.2 Crankcase Pressure

In the solution algorithm of the system parameter quantification, the load torque contributed by the crankcase pressure has the same order as the load torque contributed by the mass of the slider-crank mechanism and the friction force of the piston rings, since the compressor used in this experiment has a small crankcase volume such that the crankcase pressure is sensitive to the piston displacement. In practice, the crankcase volume is larger than the swept volume of piston. For a multi-cylinder compressor, the crankcase volume can be kept constant or nearly constant by compensating the swept volume of each cylinder.

From Figure 5-4, the crankcase pressure is bounded to within less than 0.5 psig. The output tank pressure will be set to above 50 psig in the experiment of quantifying the

pressure-volume parameters such that the crankcase pressure is negligible in comparison with the cylinder pressure.

5.2 *Pressure-Volume Parameter Quantification by Direct Measurement of Load Torque*

After the system parameters are quantified, the compressor-motor system is run with the cylinder head installed to calculate the pressure-volume parameters. Assume that the system parameters are independent from the effect of the back pressure of the piston. Then, the governing equation of torque equilibrium for the load cell system is

$$VD = T_{LM} + T_{LE_2} + T_{LJ_2'} + T_{LM_3} + T_{LJ_3'} + T_{LF} + M_{EQ}'\ddot{y}D + T_{LP} \qquad (5-7)$$

Since the cylinder head is included in the torque table, the equivalent mass of the torque table lumped at the top of the load cell is changed and the new symbol, M_{EQ}', represents the quantity. The mass of the cylinder head is measured as 1.997 lbm, and the equivalent distance with respect to the center of rotation is 6.75 inches. Therefore, the equivalent effect of the mass of the cylinder head is a mass, $M_{EQ_{head}}$,

$$M_{EQ_{head}} = \frac{1.997 \times 6.75^2}{D^2} = 0.9099\text{lbm-in}^2 \qquad (5-8)$$

Then, the quantity M_{EQ}' is

$$M_{EQ}' = M_{EQ} + M_{EQ_{head}} \qquad (5-9)$$

The known parameters in this solution algorithm are the kinematic construction of the slider-crank mechanism, the experimental dimension shown as Table 5-1, and the system parameters shown as the solution part of Table 5-2.

The measurements required to quantify the pressure-volume parameters are the force acting on the load cell, the vertical acceleration of the torque table, the angular velocity of the crankshaft. Figures 5-8, 5-9, and 5-10 show these measurements through one complete cycle of crankshaft revolution. The period of one complete cycle of the crankshaft, T, is 0.0735 seconds.

As discussed in previous section, the angular acceleration of the crankshaft is calculated using Equation (5-2). Figure 5-11 shows the angular acceleration of the crankshaft through one complete cycle.

From the known parameters, the dynamics of the crankshaft and the vertical acceleration of the torque table, the load torques contributed by reciprocating mass, T_{LM}, eccentricity of the crank with respect to crankshaft, T_{LE_2}, mass moment of inertia of the crank with respect to crankshaft, $T_{LJ_2'}$, mass of the connecting rod, T_{LM_3}, mass moment of inertia of the connecting rod with respect to the crank-pin bearing, $T_{J_3'}$, friction force caused by the piston ring against cylinder wall, T_{LF}, and the torque table, $M_{EQ}'\ddot{y}D$, can be calculated.

With the measured torque, $T_{LP_{exp}}$, as

$$T_{LP_{exp}} = VD - T_{LM} - T_{LE_2} - T_{LJ_2'} - T_{LM_3} - T_{LJ_3'} - T_{LF} - M_{EQ}'\ddot{y}D \qquad (5-10)$$

and the objective function, $f(X)$, as

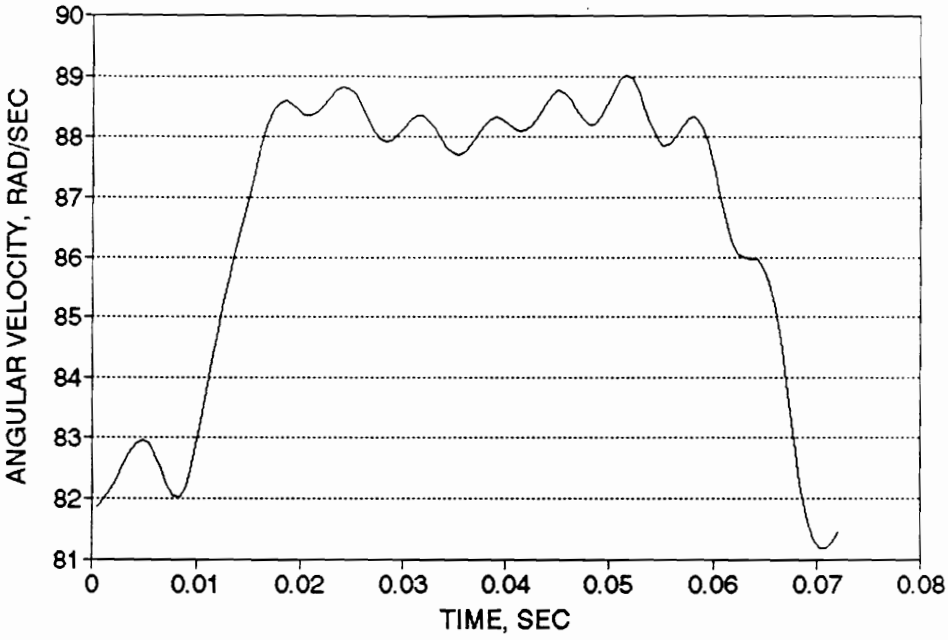

Figure 5-8. Angular Velocity of Crankshaft

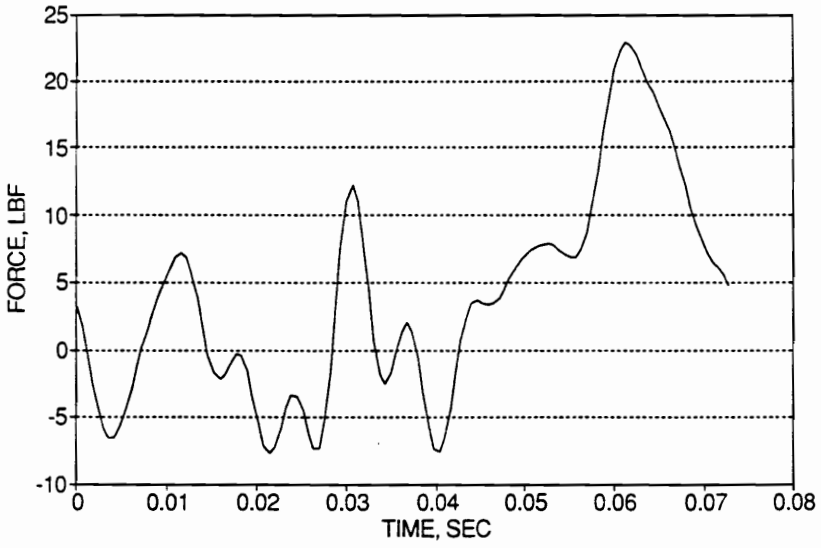

Figure 5-9. Force on Load Cell

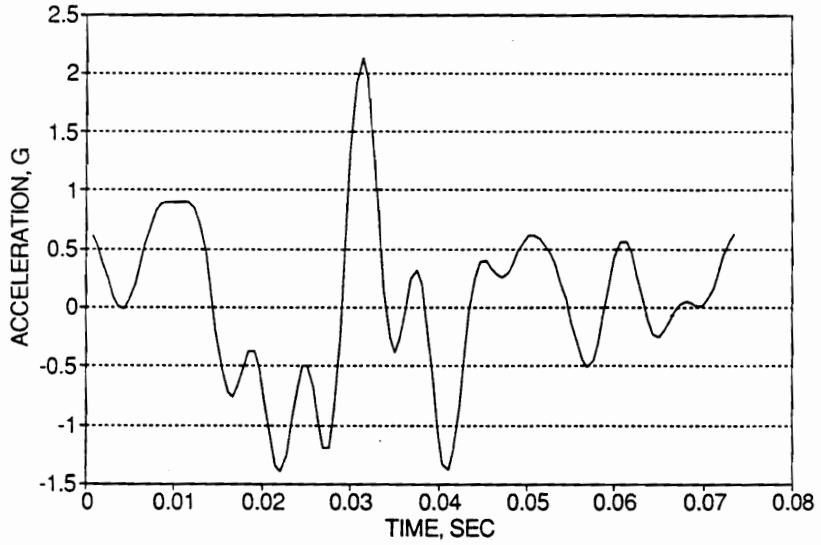

Figure 5-10. Vertical Acceleration of Lumped Mass

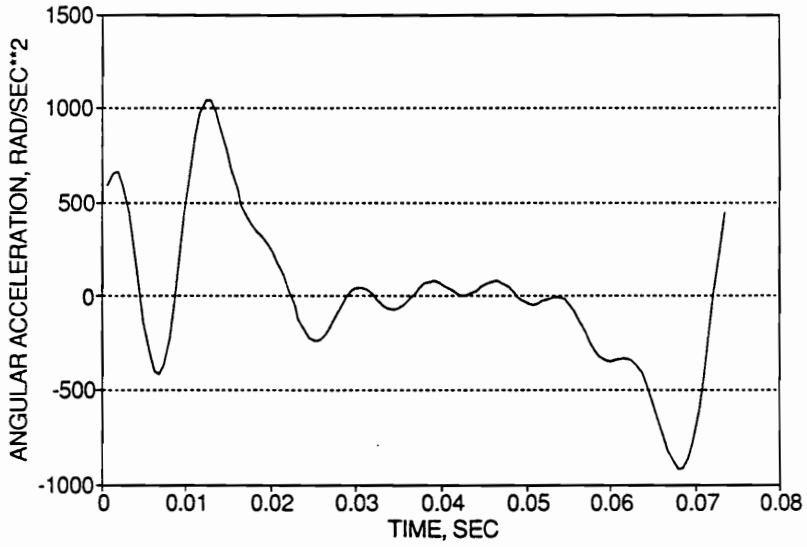

Figure 5-11. Angular Acceleration of Crankshaft

$$f(\mathrm{X}) = \sum_{i=1}^{120} (T_{LP}(\mathrm{X}) - T_{LP\mathrm{exp}})^2 \qquad (5-11)$$

by minimizing the objective function, the pressure-volume parameters, X, are to be solved.

$$\min f(\mathrm{X}) \qquad (5-12)$$

$$\text{subject to } l_i \le x_i \le u_i, \text{ for } i = 1, 2, \ldots, \mathrm{N}$$

Table 5-3 shows the conditions at which the compressor-motor system is run and the solutions. Figure 5-12 compares the measured pressure history through one complete cycle with the pressure history through one complete cycle calculated from the pressure-volume parameters.

Figures 5-13 and 5-14 compare the measurements and calculations of the load torque contributed by the cylinder pressure, $T_{LP\mathrm{exp}}$ and T_{LPC}, in time and frequency domains. The results show the time domain curve fitting is accurate within 3% for the first five harmonics.

Table 5-3. Experimental Conditions and Solutions

Conditions	
Throughput of Compressor, $10^{-3}lbm/$ sec	2.67
Output Tank Pressure, *psig*	57.5
Ambient Temperature, *F*	75
Period Per One Cycle, sec	0.0735
Simulated Leakage Throughput, *lbm/* sec	0.0
Cooling Condition	Normal
Solutions	
Output Pressure, *psig*	57.9
Pressure Fluctuation a_1, *psia*	7.64
Pressure Fluctuation a_2, *psia*	-0.35
Input Pressure, *psig*	1.8
Pressure Fluctuation b_1, *psia*	3.86
Pressure Fluctuation b_2, *psia*	1.53
Expansion Constant, κ_1	1.005
Compression Constant, κ_2	1.255

5.2.1 Discussion

5.2.1.1 Leakage

Figure 5-15 shows one complete pressure-volume cycle of the single stage air compressor schematically. For the case described above, by denoting swept volume as V_S, clearance volume as V_C, and the volume of the position at which the intake valve open,

$$\begin{aligned} \text{Volume induced per cycle} &= V_S + V_C - V_D \\ &= V_S + V_C - V_C\left(\frac{P_2}{P_1}\right)^{1/\kappa_1} \\ &= 6.1573 in^3 \end{aligned} \qquad (5-13)$$

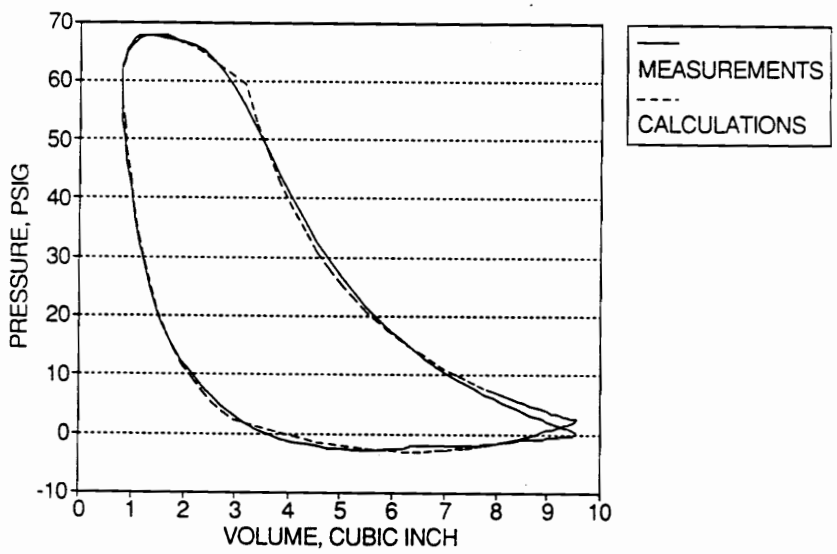

Figure 5-12. Pressure-Volume Diagram

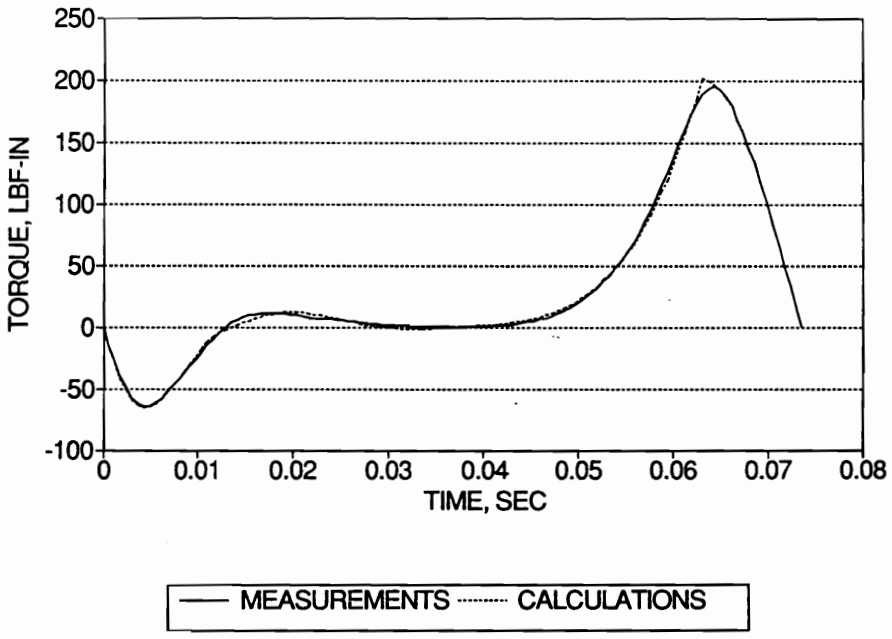

Figure 5-13. Load Torque Curve Fitting in Time Domain

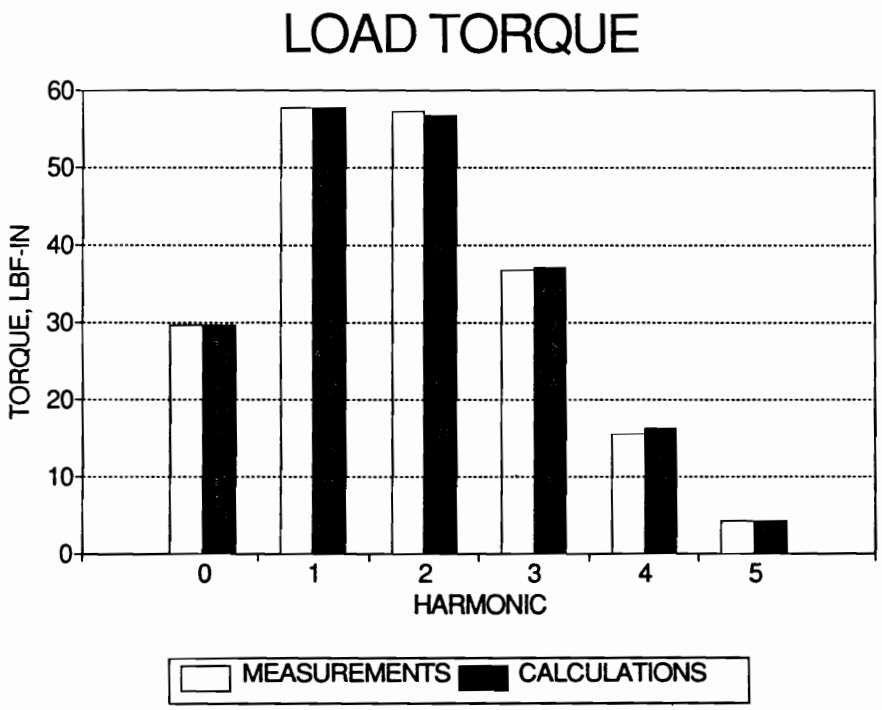

Figure 5-14. Load Torque Curve Fitting in Frequency Domain

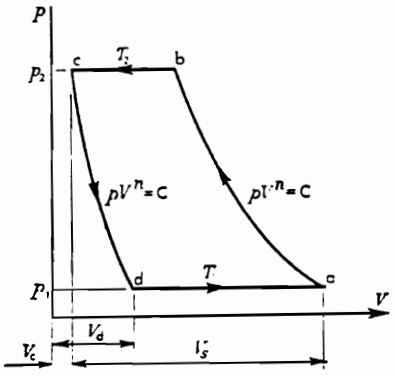

Figure 5-15. Schematic Diagram of Pressure-Volume Cycle

$$\text{Mass delivered per cycle} = V_l\rho = 2.188 \times 10^{-4} \text{ lbm} \quad (5-14)$$

Since the period of one complete cycle is 0.0735 second, the mass flow rate, $\dot{m}_D$, is

$$\dot{m}_D = \frac{2.537 \times 10^{-4}}{0.0735} = 3.699 \times 10^{-3} lbm/\text{ sec} \quad (5-15)$$

The mass throughput from the rotameter is

$$\dot{m} = \dot{V}\rho = 2.6705 \times 10^{-3} lbm/\text{ sec} \quad (5-16)$$

Then, the leakage is to be evaluated

$$\dot{m}_{leak} = \dot{m}_D - \dot{m} = 1.0285 \times 10^{-3} lbm/\text{ sec} \quad (5-17)$$

The leakage is approximately 28% of the mass delivered. Since in this case, no simulated leakage from the cylinder exists, the possible leakage paths are

1. leakage through the piston ring pack to the crankcase,

2. leakage from small openings in the piping and cylinder seals.

5.2.1.2 Operating Temperature

Figure 5-16 shows the measurement of the inlet temperature. The average is approximately 1 degree Fahrenheit higher than the ambient temperature. It can be attributed

to the effect of the heat transferred from the cylinder head which is always at a higher temperature than the ambient air temperature.

The exhaust temperature can be predicted as

$$T_2 = T_1\left(\frac{P_2}{P_1}\right)^{(\kappa_2-1)/\kappa_2} = 280°F \qquad (5-18)$$

Comparing the prediction of $280°F$ with the measurement of $276°F$ as shown in Figure 5-17, it is noticed that the measurement is approximately 4 degree Fahrenheit lower than the prediction. It also can be attributed to the effect of the heat transferred out from the exhaust air which is at the highest temperature within one cycle.

Theoretically, the cylinder air temperature is bounded within the inlet temperature and the exhaust temperature. Technically, an elaborate procedure is required to measure the cylinder air temperature, since the best position to locate the thermocouple is at the top surface of the piston. The cylinder temperature measured in this experiment can be interpreted as the temperature of cylinder head. Figure 5-18 shows the compressor is operating under a temperature approximately 226 degrees Fahrenheit.

5.2.1.3 Heat Exchanged

Figure 5-19 shows the compressor system schematically. From the principle of the conservation of energy, for any instant, this system is described as

$$\dot{W} + C_P\dot{m}_I T_I = C_P\dot{m}_L T_L + C_P\dot{m}_O T_O + \dot{Q} \qquad (5-19)$$

where:

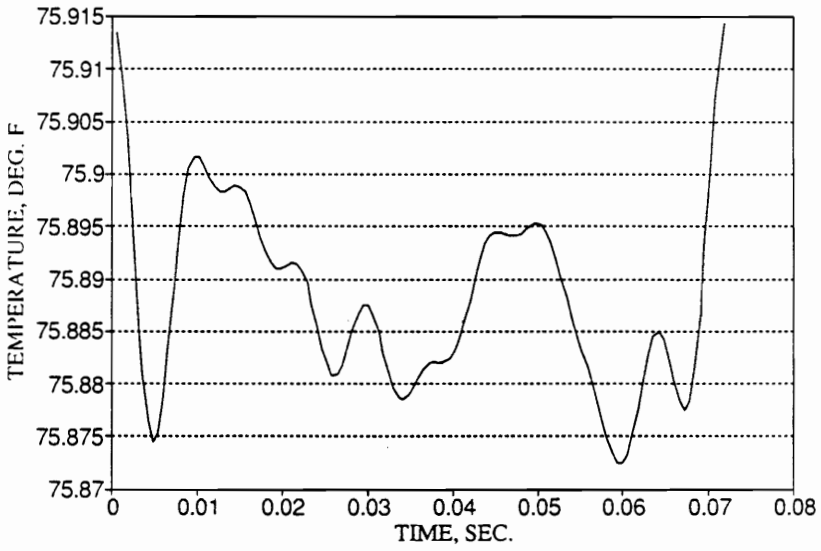

Figure 5-16. Inlet Temperature Measurement

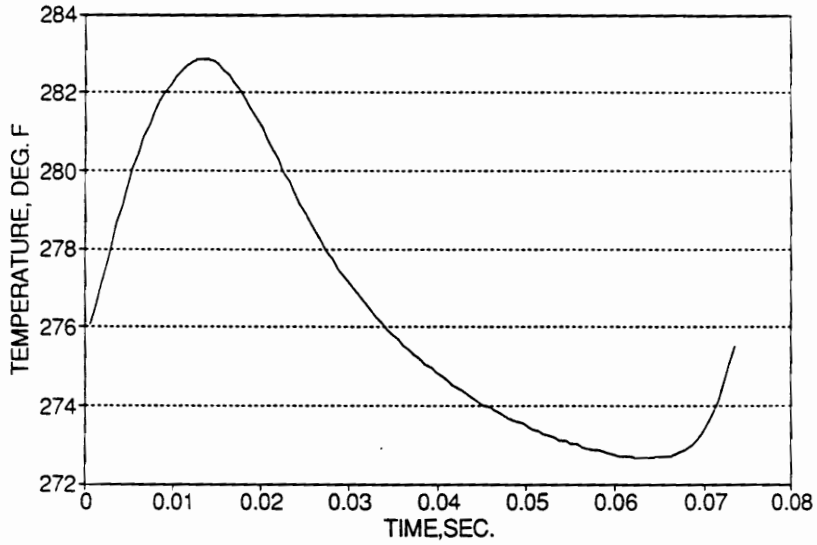

Figure 5-17. Exhaust Temperature Measurement

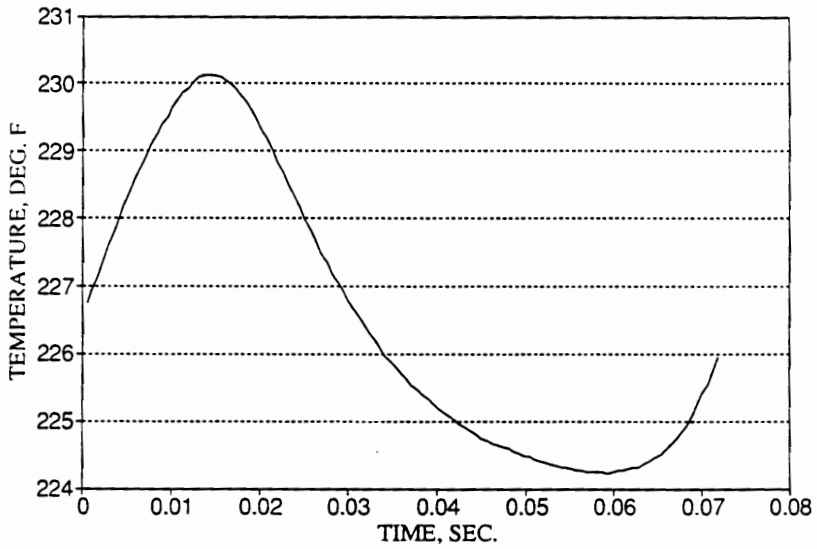

Figure 5-18. Cylinder Temperature Measurement

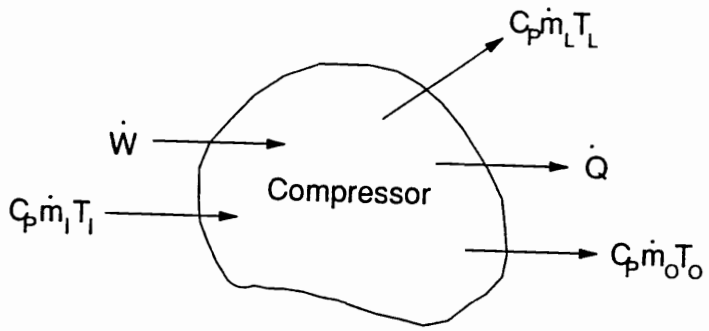

Figure 5-19. Energy Diagram of Compressor System

$\dot{W}_{in}$ power done on the system.

$C_P\dot{m}_I T_I$ enthalpy of the mass flow into the system.

$C_P\dot{m}_L T_L$ enthalpy of the leakage flow.

$C_P\dot{m}_O T_O$ enthalpy of the discharge flow.

$\dot{Q}$ rate of heat transfer.

Then the heat transferred from the compressor, $\dot{Q}$, can be calculated

$$\dot{Q} = \dot{W} + C_P\dot{m}_I T_I - C_P\dot{m}_L T_L - C_P\dot{m}_O T_O \qquad (5-20)$$

The work input the system can be evaluated by the integrating the load torque with respect to shaft angle. For one complete cycle,

$$\begin{aligned} W &= \int T_L d\theta \\ &= 245.432 \ lbf - in \end{aligned} \qquad (5-21-a)$$

This work input is consumed by compression work done on the air and the friction force of the piston ring against the cylinder wall. For one complete cycle,

$$\begin{aligned} W &= \int PdV + \int FdS \\ &= 237.766 \ lbf - in \end{aligned} \qquad (5-21-b)$$

Comparing Equations 5-21-a and 5-21-b, the work input differs from the work consumed by 3% because of numerical error. The input power can therefore be calculated as:

$$\begin{aligned} \dot{W} &= \frac{W}{T} \\ &= 0.5059\ hp \end{aligned} \qquad (5-22)$$

It is approximately the rating of the three phase motor, 1/2 hp.

The leakage path is to be simulated as an orifice as shown in Figure 5-20. Assume that the velocity in the cylinder is negligible and that the air is leaking with a velocity C. From the energy equation, for unit mass of the leaking air,

$$C_P T_2 = C_P T_1 + \frac{C^2}{2} \qquad (5-23)$$

The leakage velocity can be expressed as:

$$C = \sqrt{2C_P(T_2 - T_1)} \qquad (5-24)$$

Suppose the area of the orifice is A, then the leaking mass flow rate is

$$\begin{aligned} \dot{m}_L &= CA\rho \\ &= C_L\sqrt{(T_2 - T_1)} \end{aligned} \qquad (5-25)$$

From Equation (5-23), the leaking mass flow rate is proportional to the square root of the temperature difference between the cylinder air and the atmosphere, and C_L is the discharge coefficient of the leakage orifice.

For one complete cycle, the leakage air is

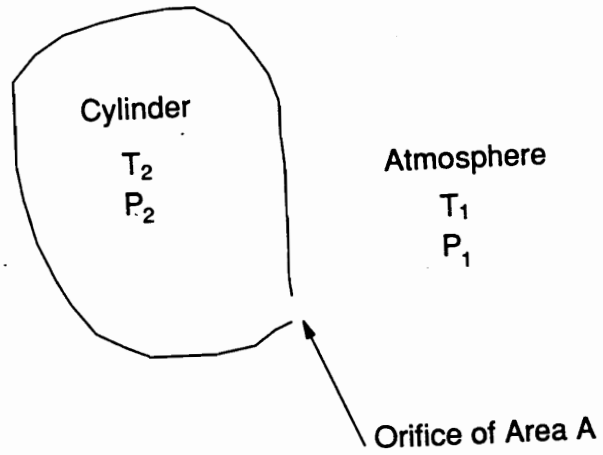

Figure 5-20. Leakage Paths

$$m_L = \int \dot{m}_L dt = \int C_L \sqrt{(T_2 - T_1)}\, dt \qquad (5-26)$$

Therefore, the discharge coefficient of the leakage orifice, C_L, can be calculated as

$$C_L = \frac{m_L}{\int C_L \sqrt{(T_2 - T_1)}\, dt} = 6.283 \times 10^{-5} lbm/\sec \sqrt{F} \qquad (5-27)$$

For one cycle, the heat transferred from the compressor into atmosphere, Q, then can be evaluated

$$Q = W + C_P m_I T_I - C_P m_O T_O - \int C_P C_L T_2 \sqrt{(T_2 - T_1)}\, dt = 0.02533 BTU \qquad (5-28)$$

The heat transfer rate, $\dot{Q}$, then can be determined.

$$\dot{Q} = \frac{Q}{T} = 0.34464 BTU/\sec \qquad (5-29)$$

5.2.2 Identification of the Operation Conditions of the Compressor

Now, the question to be answered is "If the compressor is operating under poor cooling conditions, or the if leakage increases, can these changes be detected by the pressure-volume parameters as calculated?". Three experiments were designed to answer this question.

1. The compressor is run under normal conditions with the cooling fan on and the leakage port off.

2. The cooling fan is turned off to simulate the poor cooling condition.

3. The leakage port is opened to simulate abnormal leakage.

Table 5-4 shows the conditions, solutions, and information calculated from the pressure-volume parameter.

From Table 5-4, The following phenomena are noticed.

- When the machine is operating under poor ventilation, the first harmonic of the discharge pressure fluctuations, a_1, is higher in comparison with the normal condition. It can be attributed to the heat that raises the temperature of the cylinder chamber after the discharge valve opens.
- As discussed in Chapter 2, poor ventilation increases the compression constant, κ_2, and leakage during compression decreases the compression constant, κ_2, because the leakage delays the pressure increase in the cylinder chamber.
- As discussed in Chapter 2, poor ventilation increases the expansion constant, κ_1, and leakage during expansion increases the expansion constant, κ_1, because the leakage accelerates the pressure drop of the cylinder chamber.
- In all these three cases, the first harmonics of the input pressures, b_1, are larger than input pressure. This means, during suction, the pressure in the cylinder chamber can be lower than atmosphere pressure because of the pressure drop across the suction valve.

Table 5-4. Solution List

Conditions			
Throughput of Compressor, lbm/sec	0.00267	0.00292	0.00216
Output Tank Pressure, *psig*	57.5	50	47.5
Ambient Temperature, *F*	75	75	75
Period Per One Cycle, sec	0.0735	0.0730	0.0722
Leakage Port Throughput, lbm/sec	**0.0**	**0.0**	**0.000723**
Cooling Fan	**On**	**Off**	**On**
Solutions			
Output Pressure, *psig*	57.9	50.6	48.2
Pressure Fluctuation a_1, *psia*	7.6	13.2	10.1
Pressure Fluctuation a_2, *psia*	-0.35	-0.023	-0.18
Input Pressure, *psig*	1.8	1.96	1.58
Pressure Fluctuation b_1, *psia*	3.86	4.52	3.88
Pressure Fluctuation b_2, *psia*	1.53	1.68	1.51
Expansion Constant κ_1	1.005	1.133	1.136
Compression Constant κ_2	1.255	1.398	1.223
Additional Information Calculated			
Total Leakage, lbm/sec	0.00103	0.00128	0.00211
Total Leakage Percentage,%	27.8	30.4	49.5
Exhaust Temperature, *F* *	280(276)	358(351)	238(236)
Input Power($T_L\dot{\theta}$), *hp*	0.5059	0.551	0.5003
Friction Power, *hp*	0.0326	0.0329	0.0332
Pressure Power, *hp*	0.458	0.528	0.458
Heat Transfer rate, *BTU/* sec	0.175	0.132	0.204

* Temperatures in () are measurements.

- With the leakage port closed, there is approximately 30 % of the mass delivered leaking from the piston ring pack, piping openings, and cylinder sealing and with the leakage port fully open, the leakage increases by approximately 20 %.

- The exhaust temperature measurements are only very slightly lower than the calculations because of the effect of the heat transferred out from the exhaust air which is at the highest temperature within one complete cycle.
- The power input calculated from the load torque matches with the power consumed by pressure and friction force within 3 %.
- The heat transfer rates decreases approximately 30% in poor ventilation condition and in this case, the power consumed by pressure increases by 15 %.

5.3 *Parameter Quantification by Measurement of Input Power of Motor*

The equation of motion for a rigidly coupled motor-compressor system developed in Chapter 1 is

$$T_M = T_L + J_S\ddot{\theta} + C_S\dot{\theta} \qquad (5-30)$$

Attempts to quantify the compressor parameters by solving Equation (5-30) were unsuccessful. According to the results shown in previous sections, the mathematical model for the load torque, T_L, is correct. This implies that if the load torque can be correctly measured, by applying the mathematical model developed in this research, then the compressor parameters can be solved. Therefore, the failure to solve Equation (5-30) can be attributed to inaccurate determination of the output torque from the three phase motor.

As discussed in Chapter 2, by acquiring the input currents and voltages for each phase, the input power of the motor can be calculated. The mechanical power developed in the shaft-compressor system is evaluated by subtracting the stator copper, rotor copper, and stator core losses from the input power of the motor. The output torque of the motor is then calculated by dividing the mechanical power developed by the angular velocity of the crankshaft.

$$T_m = \sum_{i=1}^{3} \frac{(I_i V_i - I_i^2 R_{1i} - I_{1i}^2 R_{Ci} - I_{2i}^2 R_{2i}')}{\dot{\theta}} \qquad (5-31)$$

There are two possible reasons which cause inaccurate measurement of the output torque of the motor.

1. The instantaneous input power of motor is the product of the instantaneous power supply voltage and the input current. For the DT2801-A board, data for each channel is acquired sequentially. As discussed in Chapter 5, the sampling rate is 9000 hz and the power supply is at 60 hz. Therefore, if the voltage and current are acquired on sequential channels, without other parameter in-between, these two data points will be 2.4° apart from each other. To compensate for the phase difference, the signals are recalculated by performing a Fourier transform and an inverse Fourier transform. This procedure causes numerical errors which diminish the accuracy of the measurement of the input power of the motor.

2. As discussed in Chapter 2, the slip of the motor is treated as constant through one complete rotor cycle. By using the average slip value, the power losses in the motor are calculated. Since there are nonzero ac components of the rotor angular velocity, this assumption is not accurate enough to describe the motor behavior.

5.4 *References*

1. Structural Dynamics Research Corporation, 1986, *I-DEAS Reference Manual, Geomod, Solid Modeling and Design*,

6.0 Summary and Conclusion

This dissertation has documented an attempt to assess the operating condition of reciprocating air compressors by quantifying the machine parameters. A theoretical expression for the load torque required to drive the air compressor in terms of the machine parameters and instantaneous angular position, velocity, and acceleration of the crank shaft was derived; in this theoretical derivation, a more accurate model to describe the inertia of a slider-crank mechanism was proposed and the effect of friction forces was discussed. The time domain and frequency domain solution techniques which are based on known machine construction and crank shaft dynamic and load torque measurements to determine the machine parameters were discussed in detail. The personal computer based system designed to measure the quantities necessary to solve the machine parameters and the quantities used to compare with calculations was also documented.

From these results, it is concluded that:

1. The traditional model for estimating the inertia of a slider-crank mechanism, lumped mass model, could cause significant error in comparison with exact model, continuously distributed mass model.

2. The friction force between the piston rings and the cylinder wall of a reciprocating compressor can be modeled as a constant force caused by the expansion of the piston rings, by neglecting the kinetic friction effects of the side thrust force.

3. By accurately measuring the angular velocity of the crankshaft and the load torque with least square curve fitting in the frequency domain, the system parameters of a single-stage reciprocating compressor, the piston ring friction force and the inertia of the slider-crank mechanism, can be solved within 8% in comparison with measurements.

4. By accurately measuring the angular velocity of the crankshaft and the load torque and curve fitting in the time domain, the pressure history of a single-stage reciprocating compressor can be estimated by solving for the pressure-volume parameters, intake and discharge levels, expansion and compression constants, and intake and discharge fluctuation characteristics. Parameters are found to be within 5 % of their observed values.

5. In addition to the angular velocity of the crankshaft and the load torque, the throughput of an air compressor is needed to decouple the effects of leakage and heat transfer.

6. The solution for multi-stage compressors can be achieved by decoupling the load torque of each cylinder pressure contribution by using time domain solution tech-

niques. The torque curve fitting is shown to be accurate within 5% for the first five harmonics and comparisons of predicted pressure histories with measurements shows a reasonable match for a four-stage two-cylinder high pressure air compressor (HPAC).

The attempts to quantify the load torque by measuring phase voltages and currents of the three phase motor were unsuccessful because of the technical problems in accurately acquiring the input power of the motor and a mathematical model not sufficiently accurate to describe the power losses in the three phase motor.

7.0 Recommendation for Further Research

As discussed in previous chapters, the non-intrusive non-destructive diagnosis of a reciprocating compressor is accomplished by fully understanding of the equation of motion of the mechanism and accurate measurements of the angular velocities of the crankshaft, load torque of the machine, and the throughput of the compressor. Among these, the physical behaviors of the slider-crank mechanism and the shaft system are described in detail, a practical procedure to accurately measure the angular velocity of the crankshaft is also proposed, and the throughput measurement can be easily achieved on line. However, it is not feasible to measure the load torque with a load cell and an accelerometer by using a torque table in the field.

In comparison with mechanical measurements of the load torque, the motor's input phase voltages and currents can be more accurately and effortlessly measured. However, in order to more accurately relate the load torque with the voltage and current measurements, two tasks are recommended for further research:

1. the voltage and current be acquired simultaneously by utilizing a parallel data acquisition board.

2. a more accurate mathematical model be used to describe the motor power losses.

Another alternative is to accurately measure the load torque using a torque cell based on the principle that the load torque on a shaft is proportional to the strains on the surface of the shaft.

Once the load torque can be 'practically' accurately measured, the solution techniques can be extended to a multi-stage multi-cylinder compressor which is mathematically more complicated because of a larger number of parameters to be quantified.

Appendix A. Experimental Study

The mathematical expressions for the load torque to be used to solve the compressor condition indicators are developed in Chapter 3 (Equations 3-28, 3-41, and 3-52). For these expressions to be useful, the instantaneous angular position, velocity, and acceleration of the crankshaft, and the instantaneous output torque of the motor (by measuring the instantaneous input phase current and voltage) or instantaneous load torque must be known. This appendix presents the personal computer based instrumentation system developed to accurately measure these quantities. This system is an extension of the work of Kanth[1] and Williams[2]. Also, the cylinder pressures and temperatures and the discharge flow rate from the air tank are to be measured to compare with those calculated from the mathematical model.

A.1 Instantaneous Shaft Velocity

The instrumentation system consists of two main elements: an incremental optical shaft encoder, and a signal preprocessing card that fits into an expansion slot of an IBM or IBM compatible personal computer.

A.1.1 Optical Shaft Encoder

Optical encoders are the most common form of shaft encoder owing to the high accuracies possible in their manufacture and use of a semiconductor light emitter. An optical encoder has there components: a light source and associated optical system which constantly emit the light, a disk composed of transparent and opaque parts which permits the light pass through the transparent part, and light detectors which work as counters, when they detect a light signal they emit a pulse. The operation principle is shown as Figure A-1[3].

A Model 714 ACCU-CODER manufactured by Encoder Product Co. is used in this procedure. The shaft encoder is coupled to the rigid shaft of the motor-load system with a toothed belt and pulley arrangement. Both pulleys are the same diameter, providing a one to one angular velocity ratio.

The shaft encoder is powered by the +12 volt power supply from the personal computer. The encoder has two output channels. The first output channel is a 1 PPR (pulses per revolution) signal; the pulses are of constant pulse width (20μ sec.) and magnitude (+5 volt), and occur at the same angular position of the encoder shaft during each rev-

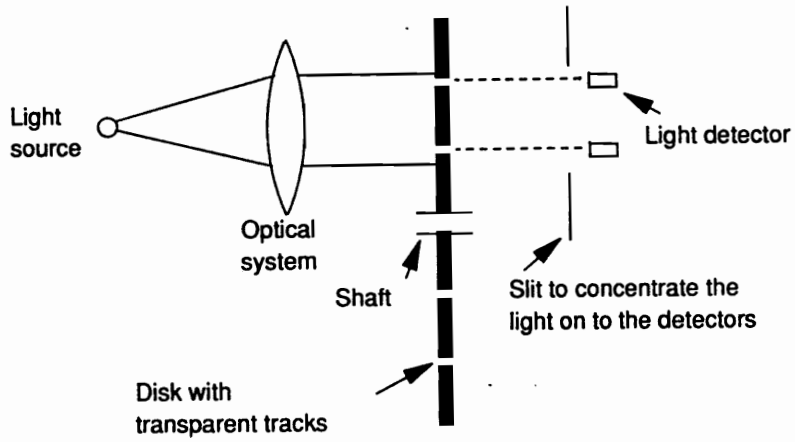

Pin	
A	Power ground
B	+12 volt
C	Not used
D	600 PPR
E	1 PPR
F	Signal ground

Figure A-1. Operation Principle of a Optical Shaft Encoder

olution. The second output channel is a 600 PPR signal; the pulses are of constant pulse width (20μ sec.) and magnitude ($+5$ volt), and occur at even angular increments of the encoder shaft. The 600 PPR signal is a frequency modulated signal; the instantaneous frequency of the signal is direct proportional to the instantaneous angular velocity of the encoder shaft (and thus to the instantaneous velocity of the crankshaft of the air compressor)[4]. The pin assignment for the shaft encoder is shown as Figure A-1.

A.1.2 Signal Preprocessing Card

The signal preprocessing card is an extension of the work of Williams[2] in 1989. This card is designed to fit into an expansion slot of an IBM or IBM compatible personal computer. The function of this card is to convert the frequency modulated pulse train from the shaft encoder into an amplitude modulated voltage that is directly proportional to the angular velocity of the crankshaft of the air compressor. The output voltages of the signal preprocessing card reflect both the AC and DC components of the angular velocity of the shaft.

Figure A-2 shows a schematic of the signal preprocessing circuitry. All power for the card, as well as the power supply for the optical shaft encoder are obtained from the expansion slot of the personal computer.

The card consists of two separated circuits. The first circuit uses a flip-flop to convert the 1 PPR signal from the shaft encoder into an alternating 0 volt and 5 volt signal that changes state each time the shaft undergoes one complete revolution. This output signal is used as a trigger for the analog to digital data acquisition system.

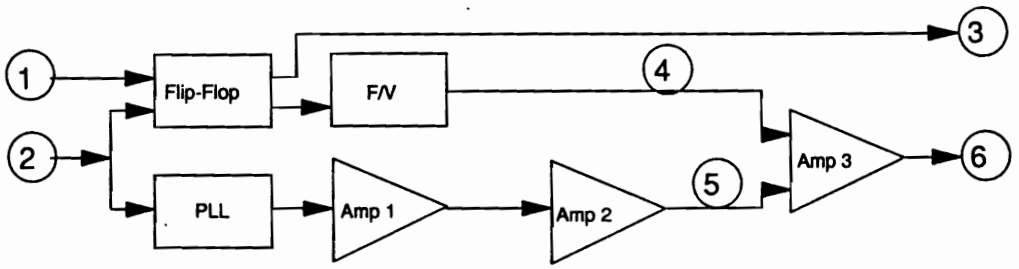

1 1 PPR from shaft encoder

2 600 PPR from shaft encoder

3 1 PPR flip-flop signal

4 Voltage proportional to average shaft velocity

5 Voltage proportional to AC shaft velocity component

6 Voltage proportional to total shaft velocity

Figure A-2. Schematic of Signal Preprocessing Circuitry

The second circuit in this card converts the 600 PPR signal from the shaft encoder into a voltage that is directly proportionally to the instantaneous angular velocity of the shaft. This circuit has two main branches; a phase-locked loop circuit that produces a voltage that is proportional to the AC component of the angular velocity of the shaft, and a frequency to voltage converter circuit that produces a voltage that is proportional to the DC component of the angular velocity of the shaft. The voltage corresponding to the AC and DC components of the angular shaft velocity are amplified so they are scaled the same, and summed to produced an output voltage that is directly proportional to the total angular velocity of the shaft.

A.1.2.1 Flip-Flop

The D flip-flop is widely used in computer circuitry and is represented schematically in Figure A-4. Preset, clear, and clock are the inputs of the flip-flop; Q and $\overline{Q}$(complement of Q) are the outputs. Figure A-3[5] shows the function table of a D flip-flop.

In the signal preprocessing card, an SN74LS74AN DUAL D FLIP-FLOP chip is used to convert the 1 PPR and 600 PPR signals into alternating 0 volt and +5 volt signals. The chip consists of two D flip-flop circuits with the same power supply. The pin-out for the chip is shown in Figure A-4. Since the preset and the clear for both D flip-flops are left unconnected with inputs, they float on high level voltage (+5 volt)[6]. The output signal for the 1 PPR input from shaft encoder is taken as an output signal of the pre-processing card and used a trigger for the analog to digital board, and the output signal for the 600 PPR input from shaft encoder is used as input to the F/V converter.

INPUT				OUTPUT	
PR	CL	CK	D	Q	$\bar{Q}$
L	H	X	X	H	L
H	L	X	X	L	H
L	L	X	X	H*	H*
H	H	↑	H	H	L
H	H	↑	L	L	H

*: This configuration is nonstable

H: High level

L: Low level

X: Irrelevent (any input)

↑: Transition from low to high

Figure A-3. Function Table of D Flip-Flop

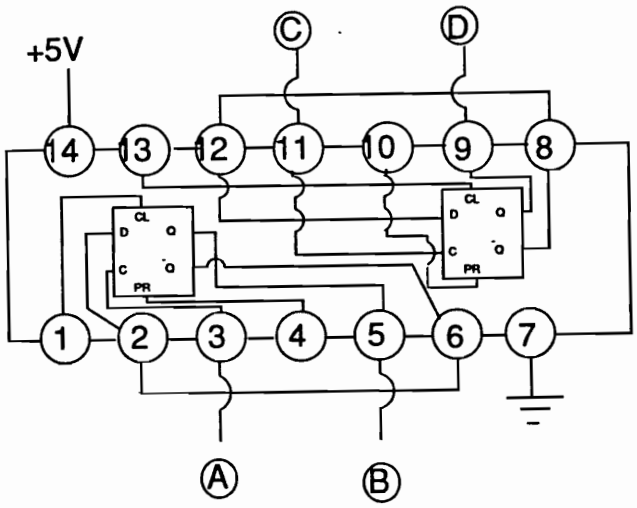

A 600 PPR from shaft encoder

B To F/V

C 1 PPR from shaft encoder

D To output port

Figure A-4. Circuitry Arrangement of the Flip-Flop

A.1.2.2 Frequency-to-Voltage Converter

A frequency to voltage converter is used to produce a voltage that is proportional to the DC component of the angular velocity of the encoder shaft (the average angular velocity of the crankshaft). The frequency to voltage converter used is an Analog Devices Model 451L F/V. Since the pulse train from the shaft encoder is too narrow (20μ second) to drive the frequency to voltage converter, the 600 PPR signal is first passed through the flip-flop chip, and then into the frequency-to-voltage converter.

As shown in Figure A-5, the input signals are applied directly into a comparator, which is internally set to provide a $+1.4V$ threshold with $\pm 50mV$. This threshold offers noise immunity for the input signal level. Following the input comparator is a precision charge dispensing circuit with a filter and a output amplifier where the comparator signal is converted to a dc voltage. When the input comparator changes state, C_C is alternately charged from a precision voltage reference and discharged through the summing point of the output amplifier, A_2. A current to voltage conversion is then accomplished by R_F. The current pulse from the charge dispensing circuit are integrated by C_F to reduced the ripple. Added filtering for low frequency input signals is provided by an adaptive filter at the output of the charge dispensing circuit[7]. The output signal from the frequency to voltage converter is scaled as 200 RPM per volt for the AC component of the angular velocity of the shaft encoder; then is taken as a output signal of the preprocessing card.

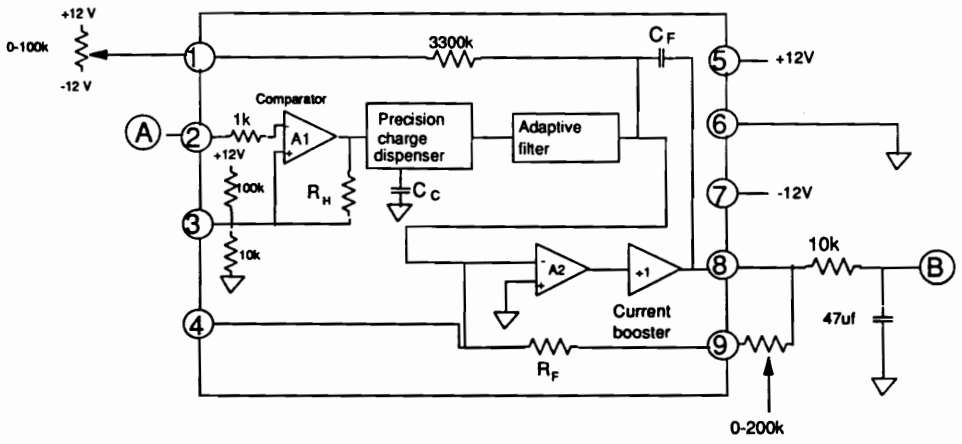

A 300 PPR signal from flip-flop
B Voltage proportional to average shaft velocity to amplifier and output port

Figure A-5. Circuitry Arrangement of the Frequency to Voltage Converter

A.1.2.3 Phase-Locked Loop Circuit

The purpose of the phase-locked loop circuit is to convert the frequency modulated 600 PPR signal from the shaft encoder into an amplitude modulated output signal that is proportional to the AC component of the angular velocity of the shaft.

As shown in Figure A-6, a phase-locked loop circuit consists of there basic elements: a phase detector, a loop filter, and a voltage controlled oscillator (VCO). The phase detector compares the phase of the input signal against the phase of the output of the VCO. The output from the phase detector is a voltage proportional to the difference between the frequencies of its two inputs. This error signal is then filtered by the loop filter and applied to the VCO. When the loop is 'locked', the VCO control voltage (the output voltage from the loop filter) is such that the frequency of the output signal from the VCO is exactly equal to the average frequency of the input signal. The output from the loop filter is a voltage (VCO control voltage) proportional to the difference between the instantaneous frequency and the average frequency of the input signal[8,9]. The input signal is the 600 PPR signal from the optical shaft encoder; the output voltage from the loop filter is proportional to the AC component of the angular velocity of the shaft, and then is taken as a output signal of the signal preprocessing card.

National Semiconductor Corporation's Model LM565CN Phase Locked Loop chip is used in the phase-locked loop circuit. Linear circuit performance for average shaft speed from 600 RPM to 4500 RPM is achieved by connecting one of three capacitors to the phase-locked loop chip with a user selectable switch accessible at the back of the signal preprocessing card. The three capacitors ensure linear circuit performance over a range of 600 RPM to 1200 RPM, 1000 RPM to 2400 RPM, and 2000 RPM to 4500 RPM, for

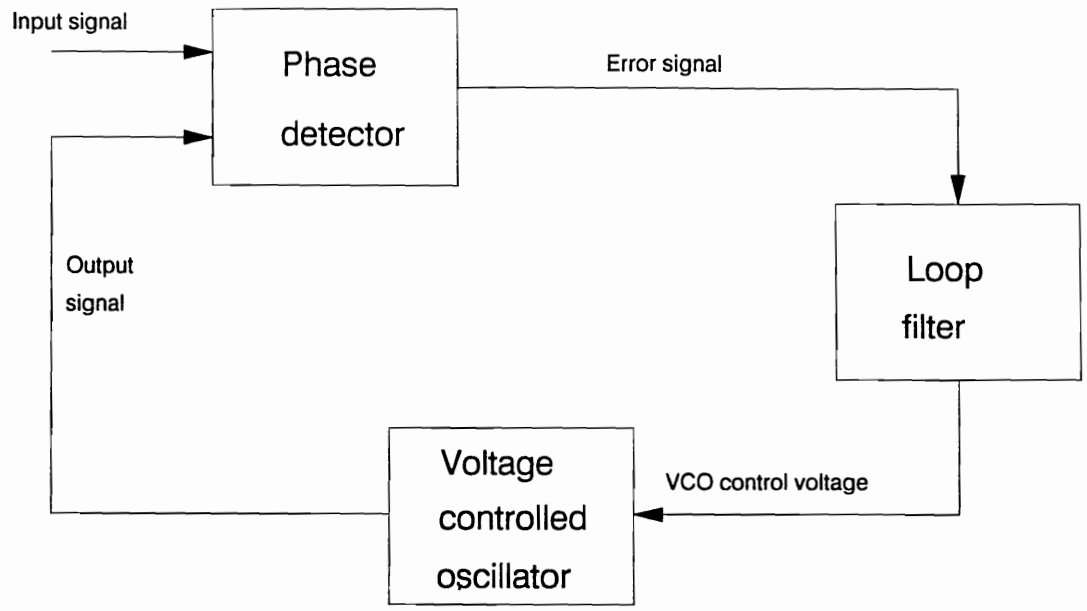

Figure A-6. Operation Principle of a Phase-Locked Loop Circuit

the switch position 1, 2, and 3, respectively[2]. The arrangement of the phase-locked loop circuit is represented schematically in Figure A-7.

A.1.2.4 Operational Amplifier

Three 741 operational amplifiers are used in the signal preprocessing card. Numbered in Figure A-2, Amplifier 1 receives the signal from the phase-locked loop circuit and scales the output such that 1 volt output represents 40 RPM of the AC component of the angular velocity of the encoder shaft, Amplifier 2 changes the scale of the output signal from Amplifier 1 to -200 RPM per volt, and Amplifier 3 receives the 200 RPM per volt output signal from the frequency to voltage converter for the DC component of the angular velocity of the encoder shaft, and the -200 RPM per volt output signal from Amplifier 2 for the AC component of the angular velocity of the encoder shaft; then produced a output signal of 200 RPM per volt for the total angular velocity of the encoder shaft. The circuitry arrangement for the three amplifier are shown in Figure A-8, A-9, and A-10[7].

A.1.2.5 Specifications of Final Design

Input and output for the preprocessing card is achieved via two standard DB-9 connectors. Figure A-11 shows a complete circuit diagram and Figure A-12 shows the pin assignments for the connectors.

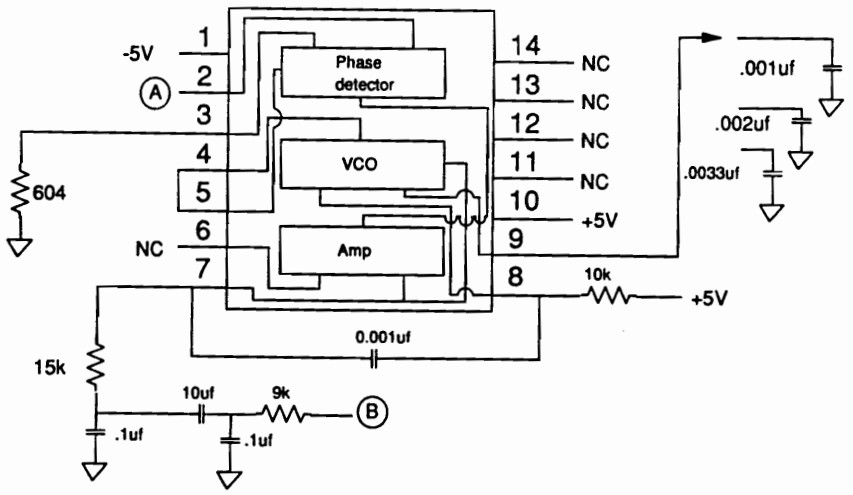

A 600 PPR siganl from shaft encoder

B Voltage proportional to AC shaft velocity component

Figure A-7. Circuitry Arrangement of the Phase-Locked Loop Circuit

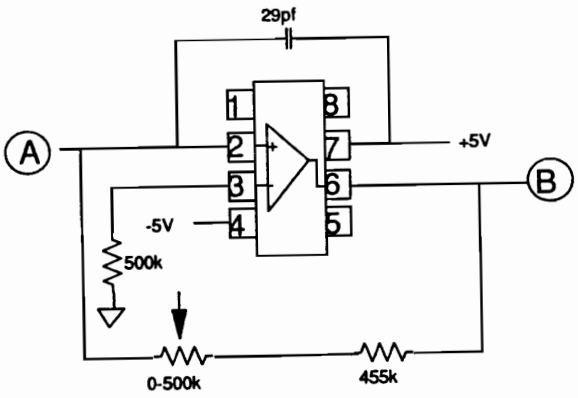

A Signal from PLL

B To Amplifier 2 and output port

Figure A-8. Circuitry Arrangement of Amplifier 1

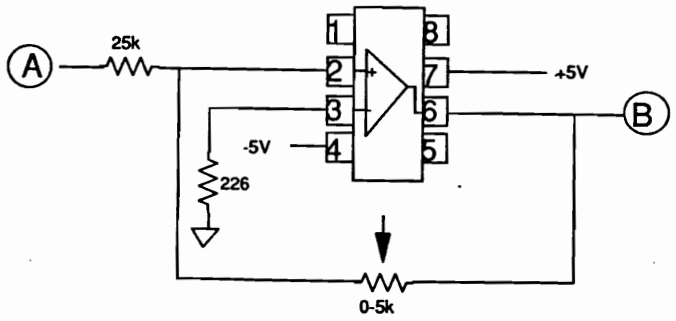

A Signal from Amplifier 1

B To Amplifier 3 and output port

Figure A-9. Circuitry Arrangement of Amplifier 2

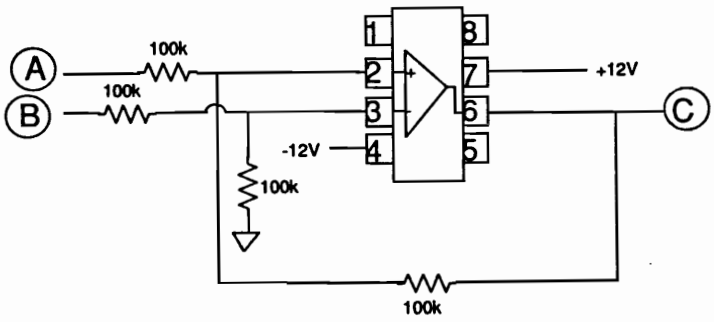

A Signal from Amplifier 2

B Signal from F/V converter

C To output port

Figure A-10. Circuitry Arrangement of Amplifier 3

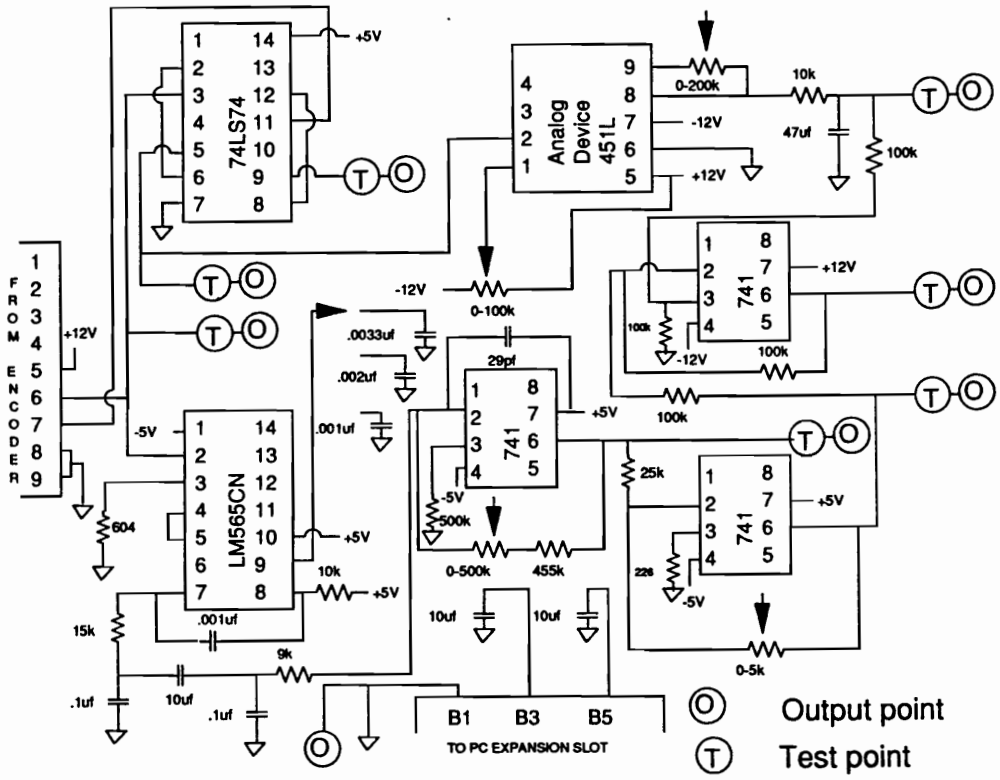

Figure A-11. Circuit Diagram the Signal Preprocessing Card

Pin No.	Output Connector (To A/D Board)	Input Connector (From Optical Encoder)
1	$\dot{\theta}_{AC}$ (40 RPM/V)	Not Used
2	$\dot{\theta}_{DC}$ (200 RPM/V)	Not Used
3	$\dot{\theta}_{AC}$ (-200 RPM/V)	Not Used
4	$\dot{\theta}_{DC+AC}$ (200 RPM/V)	Not Used
5	1 PPR Flip Flop	+12 V
6	GND	600 PPR (From Encoder)
7	600 PPR (From Encoder)	1 PPR (From Encoder)
8	Not Used	GND
9	600 PPR Flip Flop	GND

Figure A-12. Pin Assignment for Input and Output Connector

A.1.2.6 Calibration Procedure

The following calibration procedure for the preprocessing card has been developed and redeveloped to accurately reflect the instantaneous velocity of the shaft encoder. The calibration is performed by adjusting the four trimpot potentiometers R1, R2, R3, and R4, (see Figure A-11), accessible at the top of the card.

The following equipment is needed in this calibration procedure.

1. DC precision power supply. (Hewlett Packard DC POWER SUPPLY, Model 6200 DC)

2. Sine wave generator. (BK Precision 3020 Sweep/Function Generator)

3. Voltage controlled generator. (Wavetek Voltage Controlled Generator VCG Model 111)

4. Precision AC/DC digital voltmeter. (Fluke 8050A Multimeter)

5. Precision frequency counter. (Hewlett Packard 5315A Universal Counter)

The following steps outline the calibration procedure.

1. Install the signal preprocessing card in the computer, turn on the computer and allow the card to warm up for more than 15 minutes, and set the user selectable switch on the front of the card to the desired speed range.

2. Zero the frequency to voltage converter chip: adjust trimpot R1 such that the voltage at output pin 2 is zero.

3. Calibrate the frequency to voltage chip for the DC component of the speed of the encoder shaft:

   a. Set the VCG to a square wave output, set the base frequency of the VCG to the proper frequency to simulate the encoder's 600 PPR signal, and check the base frequency of the VCG using the precision frequency counter.

   b. Input the artificial signal of the VCG to the preprocessing card. (input pin 6 for the 600 PPR signal, and input pin 8 for the signal ground)

   c. Using the digital voltmeter, adjust trimpot 2 such that output pin 2 reads 1 volt per 200 RPM of the simulated shaft velocity.

4. Calibrate the phase locked loop circuit chip for the AC component of the speed of the encoder shaft:

   a. Calculate the input voltage to make 10% of the VCG output frequency: use the DC power generator to generate a voltage, use the digital volmeter to check this voltage, input this voltage to the VCG with the simulated base frequency, use the precision frequency counter to check the output frequency of the VCG, and then determine the voltage to make 10% of the simulated base frequency.

   b. Generate a signal to simulate the AC component for the shaft encoder: using the frequency counter and digital voltmeter, set the function generator to gen-

erate a sine wave of 1/600 of the base frequency, and an RMS voltage equal to the voltage calculated in previous step.

c. Input the signal generated in previous step to the VCG with base frequency. Now, the output signal of the VCG simulates an encoder signal with DC component of the base frequency and AC component of 10% of the base frequency.

d. Input the signal of the VCG in previous step to the preprocessing card. (input pin 6 for the 600 PPR signal and input pin 8 for the signal ground)

e. Using the digital voltmeter, adjust trimpot 3 such that output pin 1 reads 1 volt per 40 RPM of the simulated shaft AC velocity component.

f. Using the digital voltmeter, adjust trimpot 4 such that output pin 3 reads 1 volt per 200 RPM of the simulated shaft AC velocity component.

Now, the calibration procedure is completed. When connected to the shaft encoder, the output of output pin 4 of the signal preprocessing card will be a voltage proportional to the instantaneous angular velocity of the shaft encoder. Each output volt from pin 4 corresponds to an angular shaft velocity of 200 RPM of the encoder rotor[2].

A.2 Verification of Load Torque

In order to verify the load torque, the air compressor is mounted on a torque table that is attached to the base of the experimental setup with two pillow block bearings. The

axis of the bearings is coincident with the axis of the crankshaft of the air compressor. A large thrust bearing is mounted on the support shaft for the table between the table and the base of the experimental setup to reduce the support shaft deflections during operation. A compressive preload is applied to the thrust bearing by using a threaded rod that passes through the center of the support shaft.

In the experimental setup described above, the load is mounted such that it pivots about its driving axis and constrained from rotating during operation by a load cell attached between the base plate of the experimental setup and load torque table. Figure A-13 describes the model of single degree of freedom for the measurement of the load torque and Figure A-14 shows the free body diagram of the torque table. The equation of torque equilibrium with respect to point O is:

$$T_L - F(L_1 + L_2) + MgL_1 = -M\ddot{y}L_1 \qquad (A-1)$$

Then, F, the force measured by the load cell can be expressed as:

$$F = \frac{T_L + MgL_1 + M\ddot{y}L_1}{L_1 + L_2} \qquad (A-2)$$

In Equation (A-2), the term MgL_1 is constant and can be ignored since the zero position of the load cell can be adjusted to negate its effects. Then Equation (A-2) can be re-written as:

$$F = \frac{T_L + M\ddot{y}L_1}{L_1 + L_2} \qquad (A-3)$$

Now, set

$$R = L_1 + L_2 \qquad (A-4)$$

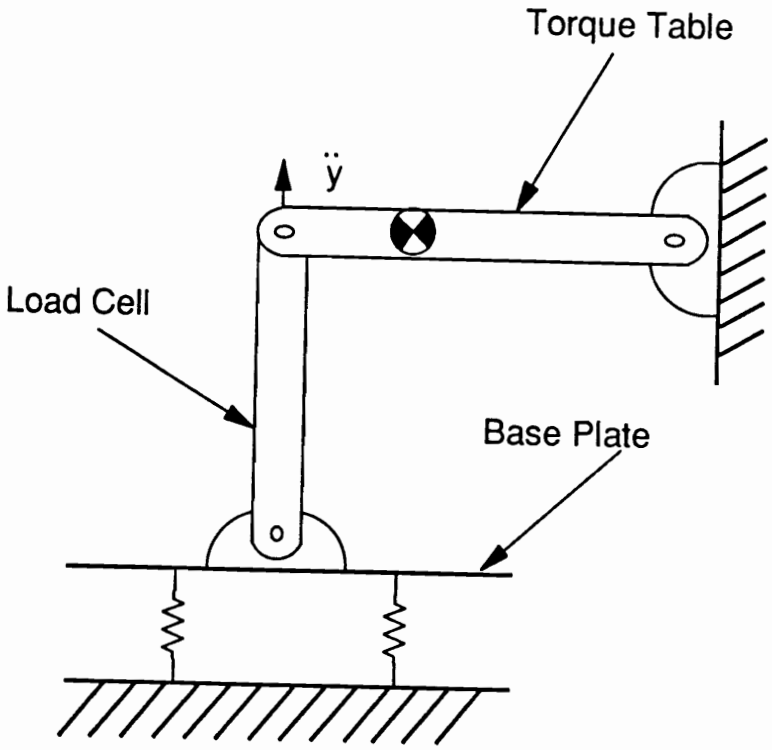

Figure A-13. Single Degree of Freedom Model of Torque Table and Base Plate

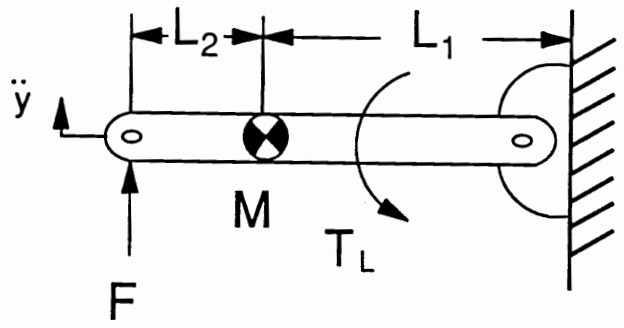

Figure A-14. Free Body Diagram of Torque Table

and

$$ML_1 = M_{EQ}R \qquad (A-5)$$

Then, Equation (A-2) can be rearranged as:

$$FR = T_L + M_{EQ}\ddot{y}R \qquad (A-6)$$

where

F	Force measured by the load cell.
R	Distance from the axis of crankshaft to the load cell.
T_L	Load torque.
M_{EQ}	Equivalent mass of the load torque table and the compressor lumped at point A.
$\ddot{y}$	Vertical acceleration of point A.

Equation (A-6) is to be used to solve the compressor parameters by substituting the load torque, T_L, by a function of the compressor kinematic constructions, dynamics of the crankshaft, and the compressor parameters analytically.

A.2.1 Force Measurement

In this experiment, a beam-type strain gauge load cell with power supply system designed by R. G. Mitchiner and J. Williams[2] is used to measure the reaction force. This load cell were designed to measure both AC and DC components of the reaction force of the torque table. The design specification and calibration data are refered to J. Williams[2] thesis.

A.2.2 Vertical Acceleration of the Torque Table

In Equation (A-6), the vertical acceleration of the torque table must be measured to evaluate the load torque. In this experiment, a piezoelectric accelerometer is used to measure the vertical acceleration of the torque table. Since all the data are acquired at the steady state of the motor-compressor system, the DC component of the vertical acceleration of the torque table can be assumed to zero and the AC components to be the absolute value of the acceleration.

A PCB 308B03 accelerometer with an PCB Power Supply 482A is used to measured the vertical acceleration of the base plate. Table A-1[11] lists the specification of the accelerometer.

Table A-1. Accelerometer Specifications

Manufacturer	PCB Piezoelectrics, Inc.
Model	308b03
Voltage sensitivity	50 mV/g
Resonant frequency	25 kHz
Linear frequency range	1 - 3000 Hz

A.3 Pressures of Cylinder Chamber and Crankcase

A PCB 111A02 dynamic pressure transducer with an ICP Power Supply 482A is used to measure the compressor cylinder chamber and crankcase pressures. Table A-2[11] list the specification of the pressure transducer.

A piezoelectric pressure transducer can only measure the AC components of pressure. Therefore, in this measurements, two assumptions are made.

- The DC component of the crankcase pressure is assumed to be zero since the measurement were performed in steady state.
- The pressure of the cylinder chamber at bottom dead center position is assumed to be atmosphere pressure.

Table A-2. Specifications of Pressure Transducer

Manufacturer	PCB Piezoelectrics, Inc.
Model	111A21/62
Serial Number	607
Sensitivity	35.5 mV/psi
Linearity	< 1.0 %F.S.
Calibration Range	0 - 100 psi
Input Time Constant	1 sec.
Rise Time	2 μsec.
Natural Frequency	300 kHz
Output Impedance	< 100ohms

A.4 Temperature Measurement

Three Omega Type J Iron Vs. Copper-Nickel thermocouple probes are are used to measure temperatures. These probes are connected to exhaust port, intake port, and cylinder chamber of the compressor respectively, a user selectable switch box used to select the channel desired, then to a DC millivolt amplifier.

With a compensation circuit built in the DC millivolt amplifier, the reference temperature is the ice point (32°*F*). The voltage outputs of thermocouples are not linearly proportional to the temperatures detected. The temperature-voltage curve of the J-type thermocouple is shown as Figure A-15 (from 30°*F* to 400°*F*)[12].

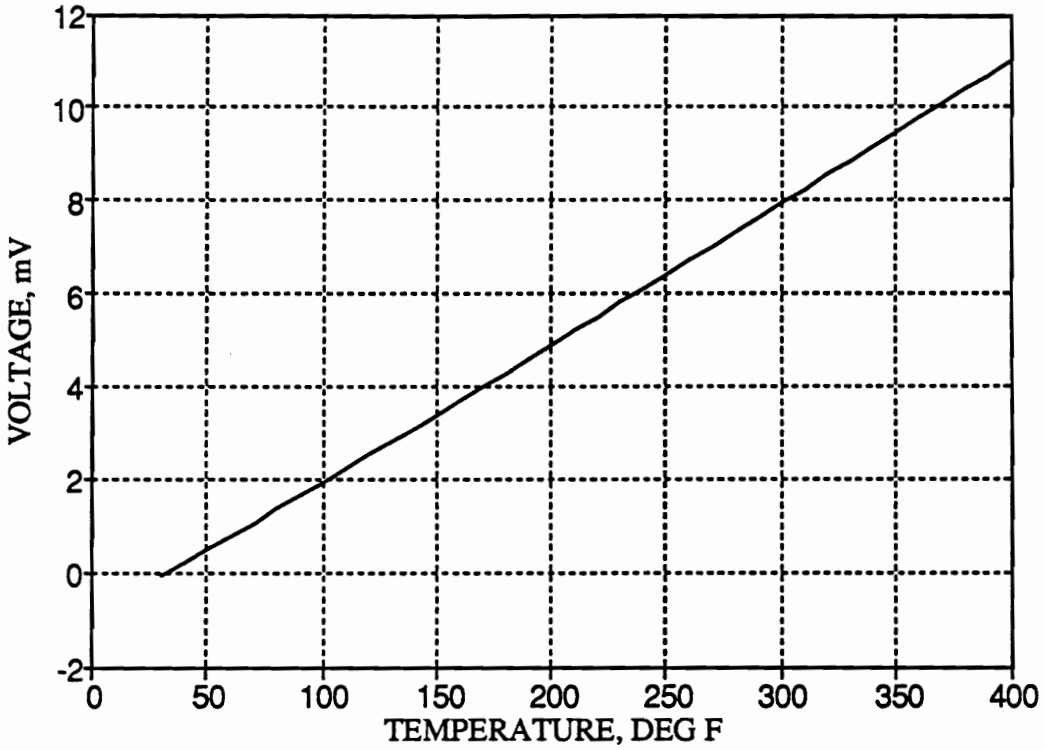

Figure A-15. Temperature-Voltage Curve of J-type Thermocouple

A.5 Flow Rates of the Air Tanks

An air tank (Speedaire, Model 4Z492) with a pressure gauge (Midwest Product, Inc.), a flow rate control valve (Speedaire, Model 1Z838C), and a rotameter (Omega Engineering, Inc., FL 73 M) is connected to the exhaust port of the air compressor to control the exhaust pressure and throughput of the air compressor. Another air tank (Speedaire, Model 4Z492) with a rotameter (Omega Engineering, Inc., FL 72 N) is connected to the cylinder chamber of the air compressor to simulate leakage of the compressor.

A.5.1 Calibration

The following calibration procedure for the rotameter FL 72N was developed to accurately reflect the flow rate of air under standard condition because the scale on the rotameter FL 72N is calibrated with fresh water[23].

A bellows gas meter (Rockwell CL-250) is used to calibrate the rotameter FL 72N; by connecting the rotameter FL 72N to the output port of the gas meter and the leakage port to the inlet of the gas meter, the calibration is performed by integrating the flow through the rotameter and comparing the integration with the readout of the gas meter. According to G.L. Tuve and L.C. Domholdt[24], errors of 1 to 2 per cent are typical for this easily set-up, easily performed calibration procedure.

Table A-3 shows the calibration data within the range of the leakage port throughput. The average factor of the reading on the rotameter FL 72N to standard air flow is 36.5.

Table A-3. Calbration Data of Rotometer FL 72N

Reading on Rotameter, *gallon/hour*	Standard Air Flow, ft^3/ sec	Fctor
3.0	0.00421	37.78
4.0	0.00520	35.03
5.0	0.00676	36.41
6.0	0.00824	36.99
7.0	0.00962	37.01
8.0	0.0106	35.78

A.6 Current and Voltage into Motor

A voltage control box is designed such that each output volt from the voltage control box represents 100 volts of input into the three phase motor. A 80i-600 ac current probe (John Fluke MFG. Co., Inc.) is used to measure the input currents to the motor.

A.7 Data Acquisition

The personal computer based data acquisition system consists an IBM-AT personal computer, a signal preprocessing card, and a Data Translation Inc. DT 2801-A system interface card.

The Data Translation DT 2801-A card is used to sample and record the input voltage, and hence, provides a measurements of instantaneous angular velocity of the shaft en-

coder, the temperature of the intake port or exhaust port or cylinder chamber of the compressor, the pressure of the cylinder chamber, the force acting on the load cell, the acceleration of the torque table, and the voltage and current input to the there-phase motor.

A.7.1 DT 2801-A Board and PCLAB

The DT 2801-A system is an analog and digital input/output interface card for an IBM personal computer. The DT 2801-A has one twelve bit analog to digital converter and two twelve bit digital to analog converter. Analog voltage can be sampled in up to sixteen single ended channels or eight differential channels. The DT 2801-A has an internal clock that can be set from 0.2 to 26.7k Hz. Data acquisition can be performed using the internal clock or user supplied external clock. Either an internal trigger or user supplied external trigger can be used to begin data acquisition. For a DT 2801-A, unipolar input ranges accept positive voltages only, ranging from 0 to +1.25V to 0 to +10V, and bipolar input ranges accept both positive and negative voltages, ranging from $\pm$ 1.25V to $\pm$ 10V[13].

The DT 2801-A system is run using the software, PCLAB[14], distributed by Data Translation Inc.. PCLAB consists of a number of callable subroutines that perform specific functions (e.g. beginning data acquisition) on the DT 2801-A board. PCLAB supports all Microsoft languages supported by MSDOS[15]. Micro-Soft Fortran 3.30[16] is used in this experiment.

A.7.2 Data Acquisition Method

The 1 PPR output signal from the flip flop of the signal preprocessing card is used as an external trigger to initiate the data acquisition. The shaft encoder is mounted in the experimental setup so that the 1 PPR output signal of the shaft encoder occurs when the piston of the compressor is at the top dead center position, using a stroboscope (General Radio, 1531-AB Strobotac) with 1 PPR signal from the encoder as input trigger to do this alignment.

In this experiment, the internal real time clock is used to start the repetitive data conversions. The time for the data acquisition is the period of one complete cycle of the crankshaft revolution such that the data sets represent the physical phenomena under consideration within one complete cycle of the crankshaft revolution. By acquiring the 1 PPR signal from the flip-flop, the period of one cycle of the crankshaft revolution can be determined. Then the data sets can be represented equally time-spaced since the internal clock ticks start the data conversation equally time-spaced.

Five channels are used to sequentially acquire the data. After the 1 PPR signal triggers the data acquisition process, 600 data points are taken; the 600 data points are equally time-spaced acquired within the period of one complete cycle of the crankshaft revolution. The $1st, 6th, 11th, \ldots, 596th$ data points represent the data set of channel 1; the $2nd, 7th, 12th, \ldots, 597th$ data points represent the data set of channel 2; the $3rd, 8th, 13th, \ldots, 598th$ data points represent the data set of channel 3; the $4th, 9th, 14th, \ldots, 599th$ data points represent the data set in channel 4; and the $5th, 10th, 15th, \ldots, 600th$ data points represent the data set in channel 5.

After the data acquisition is complete, another set of data is to be acquired using the 1 PPR external trigger to make sure the data acquisition starts at the top dead center position. As discussed by Ewins[22], averaging process is needed to eliminate the effect of random noise. Experiment shows that the average of 300 or more sets of data will insure the repeatability of the signals. Since the five channel data acquisition is sequential instead of parallel, the time references of the five data sets are different. By doing Fourier transformation and then inverse Fourier transformation, the time references can be shifted to coincidence.

The base frequency of the rotating system is below 15 Hz (synchronous speed of the motor) and 600 data points are acquired within one complete cycle of the crankshaft revolution. Therefore, the sampling rate[22] is less then 9000 Hz and for each channel, the sampling rate is approximately 1800 Hz. This insures the operation is within the capacity of DT2801-A acquisition card.

A.7.3 Low Pass Filter

The purpose of utilizing low pass filters in this experiment includes:

1. According to J. Williams[2], the first natural frequency of the load cell occurs at 360 Hz and the operating frequency range is 0-150 Hz. A low pass filter is used to cut off the high frequency contents of the load cell signal.

2. Low pass filters can be used to boost output voltages of some instruments to insure that the output signals scale to the associated physical phenomenon.

3. A low pass filter is used to sharply cut off the frequency content beyond the Nyquist frequency to avoid the distortion in the discrete Fourier transformation. The Nyquist frequency, ω_{max}, which physically defines the maximum distinguishable in frequency spectrum, is half of sampling rate, ω_s.

$$\omega_{max} = \frac{1}{2}\omega_s = 4500 \text{ Hz} \qquad (A-7)$$

According to Ewin[22], a signal which has a true frequency content shown as Figure A-16a will appear in the discrete Fourier transformation as the distorted form shown in Figure A-26b. As mentioned above, the highest frequency which can be included in the spectrum (or transform) is $\frac{\omega_s}{2}$, so the indicated spectrum should stop at that frequency. The distortion shown in Figure A-16b can be explained by the fact that the part of signal which has frequency components above Nyquist frequency will appear reflected or 'aliased' in the range from 0 to $\frac{\omega_s}{2}$.

Since this problem can be cured by using low pass filters to sharply attenuate the frequency content, filters used in this case are also called anti-aliasing filters.

In this experiment, a Frequency Devices, Model 9002 with Model LP01, 8-Pole, 6-Zero, Elliptic Low-Pass Filter was implemented to cut off the undesired high frequency components. Table A-3 shows the specifications of the low-pass filter[25].

A.7.4 Resolution and Sensitivity

According to George C. Barney[3], the resolution is defined as the ability of an instrument to respond and detect the smallest change in the input measurand. The 2801-A

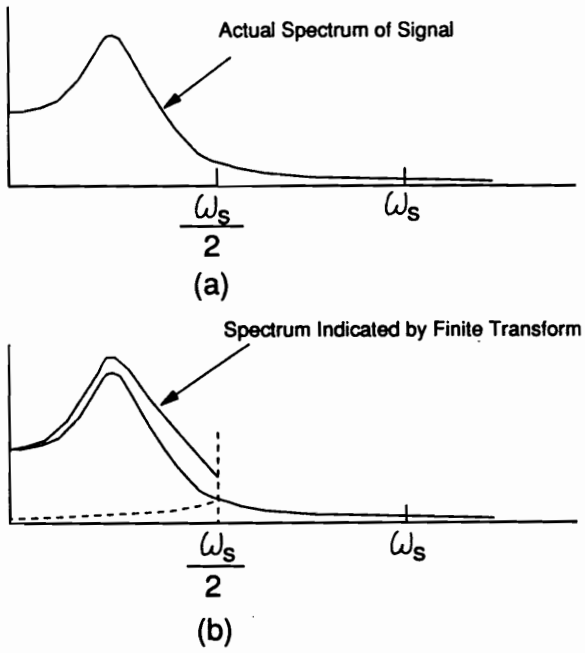

Figure A-16. Alias Distortion of Spectrum by Discrete Fourier Transform

Table A-4. Specifications of Low-Pass Filter

Manufacturer	Frequency Devices
Model	9002
Filter Model	Model LP01
Transfer Function	8-pole 6-zero
	Elliptic Low-pass
Passband Ripple	$\pm$ 0.035 dB
Stop Band Attenuation	80 dB
Cutoff Frequency,f_r	$\pm$ 2 %
Amplitude	-0.035 dB
Phase	$-323.5°$
Phase Match	
$0 - 0.8f_r$	$\pm 2°$max, $\pm 1°$typ
$0.8 - 1.0f_r$	$\pm 4°$max, $\pm 2°$typ
Filter Attenuation	
0.035 dB	$1.00f_r$
3.01 dB	$1.13f_r$
60.0 dB	$1.67f_r$
80.0 dB	$1.77f_r$
Amplitude Match	
$0 - 0.8f_r$	$\pm$ 0.2dB max, $\pm$ 0.1dB typ
$0.8 - 1.0f_r$	$\pm$ 0.4dB max, $\pm$ 0.2dB typ
Total Harmonic Distortion	-90 dB typ
Broad Band Noise	$200\mu V_{rms}$typ
Narrow Band Noise	$10nV/\sqrt{Hz}$ typ

data acquisition board has a 120-bit A/D converter[13] and the full scale range of output voltage in this experiment is selected to be $\pm$ 10V, then the resolution of the data acquisition board, ΔV, can be evaluated

$$\Delta V = \frac{20}{2^{12}} = 0.00488 \text{ V} \qquad (A-8)$$

According to James W. Dally[17], the sensitivity of a voltage recording instrument, S, is defined as the output voltage of the instrument that represents one unit of measured physical quantity. Mathematically,

$$S = \frac{E_o}{Q} \qquad (A-9)$$

where Q is the known physical quantity interested and E_o is the voltage measured.

From the definition of the resolution of the data acquisition board and the sensitivity of an instrument, the resolution of the data acquisition system, Δ, can be defined as the ability of the data acquisition system to respond and detect the smallest change in the input physical quantity. Mathematically,

$$\Delta = \frac{\Delta V}{S} \qquad (A-10)$$

This quantity, Δ, is important to describe a data acquisition system. If the resolution of a load cell data acquisition system is 0.1 lbf and the input signal is bounded within 0.2 lbf, the AC component of the output signal is meaningless since the output signal is bounded by accuracy bounds within 0.2 lbf itself.

To improve the resolution of the data acquisition system (smaller resolution), amplifiers built into the low pass filters are used to amplify the output signals from the instruments. Table A-5 shows the original sensitivities, the multiples amplified by the amplifiers, and the final resolutions of the output signals of all the instruments in this data acquisition system.

Table A-5. Sensitivity and Resolution

Instrument	Sensitivity	Mutiple	Resolution
Shaft Encoder	20.94 rad/V	2	0.0511 rad
Load Cell	52.63 lbf/V	10	0.0257 lbf
Accelerometer	20 g/V	10	0.00976 g
Pressure Transducer (1)	28.57 psia/V	2	0.06971 psia
Pressure Transducer (2)	28.57 psia/V	10	0.01394 psia
Thermocouple (3)	3328 F/V	1000	0.1624 psia
Current Probe	1 amp/V	1	0.00488 amp
Voltage Box	100 V/V	5	0.0976 amp

(1) for the inside pressure of the cylinder.

(2) for the crankcase pressure.

(3) the sensitivity is a approximation and the signal is amplified by both milivolt amplifier and filter.

A.8 Experimental Setup

The experimental setup consists of a 1/2 inch thick steel base that is attached to a wooden table via rubber mounts (Vibration Mountings and Controls Inc., Model R2[BLUE-135LB]) located at each corner, a 1/2 horsepower three phase AC induction motor, a U-joint coupling drive shaft, a single-stage, single-cylinder air compressor (Speedaire, Model 1Z943B) mounted on a table, a thermocouple system, a pressure transducer system, two air tanks with flow rate control system, an optical shaft encoder, and a personal computer data acquisition system.

The output shaft of the AC induction motor has been drilled out and replaced with a longer shaft that protrudes both ends of the motor casing. The motor is mounted by cradling both ends of the shaft in pillow block bearings.

The air compressor is mounted on a table that is attached to the base of the experimental setup with two pillow block bearings. The axis of the bearings is coincident with the axis of the air compressor. A large thrust bearing is mounted on the support shaft for the table between the table and the base of the experimental setup to reduce the support shaft deflections during operation. A compressive preload is applied to the thrust bearing by using a threaded rod that passes through the center of the support shaft[2].

A.9 References

1. Kanth, R.M., 1987, *A Personal Computer Based Instrumentation System for Determining Real-Time Dynamic Torque in Rotating Machinery* , Masters Thesis, Virginia Polytechnic Institute and State University, Blacksburg, VA.

2. Williams, J., 1989, *Parameter Identification in a Slider-Crank Mechanism Through Direct Measurement of Shaft Velocity* , Masters Thesis, Virginia Polytechnic Institute and State University, Blacksburg, VA.

3. Barney, C. George, 1988, *Intelligent Instrumentation, Microprocessor Applications in Measurement and Control*, Control System Centre, UMIST, Manchester

4. Encoder Product Company, *ACCU-CODER, Catalog*, Sandpoint, Idaho

5. Clements, Alan, 1985, *The Principle of Computer Hardware*, Oxford University Press, New York

6. Texas Instruments Incorporated, 1976, *The TTL Data Book for Design Engineers*

7. Analog Devices, 1982, *Data-Acquisition Databook, Volume I and II*

8. Gardner, M. Floyd, 1979, *Phaselock Technique*, John Willey & Sons, New York

9. National Semiconductor Corporation, 1982, *Linear Databook*

10. PCB Piezotronics, Inc., 1987, *Calibration Data, ICP Accelerometer*

11. PCB Piezotronics, Inc., 1982, *Quartz Sensors, Catalog*

12. Omega Company, *Omega Complete Temperature Measurement Handbook and Encyclopedia* , Vol. 26

13. Data Translation, Inc., 1983, *DT2801 Series, User's Manual*

14. Data Translation, Inc., 1984, *PCLAB Release Notes*, Version 2.0.

15. Microsoft Corporation, 1987, *MS DOS Disk Operation System*, Version 3.0.

16. Microsoft Corporation, 1987, *Microsoft FORTRAN Optimizing Compiler, User's Guide*, Version 3.30.

17. James W. D., William F. R., Kenneth G. M., 1984, *Instrumentation for Engineering Measurements*, John Wiley & Sons, Inc.

18. Alan S. Morris, 1988, *Principle of Measurement and Instrumentation*, Prentice Hall

19. Richard W. Miller, 1989, *Flow Measurement Engineering Handbook, Second Edition*, McGraw-Hill Publishing Company

20. John Fluke Mfg. Co., Inc., *Instruction Sheet, 80i-600 AC Current Probe*,

21. S. Borowttz, A. Beiser, 1966, *Essence of Physics*, Addison-Wesley Publishing Company, Inc.

22. Ewins, D. J., 1984, *Modal Testing; Theory and Practice*, Willey, New York

23. Omega Company, *Omega Complete Flow and Level Measurement Handbook and Encyclopedia* , Vol. 26

24. G.L. Tuve, L.C. Domholdt, 1966, *Engineering Experimentation*, McGraw-Hill Book Company, New York

25. Frequency Devices, Model 9002, *Dual-Channel Programmable Filter Instrument.*

Vita

Ming-Fa Feng, the sixth child of Mr. and Mrs. Tsun-Te Feng, was born on August 7, 1962 in Tainan, Taiwan. He was graduated from Taipei Institute of Technology in June, 1982 as a mechanical engineering major. In September, 1987, Mr. Feng earned his Master of Science degree in mechanical engineering from Virginia Polytechnic Institute and State University.

After two years of graduate study in mechanical engineering at Virginia Polytechnic Institute and State University, Mr. Feng developed his interest in academic research and decided to pursue a Doctor of Philosophy in mechanical engineering, and joined the Ph.D. program in the same department in the Fall 1987.

M. Feng.